

INFORMATION TO USERS

This manuscript has been reproduced from the microfilm master. UMI films the text directly from the original or copy submitted. Thus, some thesis and dissertation copies are in typewriter face, while others may be from any type of computer printer.

The quality of this reproduction is dependent upon the quality of the copy submitted. Broken or indistinct print, colored or poor quality illustrations and photographs, print bleedthrough, substandard margins, and improper alignment can adversely affect reproduction.

In the unlikely event that the author did not send UMI a complete manuscript and there are missing pages, these will be noted. Also, if unauthorized copyright material had to be removed, a note will indicate the deletion.

Oversize materials (e.g., maps, drawings, charts) are reproduced by sectioning the original, beginning at the upper left-hand corner and continuing from left to right in equal sections with small overlaps. Each original is also photographed in one exposure and is included in reduced form at the back of the book.

Photographs included in the original manuscript have been reproduced xerographically in this copy. Higher quality 6" x 9" black and white photographic prints are available for any photographs or illustrations appearing in this copy for an additional charge. Contact UMI directly to order.

UMI

A Bell & Howell Information Company
300 North Zeeb Road, Ann Arbor MI 48106-1346 USA
313/761-4700 800/521-0600

NOTE TO USERS

The original manuscript received by UMI contains broken or light print. All efforts were made to acquire the highest quality manuscript from the author or school. Microfilmed as received.

This reproduction is the best copy available

UMI

University of Alberta

The Efficiency of Flares in Cross-Winds

by

George A. Skinner



A thesis submitted to the Faculty of Graduate Studies and Research in partial fulfillment
of the requirements for the degree of Master of Science
Department of Mechanical Engineering

Edmonton, Alberta

Fall 1998



**National Library
of Canada**

**Acquisitions and
Bibliographic Services**

395 Wellington Street
Ottawa ON K1A 0N4
Canada

**Bibliothèque nationale
du Canada**

**Acquisitions et
services bibliographiques**

395, rue Wellington
Ottawa ON K1A 0N4
Canada

Your file Votre référence

Our file Notre référence

The author has granted a non-exclusive licence allowing the National Library of Canada to reproduce, loan, distribute or sell copies of this thesis in microform, paper or electronic formats.

The author retains ownership of the copyright in this thesis. Neither the thesis nor substantial extracts from it may be printed or otherwise reproduced without the author's permission.

L'auteur a accordé une licence non exclusive permettant à la Bibliothèque nationale du Canada de reproduire, prêter, distribuer ou vendre des copies de cette thèse sous la forme de microfiche/film, de reproduction sur papier ou sur format électronique.

L'auteur conserve la propriété du droit d'auteur qui protège cette thèse. Ni la thèse ni des extraits substantiels de celle-ci ne doivent être imprimés ou autrement reproduits sans son autorisation.

0-612-34419-3

University of Alberta

Library Release Form

Name of Author: George A. Skinner
Title of Thesis: The Efficiency of Flares in Cross-Winds
Degree: Master of Science
Year this Degree Granted: 1998

Permission is hereby granted to the University of Alberta Library to reproduce single copies of this thesis and to lend or sell such copies for private, scholarly, or scientific research purposes only.

The author reserves all other publication and other rights in association with the copyright in the thesis, and except as hereinbefore provided, neither the thesis nor any substantial portion thereof may be printed or otherwise reproduced in any material form whatever without the author's prior written permission.


15149 42 Avenue

Edmonton, Alberta

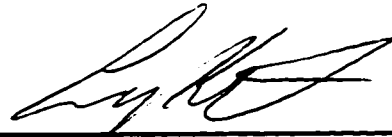
Canada T6H 5P6

August 18, 1998

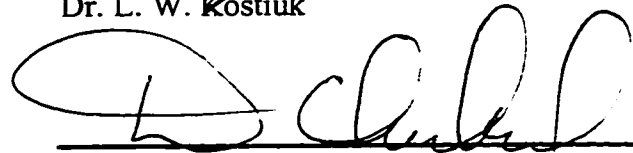
University of Alberta

Faculty of Graduate Studies and Research

The undersigned certify that they have read, and recommend to the Faculty of Graduate Studies and Research for acceptance, a thesis entitled The Efficiency of Flares in Cross-Winds submitted by George Alexander Skinner in partial fulfillment of the requirements for the degree of Master of Science.



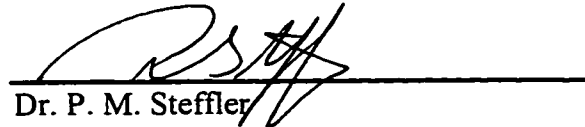
Dr. L. W. Kostiuk



Dr. M. D. Checkel



Dr. J. D. Dale



Dr. P. M. Steffler

August 17, 1998

Abstract

Flaring is a process widely used in the energy and petrochemical industries to destroy combustible waste gases. This dissertation quantifies the effects of wind on flare efficiency. A new technique has been developed to test the efficiency of scale model flares in a large closed-loop wind tunnel facility simulating various wind speeds. The technique was then used to examine the efficiency of two model flares at varying wind speeds and fuel flow rates. The tests lead to the conclusion that flare efficiency decreases with wind speed. By modeling the flare as a buoyant plume, a predictive scaling relation is derived between flare efficiency, wind speed and fuel flow rate. This model is extended to include the scale of the model that could allow the results obtained with laboratory-scale flares to be interpreted for full-sized industrial flares.

“Full speed ahead and damn the torpedoes!”

Admiral David Farragut, United States Navy

Battle of Mobile Bay

To Emma,

Acknowledgment

I would like to acknowledge the following people whose kind assistance made this dissertation possible:

Dr L.W. Kostiuk, who inspired me with the science of combustion;

Dr. M.D. Checkel, for his timely guidance;

Dr. D.J. Wilson, for showing me the beauty of “back of the envelope” calculations;

Matthew Johnson, who explained to me the mysteries of Swagelock[®] and participated in the cover-ups;

My parents, for their help and for pretending to be interested when I talked about my research;

Terry Nord and Wayne Pittman, for their valuable technical assistance;

Alan Muir, Albert Yuen, Tony van Straten, and Don, whose skilled work helped make this experiment a reality;

Dr. Eric Bourguignon, for his many contributions to the Flare Research Project;

Ric Forest, for keeping me gainfully employed throughout my graduate studies;

Chester Houg, whose guidance as my mentor assisted in my decision to pursue graduate studies;

The Department of Mechanical Engineering, for their financial support throughout my graduate studies;

and the Thursday Guys’ Night Out crew, for their continued dedication to excellence in debauchery.

Table of Contents

Chapter 1 - Introduction.....	1
Laboratory-Based Testing vs. Field Testing.....	4
Definitions of Flare Efficiencies.....	5
Local vs. Global Product Analysis.....	6
A New Technique for Measuring Flare Efficiencies in a Cross-Wind.....	8
Effects of Wind on the Efficiency of Natural Gas Flares.....	8
References.....	9
Chapter 2 - Measuring Efficiencies of Jet Diffusion Flames in a Cross-Flow.....	11
Introduction.....	11
Background.....	12
Definition of Efficiency.....	13
Global or Local Analysis.....	14
Experimental Set-Up.....	16
Experimental Methodology.....	18
Diagnostics.....	27
Discussion of Uncertainty.....	29
Preliminary Test Results.....	31
Conclusions.....	32
Notation.....	33
References.....	34

Chapter 3 - Efficiency of Natural Gas Flares In Cross-Winds.....	45
Introduction.....	45
Experimental Methodology	50
Flares Tested	51
Experimental Results	52
Interpretation of Results.....	55
Momentum-Based Correlation.....	56
Buoyancy-Based Correlation	56
Conclusions.....	60
References.....	62
Chapter 4 - Conclusions.....	76
Measuring Efficiencies of Flares in Cross-Winds	76
Efficiency of Flares in Cross-Winds.....	77
Relationship Between Efficiency, Wind Speed and Flaring Rate	77
Future Directions	78
Appendix A - Low Speed Wind Tunnel	80
Wind Tunnel Layout.....	80
Modifications for Combustion Experiments.....	81
Wind Tunnel Performance.....	83
Tunnel Leak Rate.....	83
Tracer-Decay Technique for Air Infiltration Measurements	84
Tunnel Mixing Characteristics.....	85

Tunnel Volume	86
Appendix B - Gas Analysis System.....	94
Overview.....	94
Components	94
Principles of Operation	95
Non-Dispersive Infrared (NDIR).....	95
Paramagnetic.....	96
Flame Ionization Detection (FID).....	96
Chemiluminescent.....	97
Gas Analysis System.....	97
Calibration Procedures.....	98
Analog Output Board Calibration.....	100
References.....	101
Appendix C - Experimental Diagnostics	103
Air Speed Transducers.....	103
Pressure Transducer Calibration	106
Temperature Transducer	106
Temperature Transducer Calibration	107
Mass Flow Meters & Controllers.....	108
Calibration Procedure	109
References.....	111
Appendix D - Uncertainty Analysis of Inefficiency Measurement	120

Inefficiency Equation.....	120
Expression for Uncertainty	121
Calculation of Uncertainty in $\frac{d}{dt}\left(\frac{y_{HC}}{T}\right)$	123
Sample Calculation	126
Uncertainties of Variables in Equation D.4	127
Sample Uncertainty Calculation	130
References.....	132

List of Tables

Table 3-1 - Power law exponents for plots of 25.4 mm flare inefficiency as a function of wind speed	54
Table 3-2 - Power law exponents for plots of 12.7 mm flare inefficiency as a function of wind speed	55
Table B-1 - Span Gases used for analyzer calibration	99
Table C-1 - Pitot Tube Ranges & Resolutions.....	105
Table C-2 - Mass Flow Meters used - Range, Accuracy & Resolution.....	109
Table D-1 - Uncertainties in variables used to calculate inefficiency	128

List of Figures

Figure 2.1 - Low Speed Wind Tunnel Facility used for Efficiency Measurements.	36
Figure 2.2 - Schematic of Experimental Set-Up	37
Figure 2.3 - Burner Configuration.	38
Figure 2.4 - Flow profile and turbulence intensity of 25.4 mm burner with turbulence generator	39
Figure 2.5 - Comparison of terms in wind tunnel mass balance equation.....	40
Figure 2.6 - Hydrocarbon concentration and gas flow rates for a typical test.	41
Figure 2.7 - Schematic of experimental diagnostics installation	42
Figure 2.8 - Effect of test length on measured inefficiency.....	43
Figure 2.9 - Inefficiency of flame as a function of cross-flow speed	44
Figure 3.1 - Schematic of experimental set-up used to measure flare inefficiency	65
Figure 3.2 - Hydrocarbon destruction inefficiency of 25.4 mm scale flare at varying fuel flow rates and wind speeds	66
Figure 3.3 - Power Law behavior of 25.4 mm flare destruction inefficiency for varying wind speed	67
Figure 3.4 - Hydrocarbon destruction inefficiency of 12.7 mm scale flare for varying fuel flow rate and wind speed	68
Figure 3.5 - Power law behavior of 12.7 mm flare destruction inefficiency for varying wind speed.	69
Figure 3.6 - 25.4 mm flare inefficiency plotted as a function of the ratio of air momentum to fuel momentum.	70

Figure 3.7 - Diagram illustrating plume nomenclature.....	71
Figure 3.8 - 25.4 mm flare inefficiency data plotted as a function of $\frac{U_{\infty}}{V_f^{\frac{1}{3}}d^{\frac{1}{3}}}$	72
Figure 3.9 - 12.7 mm flare inefficiency plotted as a function of $\frac{U_{\infty}}{V_f^{\frac{1}{3}}d^{\frac{1}{3}}}$	73
Figure 3.11 - Destruction inefficiencies of 12.7 mm and 25.4 mm flares plotted as a function of wind speed for varying fuel flow rates	74
Figure 3.12 - Flare inefficiency data collapses onto a single line when plotted as a function of $\frac{U_{\infty}}{V_f^{\frac{1}{3}}d^{\frac{1}{3}}}$	75
Figure A.1 - Diagram of Wind Tunnel Facility.	89
Figure A.2 - Typical decay of SF ₆ tracer gas concentration measured in the high speed test section during an air infiltration test.....	90
Figure A.3 - Wind Tunnel Leak Rate as a function of High Speed Test Section Wind Speed.....	91
Figure A.4 - Longitudinal mixing behavior of the Low Speed Wind Tunnel	92
Figure A.5 - Variation in Tracer Gas Concentration Across Low-Speed Test Section	93
Figure B.1 - Schematic of Gas Analysis System	102
Figure C.1 - Diagram of Diagnostics Installation in Wind Tunnel.....	112
Figure C.2 - Schematic of pressure transducer calibration procedure	113
Figure C.3 - Schematic of temperature transducer calibration set-up.....	114
Figure C.4 - Schematic of Mass Flow Meter Calibration Set-Up.....	115
Figure C.5 - Typical plot of output for flow meter calibration.....	116

Figure C.6 - Matheson 24.4 SLPM Flowmeter calibrated with natural gas117
Figure C.7 - Omega 100 SLPM Flow Meter/Controller calibration with natural gas118
Figure C.8 - Omega 500 SLPM Flowmeter calibrated with natural gas.....119

List of Nomenclature

AF_{st} = stoichiometric air/fuel ratio (on a mass basis)

B_1 = constant

B_2 = combined constant

$C_{p,\infty}$ = heat capacity of air (J/(kg*K))

d = flare tip flow diameter (m)

Δh_b = vertical distance between flare tip and flame centerline (m)

F_b = buoyancy flux (m^4/s^3)

g = 9.81 m/s^2

H_s = $\rho_f Q_f q_f$ = flare chemical energy release rate (W)

M = ratio of wind momentum to fuel momentum at flare tip

n_f = number of carbon atoms in a molecule of fuel

n_{ref} = number of carbon atoms in a molecule of reference gas

P_∞ = atmospheric pressure (kPa)

q_f = enthalpy of reaction of fuel & air (J/kg)

Q_f = fuel flow rate (slpm)

Q_{in} = flow rate of ambient air into wind tunnel (slpm)

Q_{out} = leakage of air from wind tunnel (slpm)

Q_{ref} = reference gas flow rate (slpm)

ρ_∞ = air density (kg/m^3)

ρ_f = density of fuel at ambient conditions (kg/m^3)

- ρ_{HC} = density of hydrocarbons in the wind tunnel (kg/m^3)
- $\rho_{\text{HC } \infty}$ = density of hydrocarbons at ambient conditions (kg/m^3)
- ρ_{ref} = density of reference gas inside wind tunnel (kg/m^3)
- R_{∞} = ideal gas constant for air (239.86 kJ/(kmol*K))
- R_{HC} = ideal gas constant for the hydrocarbon (133.38 kJ(kmol*K))
- T_{∞} = ambient temperature outside wind tunnel (K)
- T = temperature inside wind tunnel (K)
- U_{∞} = wind speed (m/s)
- V = volume of wind tunnel (m^3)
- V_f = average fuel velocity at flare tip (m/s)
- x_b = distance downstream of flare stack (m)
- y_{HC} = concentration of hydrocarbons (ppm)
- $y_{\text{HC } \infty}$ = background concentration of hydrocarbons (ppm)

Chapter 1 - Introduction

Flaring is widely used in the energy and petrochemical industries to destroy combustible waste gases. As many of these waste gases pose environmental or explosion hazards, they must be destroyed reliably. Research conducted prior to 1996 had concluded that flares burn fuel at efficiencies greater than 98% except near blow-off [Pohl et. al., 1986].

However, these tests were conducted in quiescent environments and considered only gaseous fuels. More recent research has suggested that a cross-wind can reduce flaring efficiency [Strosher, 1996]. Unfortunately, these conclusions were based on field studies where test parameters like wind speed, gas composition, gas flow rate and inclusion of liquid hydrocarbons were poorly controlled or unknown. As a result the quantitative question of the effects of wind on flare efficiency were left unanswered.

The behavior of flares has been studied for more than a half century and has its origins in studying jet diffusion flames. Initial research specific to flaring focused on characterizing the shape, flame modes, radiation field and stability limits of the flames in order to develop procedures for the design of industrial flares [c.f., Gollahalli et. al., 1975; Brzustowski, 1975; Brzustowski, 1976; Kalghati, 1983]. With the advent of stricter environmental regulations in the 1970s' and 1980s', studies shifted to the effectiveness of a flare at destroying waste gases from industrial and petrochemical operations. Major studies of flare efficiencies have been conducted in the United States of America by the Chemical Manufacturers' Association (CMA) and the Environmental Protection Agency

(EPA); in Europe by Shell Research and British Gas, and in Canada by the Alberta Research Council (ARC).

Previous studies into flare efficiency have not focused on wind effects. In fact, several of the studies purposely avoided wind effects [Pohl, 1986]. Studies conducted on flare geometry recognized that a cross-flow altered flame shape, but no reference was made to how the change in flame shape affected efficiency. Some field studies have been conducted with mild winds, but no study has performed a systematic investigation into wind effects [Stroscher, 1996; Kuipers et. al., 1996].

Laboratory tests are well-suited to parametric studies of flare behavior, but are of little use if they cannot be correlated to the large flares used by the energy and petrochemical industries. An important question is how results obtained from small laboratory scale tests scale up to larger industrial flares. With the exception of the EPA studies, laboratory-based flare experimentation has been limited to flares less than 25.4 mm in diameter. For example, Kalghati's scale flares ranged from 6 mm to 14 mm in diameter [Kalghati, 1983]. In contrast, industrial flares range in size from 100 mm to 3 m in diameter.

As mentioned, the objective of this dissertation is to quantify the effects of wind on flare efficiency. To do this a new technique has been developed to test the efficiency of scale model flares in a large closed-loop wind tunnel facility simulating various wind speeds. The technique was then used to examine the efficiency of two model flares at varying wind speeds and fuel flow rates. The tests lead to the conclusion that flare efficiency

decreases with wind speed. By modeling the flare as a buoyant plume, it was possible to derive a predictive scaling relation between flare efficiency, wind speed and fuel flow rate. This model has also been extended to include the scale of the model that could allow the results obtained with laboratory-scale flares to be interpreted for full-sized industrial flares.

This dissertation consists of two papers written for submission to a refereed journal dealing with combustion sciences. The first paper is titled “Measuring Efficiencies of Jet Diffusion Flames in a Cross-Flow”, and describes the wind tunnel technique developed to measure flare efficiencies. The second paper is titled “Efficiency of Natural Gas Flares in Cross-Winds” and contains the results of testing two different scale model flares and the derivation of a predictive scaling rule for flares based on buoyant reacting plumes. A concluding chapter follows the two papers, summarizing the conclusion and results of this dissertation. Four appendices are included in this dissertation, detailing an uncertainty analysis of the technique used to measure flare efficiency and the diagnostics and experimental facility used in the flare tests.

The remainder of this chapter provides an introduction to the concepts of laboratory-based testing versus field testing, different definitions of flare efficiency, local versus global product analysis, and introductions to the two papers that comprise the body of this dissertation.

Laboratory-Based Testing vs. Field Testing

Research into the efficiency of flares has been conducted under both laboratory and field conditions. The laboratory conditions typically allow for good control of fuel flow rate and ambient conditions, but result in lack of wind effects and limit the size of flare that can be investigated. Field conditions permits testing of large flares under operational conditions, but typically suffer from poor control of test conditions such as wind speed and from the difficulty of instrumenting a large flame 10-30 meters above ground level.

The size of the large flares encountered in field tests means that flare efficiency measurements are typically based on sampling of flare products at a single point from the flare plume. The smaller flares employed in laboratory tests permit more sophisticated methods of sampling such as hood sampling that provide a more homogeneous sample from the flare plume.

Most flare efficiency tests have been conducted under field conditions both because the size of industrial flares complicates laboratory tests and because the use of an existing flare eliminates the expense of constructing a test apparatus. A major study was conducted by the CMA in 1983 at a large industrial flare located at a refinery [Romano, 1983; Keller, 1983]. Other field studies have been conducted since in Nigeria [Obioh et. al., 1993], by the ARC [Strosher, 1996], and by Shell Research and British Gas [Kuipers et. al., 1996]. Field conditions suffer from poor control of test parameters such as wind speed, gas composition, gas flow rate and inclusion of liquid hydrocarbons. In all studies

except the ARC the efficiency was reported to be >95%. The ARC study found efficiencies as low as 64%.

Laboratory conditions allow good control of test parameters, however only a limited number of tests have been performed under laboratory conditions.. The ARC conducted some small-scale laboratory tests whose primary purpose was to develop an experimental technique that could be used in pilot scale and field parts of their study. These laboratory tests were restricted in the size of flames which could be tested and lacked a suitable method for creating a cross-flow [Stroscher, 1996]. The EPA studied full-sized flares (37-300 mm diameter) outdoors but under what were essentially laboratory conditions in the early 1980s' at its large scale test facility, but did not investigate wind effects [Pohl, 1986]. Both of these studies resulted in efficiencies >95% as long as they were conducted in quiescent conditions.

Definitions of Flare Efficiencies

Flare efficiency is commonly defined either as a destruction efficiency or a combustion efficiency. Destruction efficiency focuses on a single or group of chemical species that can react (*i*) and accounts for the fraction of those species in the reactant stream that are destroyed by the flare.

$$\eta_d = \frac{\text{mass flow rate of species } i \text{ in products}}{\text{mass flow rate of species } i \text{ in reactants}} \quad 1.1$$

Combustion efficiency focuses on the conversion of an element that exists in the fuel to its fully oxidized state. Combustion efficiency based on carbon measures the fraction of

carbon atoms that are not fully oxidized in the reactant stream (e.g. hydrocarbons and CO) that become fully oxidized by the flame (CO₂).

$$\eta_c = \frac{\text{Mass flow rate of fully oxidized carbon produced by the flame}}{\text{Total mass flow rate of carbon in reactants not as CO}_2} \quad 1.2$$

Combustion efficiencies based on other elements (e.g. sulphur) can be written in a similar manner. Combustion efficiency is a more conservative assessment of flare efficiency. Species considered destroyed under the definition of destruction efficiency have been converted to toxic products such as carbon monoxide or polynuclear aromatic hydrocarbons (e.g. benzial pyrene, ethynyl benzene or cyclohexane). The definition of combustion efficiency does not consider the flare to be efficient unless these partially oxidized products have also been completely oxidized to carbon dioxide. However, destruction efficiency and combustion efficiency have been found to be closely related; a high destruction efficiency generally implies a high combustion efficiency [Pohl, 1986].

Local vs. Global Product Analysis

Efficiency measurements can be conducted on a local or global basis. A global analysis bases efficiency on the overall composition of all of the combustion products, and a local analysis is based on the composition of the products collected at a single point in the flow where the plume of the diffusion flame is likely to be located. In local analysis, only a small fraction of the combustion products are analyzed and cannot be directly related to the amounts of species fed to the flame as fuel. Consequently, a local analysis can only measure combustion efficiency for the gases sampled and may or may not be representative of the global combustion efficiency. Local measurements cannot be used

to measure the actual mass of any species emitted from a flare, only their relative proportions at the point of measurement. Global analysis determines the absolute masses of species in the products which can be equated to the masses of species present in the fuel, permitting the determination of both destruction and combustion efficiencies.

The majority of research has relied upon local analysis of combustion products. A popular method for determining the product composition is to use an aspirating probe to sample from the plume. The probe samples from a point within the presumed location of the plume downstream of the flare. This method was used by the CMA [Keller & Noble, 1983; Romano, 1983], the ARC [Stroscher, 1996], and in Nigeria [Obioh et. Al., 1994]. Plume sampling is an easily-implemented method for measuring the efficiencies of large flames such as the industrial flares tested in the studies mentioned above. However, plume sampling cannot determine absolute masses of products from the flame, and relies on the assumption that samples taken at a single point in space are representative of the overall plume composition. This assumption suffers from plume inhomogeneity and intermittency.

A global product analysis has the advantage of analyzing all of the flame products and eliminating the need to interpret local plume composition to the entire flame. A global balance is more difficult to perform than a local balance because of the need to collect all of the combustion products, which can be extremely difficult for large flames. The EPA used a global product balance at its large-scale test facility in the early 1980s' [Pohl et. al., 1986].

A New Technique for Measuring Flare Efficiencies in a Cross-Wind

Chapter 2 describes the technique developed to measure the hydrocarbon destruction efficiency of a well-controlled jet diffusion flame in a cross-flow using a laboratory-based global product analysis. The method had the combustion occur in a large closed-circuit wind tunnel and measured the build-up of combustion products in the wind tunnel. The rate of accumulation of unburned fuel in the wind tunnel was used to determine the efficiency of the flame at a given cross-flow.

Effects of Wind on the Efficiency of Natural Gas Flares

In Chapter 3, the laboratory-based method for measuring flare destruction efficiency described in Chapter 2 is used to measure the efficiencies of two different scale pipe flares at varying fuel flows and wind speeds. Modeling a flare as a buoyant plume allows efficiency to be correlated with a power law that relates the flare exit velocity and the wind speed. The same model provides some insight into the scaling of results obtained with small laboratory-scale flares to large industrial flares.

References

Bahadori, M.Y.; Stocker, D.P.; Vaughan, D.F.; Zhou, L.; Edelman, R.B.; "Effects of Buoyancy on Laminar, Transitional, and Turbulent Gas Jet Diffusion Flames", Second International Microgravity Combustion Workshop, NASA, 1993.

Briggs, G.A.; Plume Rise Predictions, in *Lectures on Air Pollution and Environmental Impact Analyses*, Workshop Proceedings, American Meteorological Society, pp. 59-111, . Sept. 29 - Oct. 3 1975.

Brzustowski, T.A., "Flaring in the Energy Industry", *Prog. Energy Combust. Sci.*, 2, pp.129-141, 1976.

Brzustowski, T.A., "The Turbulent Diffusion Flame in a Cross-Wind", *Proceedings of the Fifth Canadian Congress of Applied Mechanics*, University of New Brunswick, Fredericton, 1975.

Gollahalli, S.R.; Brzustowski, T.A.; Sullivan, H.F.; "Characteristics of a Turbulent Propane Diffusion Flame in a Cross-Wind", *Transactions of the CSME*, 3, No. 4, pp.205-214, 1975.

Kalghati, G.T.; "The Visible Shape and Size of a Turbulent Hydrocarbon Jet Diffusion Flame in a Cross-Wind", *Combustion and Flame*, 52, pp.91-106, 1983.

Keller, Mike; Noble, Roger; "RACT for VOC - A Burning Issue", *Pollution Engineering*, July 1983, pp.20-23.

Kuipers, E.W.; Jarvis, B.; Bullman, S.J.; Cook, D.K.; McHugh, D.R.; Combustion Efficiency of Natural Gas Flares; Effects of Wind Speed, Flow Rate and Pilots, Shell Research and Technology Center Thornton & British Gas Research Center, 1996.

Obioh, I.B.; Oluwole, A.F.; Akeredolu, F.A.; "Non-CO₂ Gaseous Emissions From Upstream Oil and Gas Operations in Nigeria", *Environmental Monitoring and Assessment*, 31, pp. 67-72, 1994.

Pohl, J.H.; Lee, J.; Payne, R.; Tichenor, B.A.; "Combustion Efficiency of Flares", *Combustion Science and Technology*, 50, pp.217-231, 1986.

Romano, R.R.; "Control Emissions with Flare Efficiency", *Hydrocarbon Processing*, October 1983, pp.78-80.

Stroscher, M.; Investigations of Flare Gas Emissions in Alberta, Environmental Technologies, Alberta Research Council, 1996.

Chapter 2 - Measuring Efficiencies of Jet Diffusion

Flames in a Cross-Flow

Introduction

Jet diffusion flames are widely used in the energy and petrochemical industries to destroy combustible waste gases. When used in this application these diffusion flames are known as flares. As many of these waste gases pose environmental or explosion hazards, they must be destroyed reliably. Atmospheric wind is one of the influences believed to reduce the combustion efficiency of a jet diffusion flame, but the effect of such cross-flows has not been explicitly examined. Research conducted to date has concluded that flares burn fuels at efficiencies greater than 98% except near blow-off [c.f. Pohl et. al., 1986].

However, these tests have been conducted in quiescent environments. More recent research has identified some limitations of these previous measurements [Stroscher, 1996].

However, these recent investigations were conducted under field conditions, and test parameters like wind speed, gas composition, gas flow rate and potential inclusion of liquid hydrocarbons were poorly controlled. As a result the quantitative question of the effects of wind on combustion efficiency is left unanswered.

In the current study a laboratory-based method has been developed for measuring the efficiency of a systematically varied jet diffusion flame in a cross-flow under well-controlled conditions. Combustion occurred in a large closed-circuit wind tunnel and the

build-up of combustion products in the wind tunnel was measured. The rate of accumulation of unburned fuel in the wind tunnel was used to determine the efficiency of the flame. This paper describes the measurement technique and presents the results for a 25 mm diameter pipe flare burning natural gas at a range of cross-flow speeds.

Background

The behavior of jet diffusion flames in a cross-flow has been studied since the early 1960s'. Initial research focused on characterizing the shape, flame modes, radiation field and stability limits of the flames in order to develop procedures for the design of industrial flares [Gollahalli et. Al., 1975; Brzustowski, 1975; Brzustowski, 1976]. With the advent of stricter environmental regulations in the 1970s' and 1980s', studies shifted to the effectiveness of a jet diffusion flame at destroying waste gases from industrial and petrochemical operations.

Research into the efficiency of jet diffusion flames has been conducted under both laboratory and field conditions. The laboratory conditions typically allow for good control of fuel flow rate and ambient conditions, but have no cross-flow effects and limit the size of flame that can be investigated. Few efficiency tests have been performed under laboratory conditions. The Alberta Research Council (ARC) conducted some small-scale laboratory and pilot scale tests as part of its study of the performance of industrial flares. The pipe diameter of these flares were ≤ 6 mm and the study did not include extensive testing in a cross-flow [Stroscher, 1996]. Studies conducted for the U.S. Environmental Protection Agency (EPA) in the early 1980s' employed larger flames (32-

300 mm pipe diameter), but despite their scale, were like laboratory experiments because of the well controlled fuel composition and flow rate. The EPA study, through the use of wind screens, did not investigate cross-flow effects [Pohl, 1986].

Field studies normally involve testing of large flares used by the petroleum industry.

Field tests inherently suffer from poor control of test conditions such as cross-flow speed and from the difficulty of instrumenting a large flame 10-30 meters above ground level.

The quality of field test data ranges from limited knowledge of fuel composition and flow rate [Stroscher, 1996] to the well-determined fuel composition and flow rates of the Shell/British Gas study [Kuipers et. al., 1996].

Definition of Efficiency

Several definitions of flame efficiency have been used, including destruction efficiency or combustion efficiency. Destruction efficiency (η_d) accounts for the fraction of a species or group of species that exists in the reactant stream that are destroyed by the flare.

$$\eta_d = \frac{\text{mass flow rate of species } i \text{ in products}}{\text{mass flow rate of species } i \text{ in reactants}} \quad 2.1$$

For example, the destruction efficiency for methane would be defined as the amount of methane contained in the flame products divided by the amount of methane delivered to the flame as fuel. Combustion efficiency (η_c), based on carbon, measures the fraction of carbon atoms that are not fully oxidized in the reactant stream (e.g. hydrocarbons and CO) that become fully oxidized (CO₂) by the flame.

$$\eta_c = \frac{\text{Mass flow rate of fully oxidized carbon produced by the flame in products}}{\text{Total mass flow rate of carbon in reactants not as CO}_2} \quad 2.2$$

The destruction efficiency is often an adequate measure of flame performance if the flame is being used to destroy a hazardous substance [Pohl, 1986]. This work will measure the destruction efficiency of hydrocarbons in the flame.

Global or Local Analysis

Efficiency measurements can be conducted on a local or global basis. A global analysis bases efficiency on the overall composition of all of the combustion products, and a local analysis is based on the composition of the products collected at a single point in the flow where the plume of the diffusion flame is likely to be located. In local analysis, only a fraction of the combustion products are analyzed and cannot be correlated with the amounts of species fed to the flame as fuel. Consequently, a local analysis can only measure combustion efficiency. Global analysis determines the absolute masses of species in the products which can be equated to the masses of species present in the fuel, permitting the determination of both destruction and combustion efficiencies.

The majority of research has relied upon local analysis of combustion products. A popular method for determining the product composition is to use an aspirating probe to sample from the plume. This method was used by the Chemical Manufacturer's Association [Keller & Noble, 1983; Romano, 1983], the Alberta Research Council [Stroscher, 1996], and in Nigeria [Obioh et. Al., 1994]. Plume sampling is an easily-implemented method for measuring the efficiencies of large flames such as the industrial

flares tested in the studies mentioned above. However, plume sampling cannot determine absolute masses of products from the flame, and relies on the assumption that samples taken at a single point in space are representative of the overall plume composition. This assumption suffers from plume inhomogeneity and intermittency, requiring proper accounting for ambient material drawn into the sample.

A global product analysis has the advantage of analyzing all of the flame products and eliminating the need to interpret local plume composition to the entire flame. A global balance is more difficult to perform than a local balance because of the need to collect all of the combustion products, which can be extremely difficult for large flames. The EPA used a global product balance of major chemical species at its large-scale test facility [Pohl et. al., 1986].

A third method of measuring flame efficiency has been developed recently by Shell Research and Technology Center Thornton and the British Gas Research Center. This method makes use of two non-intrusive techniques called DIAL (Differential Infra-red Absorption Laser) and FTIR (Fourier Transform Infra-Red), which use the radiation signature of a product plume to determine plume composition [Kuipers et. Al., 1996]. The difficulty in measuring the radiation emitted by a product plume is that portions of the spectrum will be absorbed or masked by background species such as water vapor in the space between the plume and the detector. The DIAL and FTIR techniques are not

local measurements as they examine large portions of the plume, but are also not a global measurement because they are limited to collecting data along a “line-of-sight”.

Experimental Set-Up

The goal of this research project was to accurately measure the global destruction efficiency of a jet diffusion flame in a cross-flow to determine if an effect exists. This required collection of all of the products of what is essentially an open flame placed in a cross-stream. To achieve this, a jet diffusion flame was burned in a closed-loop wind tunnel where the cross-flow speed could be well controlled. A schematic of the wind tunnel and the experimental set-up are depicted in Figures 2.1 and 2.2.

The wind tunnel shown in Figure 2.1 is a closed-loop design with 2 test sections: a large low speed test section with a 2.5x2.5 m cross-section and a smaller high speed section with a 1.44x2.44 m cross-section. All the tests reported here were conducted in the high speed test section. The flow is driven by a 200 HP DC electric motor that can produce steady wind speeds from 0.20 to 25 m/s in the high speed test section. The high speed test section has extremely low turbulence levels and a flat plug velocity profile [Wilson, 1979]. The gases circulating in the tunnel are well mixed by a combination of turbulence produced by the tunnel fan and the addition of 4 small fans in the upper test section [Mixing performance is described in Appendix A]. The wind tunnel volume is approximately 350 m³, permitting long burning times before significant oxygen depletion

or emission build-up. The exact volume is not well-defined due to the size and complex geometry of the tunnel.

The burner for the jet diffusion flame was a steel pipe located in the high speed test section as shown in Figure 2.2. The length of the test section is 12 m with the burner located 9.5 m from the leading edge of the test section. The pipe used in these tests had an outer diameter (O.D.) of 25.4 mm and an inner diameter (I.D.) of 22.1 mm, but burners ranging from 6 mm O.D. to 51 mm O.D. could be installed. The burner penetrates the floor of the wind tunnel and extends 300 mm into the test section. A turbulence generator with 3 mm diameter holes and 50% blockage was placed inside the pipe to produce a turbulent flow profile with 10% turbulence intensity [Bourguignon, 1997]. Figure 2.3 illustrates the design of the burner with turbulence generator. The turbulence generator is used to ensure that the flow remains turbulent even at lower flow rates where pipe flow would normally be laminar. Figure 2.4 illustrates the flow and turbulence profiles produced by the addition of the turbulence generator.

The burner was ignited with a retractable hydrogen flame burner positioned directly in front of the burner. A “reference” gas injection port was located 1 m behind the burner in the lower test section. The purpose of this reference gas injection is discussed in the next section.

Experimental Methodology

The use of a closed-loop wind tunnel is well-suited for the measurement of the efficiencies of jet diffusion flames. The products of the combustion are trapped within the wind tunnel, providing a control volume for analysis of the efficiency based on the entire emissions of the flame.

For any experiment the cross-flow is set to a chosen speed and the fuel flow to the flame is set at a fixed rate. As the flame burns, its combustion products are captured in the closed-loop wind tunnel and mix with the air in the tunnel. The gas sampling port is placed upstream of the flame in the test section to allow for maximum mixing before sampling. By measuring the rate of accumulation of combustion products, the efficiency (or inefficiency) of the flame can be determined.

For the purposes of these experiments the destruction inefficiency (I_d) of hydrocarbons is defined as

$$I_d = 1 - \eta_d = \frac{\text{mass flow rate of unburnt hydrocarbons in combustion products}}{\text{mass flow rate of hydrocarbons delivered to flame}} \quad 2.3$$

where η_d is the hydrocarbon destruction efficiency.

A mass balance of the hydrocarbons in the wind tunnel is given by

$$\begin{aligned}
 \text{Rate Hydrocarbons Accumulate} &= \text{Rate In} - \text{Rate Out} & 2.4 \\
 &= \text{Rate In Due to Infiltration} + \text{Rate In Due to Inefficient Combustion} \\
 &\quad - \text{Rate Out Due to Leakage} \\
 &\quad - \text{Rate Out Due to Destruction of Accumulated Hydrocarbons by Flame}
 \end{aligned}$$

Writing this equation in terms of mass flow rates,

$$\dot{m}_{\text{acc}} = \dot{m}_{\text{infiltration}} + \dot{m}_{\text{flame}} - \dot{m}_{\text{leakage}} - \dot{m}_{\text{destruction}} \quad 2.5$$

Expressing the hydrocarbon mass flow rates as the product of density and volume flow rate,

$$\rho_{\text{HC}} Q_{\text{acc}} = \rho_{\text{HC}} Q_{\text{infiltration}} + \rho_{\text{HC}} Q_{\text{flame}} - \rho_{\text{HC}} Q_{\text{leakage}} - \rho_{\text{HC}} Q_{\text{destruction}} \quad 2.6$$

The infiltration and leakage terms account for the exchange of hydrocarbons in the air in the tunnel with the surrounding air since the tunnel is not perfectly sealed. Leak tests showed a typical exchange rate of 0.7 air changes per hour ($\sim 4 \text{ m}^3/\text{min}$). The flame is treated as a source of hydrocarbons as the result of inefficient combustion, and the destruction term comes from accumulated hydrocarbons being re-burned as the tunnel air is recirculated past the flame.

Modeling the tunnel as a vessel whose time rate of change in mean concentration of hydrocarbons can be characterized by the rate of change of concentration at the sampling point (i.e., after it is well-mixed) allows Equation 2.6 to be rewritten as

$$\frac{d}{dt}(\rho_{\text{HC}} y_{\text{HC}} V) = \rho_{\text{HC},\infty} y_{\text{HC},\infty} Q_{\text{in}} - \rho_{\text{HC}} y_{\text{HC}} Q_{\text{out}} + I_d n_f \rho_f Q_f - \rho_f Q_f A F_{\text{st}} \frac{\rho_{\text{HC}}}{\rho} y_{\text{HC}} (1 - I_d)^2 \quad 2.7$$

where

- ρ_{HC} = density of hydrocarbons in the wind tunnel (kg/m³)
- $\rho_{\text{HC},\infty}$ = density of hydrocarbons at ambient conditions (kg/m³)
- y_{HC} = volume fraction of hydrocarbons
- $y_{\text{HC},\infty}$ = background volume fraction of hydrocarbons
- V = volume of wind tunnel (m³)
- Q_{in} = flow rate of ambient air into wind tunnel (m³/s)
- Q_{out} = leakage of air from wind tunnel (m³/s)
- n_f = number of carbon atoms in a molecule of fuel
- ρ_f = density of fuel at conditions inside wind tunnel (kg HC/ m³ HC)
- Q_f = fuel flow rate (m³/s)
- $A F_{\text{st}}$ = stoichiometric air/fuel ratio
- ρ = density of air inside wind tunnel (kg/m³)

The inclusion of n_f in the generation term reflects the fact that the volume fraction of hydrocarbons in the wind tunnel is measured by a flame ionization detector (FID). The FID reports hydrocarbon concentration as methane-equivalent. Since the fuels being burned are alkanes their FID response is proportional to the number of carbon atoms in

the fuel molecule. [See Appendix B for details on the theory of flame ionization detector operation.]

The last term on the right hand side is based on the assumption that the hydrocarbons entering on the air side are burned with the same efficiency as those coming from the fuel side. The importance of this assumption is negligible since this term will be shown to be small compared to other terms.

Since the wind tunnel remains at a constant mean pressure, the rate of leakage out of the tunnel is equal to the rate of infiltration plus the added volume created by combustion of the fuel inside the wind tunnel. Since the fuels used in this study are a mixture of alkanes, which have the general chemical form $C_{n_f}H_{2n_f+2}$, then

$$Q_{out} = \left(Q_{in} + \frac{2n_f + 1}{1.5(n_f + 1)} Q_{fuel} \right) \left(\frac{T}{T_{\infty}} \right) \quad 2.8$$

where

T = temperature inside wind tunnel (K)

T_{∞} = ambient temperature outside wind tunnel (K)

Substituting Equation 2.8 into 2.7 gives

$$\begin{aligned}
 \underbrace{\frac{d}{dt}(\rho_{\text{HC}} y_{\text{HC}} V)}_I &= \underbrace{\rho_{\text{HC},\infty} y_{\text{HC},\infty} Q_{\text{in}}}_{II} - \underbrace{\rho_{\text{HC}} y_{\text{HC}} \left(Q_{\text{in}} + \frac{2n_f + 1}{1.5(n_f + 1)} Q_{\text{fuel}} \right)}_{III} \left(\frac{T}{T_\infty} \right) \\
 &+ \underbrace{I_d n_f \rho_f Q_f}_{IV} - \underbrace{\rho_f Q_f \text{AF}|_{\text{st}} \frac{\rho_{\text{HC}}}{\rho} y_{\text{HC}} (1 - I_d)^2}_{V}
 \end{aligned} \tag{2.9}$$

where the terms represent

- I - Rate of hydrocarbon accumulation in the wind tunnel
- II - Infiltration of hydrocarbons to the wind tunnel
- III - Leak of hydrocarbons from the wind tunnel
- IV - Generation of hydrocarbons by incomplete combustion
- V - Destruction of accumulated hydrocarbons by flame

At large times when hydrocarbon accumulation has resulted in a significant value of y_{HC} , all of the terms on the right-hand side of Equation 2.9 are important in determining the rate of hydrocarbon accumulation. However, at small times y_{HC} will be small and so will terms III and V, which depend on the instantaneous hydrocarbon concentration in the tunnel. The variation of the terms in Equation 2.9 with time is shown in Figure 2.5 for a modeled case with $\eta_d=0.025$, fuel supply rate $Q_f=20$ slpm and air infiltration of 0.65 air changes per hour with hydrocarbon background volume fraction $y_{\text{HC},\infty}=2.5$ ppm. It can be seen that the effects of the infiltration and destruction terms are negligible compared to the other terms. Similarly, for small elapsed times, the leakage term is small because it

includes the volume fraction of hydrocarbons in the tunnel and can be neglected. Taking the limit of Equation 2.9 as $t \rightarrow 0$,

$$\frac{d}{dt} \rho_{\text{HC}} y_{\text{HC}} V \Big|_{t \rightarrow 0} = I_d \rho_f Q_f n_f \quad 2.10$$

Treating the wind tunnel as constant volume and constant mean pressure and introducing the ideal gas equation for ρ_{HC} , Equation 2.10 can be rearranged to give the destruction inefficiency as

$$I_d = \frac{V}{\rho_f Q_f n_f} \frac{d}{dt} \left(\frac{P}{R_{\text{HC}} T(t)} y_{\text{HC}} \right) \Big|_{t \rightarrow 0} \quad 2.11$$

where

P = pressure inside wind tunnel (Pa)

R_{HC} = specific gas constant for the hydrocarbon (J/kg K)

This gives a simple expression with 2 unknown terms: wind tunnel volume (V) and the hydrocarbon destruction inefficiency of the jet diffusion flame (I_d). The large size and irregular shape of the wind tunnel makes precise measurement of its volume difficult if not impossible. Further, the wind tunnel geometry may result in flow separation and recirculating regions, causing the participating volume of the wind tunnel to vary with operating speed.

To eliminate tunnel volume, a second equation is introduced based on conducting a second test at the same conditions as the first, with the addition of a known reference flow of unburned fuel into the wind tunnel. This additional fuel modifies Equation 2.11 to give a second, independent equation:

$$I_d = \frac{V}{\rho_f Q_f n_f + \rho_{ref} Q_{ref} n_{ref}} \frac{d}{dt} \left(\frac{P}{R_{HC} T(t)} y_{HC} \right) \Big|_{t \rightarrow 0} \quad 2.12$$

where

ρ_{ref} = density of reference gas inside wind tunnel (kg/m³)

Q_{ref} = reference gas flow rate (m³/s)

n_{ref} = number of carbon atoms in a molecule of reference gas

Combining Equations 2.11 and 2.12 to eliminate V, an expression is obtained for the inefficiency of the jet diffusion flame.

$$I_d = \frac{\rho_{ref} Q_{ref} n_{ref}}{\rho_f Q_f n_f} \left(\frac{\frac{d}{dt} \left(\frac{y_{HC}}{T(t)} \right) \Big|_{t \rightarrow 0}}{\frac{d}{dt} \left(\frac{y_{HC}}{T(t)} \right) \Big|_{t \rightarrow 0}} - 1 \right)^{-1} \quad 2.13$$

The compositions for the fuel and reference hydrocarbon are known. The temperature and concentration of unburned hydrocarbons inside the wind tunnel are measured throughout the test. If the reference gas is the same as the fuel gas the leading coefficient on the right-hand side can be simplified by eliminating the ρ 's and n 's.

Hence to calculate inefficiency, the test was performed in 3 parts: first, the flame was burned at the desired cross-flow velocity while the concentration of hydrocarbons in the wind tunnel was measured. The second part of the test purged the wind tunnel to lower the volume fraction of hydrocarbons back to ambient conditions. In the third part of the test, the flame was burned at the same conditions, but a reference stream of unburned gas was introduced downstream of the burner. This generated the information required to determine flame inefficiency. Figure 2.6 is a plot of hydrocarbon concentration and fuel flow during a typical test.

The actual experiments are complicated by the ignition and establishment of steady flow conditions. It is because of these start-up transients that it is more sound to track the rates of accumulation of masses in the tunnel rather than total collected mass.

Initially, the flame was lit with no cross-flow, and then the wind tunnel flow velocity was brought up to the desired test speed. During the first 2-3 minutes of burning, several transient signals appeared in the hydrocarbon concentration data. Some hydrocarbons escaped combustion while the burner was lit, causing a brief spike in hydrocarbon

concentration. The inefficiency of the flame also varied as the wind tunnel flow speed increases, creating a non-uniform rate of hydrocarbon generation. Finally, a mixing transient appeared in the data because of the 2-3 passes (taking ~20-90 seconds) the plume must make through the wind tunnel to create a stationary longitudinal distribution of hydrocarbons relative to the mean concentrations. After the transients disappeared, data acquisition began for calculating I_q . The flame was typically burned for 15 minutes while the concentration of hydrocarbons in the wind tunnel was measured. Between the two test segments the flame was extinguished and the wind tunnel is purged of combustion products using a combination of large vents and ventilation fans [See Appendix A for details of the tunnel purge system].

The initial transient behavior of the experiment prevents the condition of $t \rightarrow 0$ in the expressions for inefficiency from being taken literally and actually means time prior to when the volume fraction of hydrocarbons in the wind tunnel makes the effect of tunnel leakage important. For the purposes of the tests, $t=0$ was taken as the point when steady accumulation of hydrocarbons begins. From Figure 2.6 it can be seen that when the initial transients settled out, the slope of the hydrocarbon accumulation plot became constant so the exact choice of $t=0$ is not important.

After purging, the flare was re-lit and reference gas turned on for the second part of the test. The reference gas flow rate was set so that it would roughly double the rate of hydrocarbon accumulation in the wind tunnel. This was intended to produce a well-

conditioned set of equations for calculating combustion efficiency. If the reference flow was too small, the change in rates of accumulation between the two tests would be small and difficult to quantify. If the reference flow was too large, the hydrocarbons would accumulate too quickly in the second test and exceed the range of the detection system, limiting the period over which accumulation could be measured and thus affecting the accuracy of the measured rate of accumulation.

At the completion of the test, a linear regression was fitted to the plot of hydrocarbon volume fraction divided by absolute temperature versus time. $\left. \frac{d}{dt} \left(\frac{y_{HC}}{T} \right) \right|_{t \rightarrow 0}$ was approximated as the slope of the linear regression.

Diagnostics

The facility was instrumented to monitor hydrocarbon concentration in the closed-loop wind tunnel, air speed and temperature in the lower test section, and gas flows to the burner and reference injection port. Figure 2.7 is a schematic of the diagnostics installation. Details of the diagnostics are contained in Appendices B and C.

Hydrocarbon concentration was measured with a 2 Rosemount NGA 2000 Flame Ionization Detectors, with ranges of 0 to 100 PPM methane and 0 to 250 PPM methane and resolutions of 0.02 PPM and 0.06 PPM, respectively. The choice of which

instrument was used was based on minimizing uncertainty without over-ranging the device.

Air speed in the lower test section was measured using a pitot tube. The pitot tube pressure was measured with a Setra Model 264 pressure transducer with a range of 2.54 mm water column and a Validyne DP-45 pressure transducer calibrated for a range of 25.4 mm water column. With these two pressure transducers the pitot tube was capable of measuring velocities ranging from 1 to 18 m/s. Pitot tube resolution was 0.05 m/s for the 3-15 m/s velocity range used in this study.

Air temperature was measured using an AD590 constant-current temperature transducer calibrated for a range of -50°C to 50°C with a resolution of 0.25°C .

Gas flow rates to the burner and reference injection port were measured and controlled with Omega mass flow controllers and Matheson mass flow meters. The burner gas flow rate was measured with an Omega FMA-775 flow controller calibrated for 0 to 100 slpm natural gas and a Matheson flow meter calibrated for 0 to 24.4 slpm natural gas. Meter resolutions were 0.02 slpm and 0.006 slpm, respectively. The reference injection port flow rates were metered using Omega FMA-760 flow controllers calibrated for ranges of 200 sccm, 1 slpm and 5 slpm methane with resolutions of 0.05 sccm, 0.0002 slpm and 0.001 slpm.

Data acquisition was conducted using a PC-based data acquisition system running National Instruments LabVIEW software. The PC was equipped with 2 12-bit National Instruments AT-MIO-16E-10 multiplexing data acquisition cards. The PC also controlled flow controllers and wind tunnel speed and purge systems through analog outputs.

Discussion of Uncertainty

In establishing a new experimental technique that involves several independent measurements it is important to estimate the expected uncertainty in the final results. An uncertainty analysis of Equation 2.13 determined that instrument error results in minor amounts of uncertainty in the calculated inefficiency, typically <5% of the calculated value. The analysis appears in Appendix D. The analysis considers the influence of uncertainty in fuel and reference hydrocarbon flow rate, fuel and reference hydrocarbon density, fuel and reference hydrocarbon composition, and rate of hydrocarbon accumulation in the wind tunnel.

The analysis determined that the most important source of uncertainty is in determining

the slope $\left. \frac{d}{dt} \left(\frac{y_{HC}}{T} \right) \right|_{t \rightarrow 0}$, typically an uncertainty of ~1-2% of the slope. The uncertainty

in this value dominates the cumulative uncertainty in measured inefficiency, with an influence which is 1-2 orders of magnitude larger than the influences of the other

uncertainties. The uncertainty in slope can be minimized by using hydrocarbon analyzers with high resolutions and by increasing the test length to gather more data points.

A sensitivity analysis was performed to determine how test length affects the calculated inefficiency. The inefficiency calculation was performed using progressively shorter sets of data from several inefficiency tests. The calculated inefficiency was plotted against test length to observe the variation in the results obtained as test length was decreased. As seen in Figure 2.8, the calculated inefficiency is essentially constant when test segments are greater than 400 seconds in length.

Experimental repeatability was determined by repeating some of the inefficiency measurements. These repeated tests can be seen in Figure 2.9, a plot of measured inefficiency of two flares plotted as a function of crosswind speed. Repeatability was generally good, with repeated tests falling within the boundaries of uncertainty determined by the uncertainty analysis.

Other potential sources for uncertainty are in the terms dropped from the mass balance for hydrocarbons. A high leakage/infiltration rate in the wind tunnel could result in those terms having a substantial impact on the measured inefficiency. However, as long as tests are kept short and background hydrocarbon concentrations are low, the leakage/infiltration terms are not significant.

Preliminary Test Results

Sets of tests were performed with the 25.4 mm burner at flow rates of 20 and 40 SLPM natural gas (94% methane with small fractions of propane and ethane) with varying cross-flow. Natural gas was also used as the reference gas. The results of these tests are plotted in Figure 2.9.

As expected, combustion inefficiency increases with increasing cross-flow. Inefficiency is very low (<1%) until some critical cross-flow speed at which inefficiency increases rapidly. Increasing the gas flow rate to the burner increases the cross-flow speed where inefficiency rises sharply. Changing the fuel flow rate has 2 immediate effects on the flame. It changes the momentum of the jet of fuel injected into the cross stream of air, and also increases the amount of energy released by the flame, affecting the buoyancy of the fuel jet.

At the gas flow rates used in these measurements, the relatively low gas momentum resulted in the flame becoming downwashed in the wake on the trailing edge of the burner. The downwashed flame is extremely stable and flame blow-off could not be achieved. Efficiency measurements were duplicated at low cross-flow speeds to check the repeatability of the measurement. The small variation in calculated efficiency reflects favorably on the repeatability.

Conclusions

The technique described here for measuring efficiency of jet diffusion flames in a cross-flow is an easily-implemented, reliable test method. Basing measurement of flame efficiency on a global balance of combustion products reduces uncertainties related to the plume sampling techniques used in previous measurements of diffusion flame efficiency. Conducting testing in a large, enclosed facility permits well-controlled test conditions. Preliminary results on a 25.4 mm O.D. pipe jet diffusion flame show that cross-flow can profoundly affect the flame.

Although currently implemented in a large wind tunnel, the method could conceivably be applied to any closed-loop structure for testing of flames. The use of two tests with differing rates of hydrocarbon accumulation compensates for any uncertainty in the volume of the test facility. The effect of leakage and destruction were shown to be negligible provided that the hydrocarbon volume fraction in the test facility is not too large.

This technique and facility would allow the variation of fuel flow and composition, cross-flow speed, turbulence levels both in the cross-flow and the fuel flow, burner geometry and scaling.

Notation

- AF_{st} = stoichiometric air/fuel ratio
- n_f = number of carbon atoms in a molecule of fuel
- n_{ref} = number of carbon atoms in a molecule of reference gas
- P = pressure inside wind tunnel (kPa)
- Q_f = fuel flow rate (m^3/s)
- Q_{in} = flow rate of ambient air into wind tunnel (m^3/s)
- Q_{out} = leakage of air from wind tunnel (m^3/s)
- Q_{ref} = reference gas flow rate (m^3/s)
- ρ = density of air inside wind tunnel (kg/m^3)
- ρ_f = density of fuel at conditions inside wind tunnel (kg/m^3)
- ρ_{HC} = density of hydrocarbons in the wind tunnel (kg/m^3)
- $\rho_{HC \infty}$ = density of hydrocarbons at ambient conditions (kg/m^3)
- R_{HC} = ideal gas constant for the hydrocarbon ($kJ/(kmol \cdot K)$)
- ρ_{ref} = density of reference gas inside wind tunnel (kg/m^3)
- T_{∞} = ambient temperature outside wind tunnel (K)
- T = temperature inside wind tunnel (K)
- V = volume of wind tunnel (m^3)
- y_{HC} = concentration of hydrocarbons (ppm)
- $y_{HC \infty}$ = background concentration of hydrocarbons (ppm)

References

Bourguignon, E., Flow & Turbulence Profiles of 25.4 mm Burner with Turbulence Generator, Private Communication, October 1997.

Brzustowski, T.A., "Flaring in the Energy Industry", *Prog. Energy Combust. Sci.*, 2, pp.129-141, 1976.

Brzustowski, T.A., "The Turbulent Diffusion Flame in a Cross-Wind", *Proceedings of the Fifth Canadian Congress of Applied Mechanics*, University of New Brunswick, Fredericton, 1975.

Gollahalli, S.R.; Brzustowski, T.A.; Sullivan, H.F.; "Characteristics of a Turbulent Propane Diffusion Flame in a Cross-Wind", *Transactions of the CSME*, 3, No. 4, pp.205-214, 1975.

Keller, Mike; Noble, Roger; "RACT for VOC - A Burning Issue", *Pollution Engineering*, July 1983, pp.20-23.

Kuipers, E.W.; Jarvis, B.; Bullman, S.J.; Cook, D.K.; McHugh, D.R.; Combustion Efficiency of Natural Gas Flares; Effects of Wind Speed, Flow Rate and Pilots, Shell Research and Technology Center Thornton & British Gas Research Center, 1996.

Obioh, I.B.; Oluwole, A.F.; Akeredolu, F.A.; “Non-CO₂ Gaseous Emissions From Upstream Oil and Gas Operations in Nigeria”, *Environmental Monitoring and Assessment*, 31, pp. 67-72, 1994.

Pohl, J.H.; Lee, J.; Payne, R.; Tichenor, B.A.; “Combustion Efficiency of Flares”, *Combustion Science and Technology*, 50, pp.217-231, 1986.

Romano, R.R.; “Control Emissions with Flare Efficiency”, *Hydrocarbon Processing*, October 1983, pp.78-80.

Stroscher, M.; Investigations of Flare Gas Emissions in Alberta, Environmental Technologies, Alberta Research Council, 1996.

Wilson, D.J.; Wind Tunnel Simulation of Plume Dispersion at Syncrude Mildred Lake Site, Environmental Research Monograph 1979-1, Syncrude Canada Ltd., 1979.

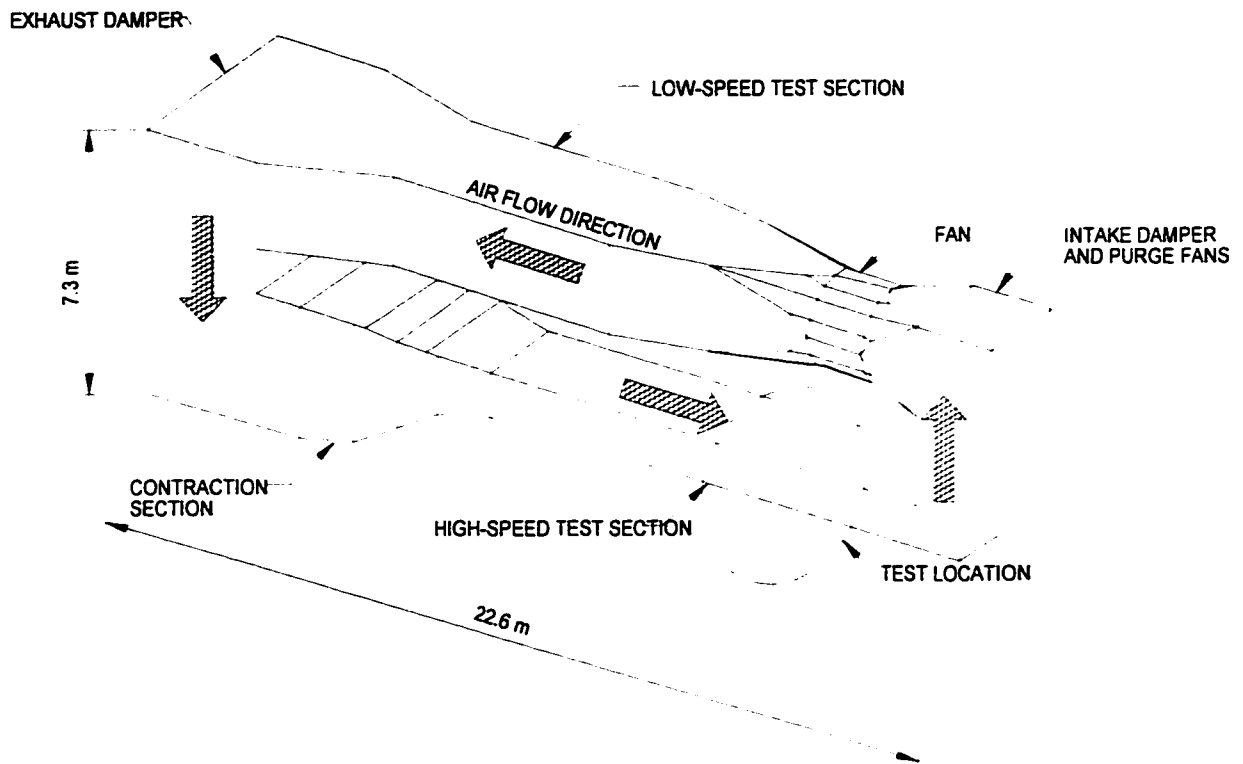


Figure 2.1 - Low Speed Wind Tunnel Facility used for Efficiency Measurements. The low-speed wind tunnel is a two story closed loop wind tunnel with two test sections. The diffusion flame experiments discussed in this paper were conducted in the high speed test section. The closed-loop configuration allows for the capture of all of the products of the diffusion flame, permitting determination of absolute quantities of products created by the flame.

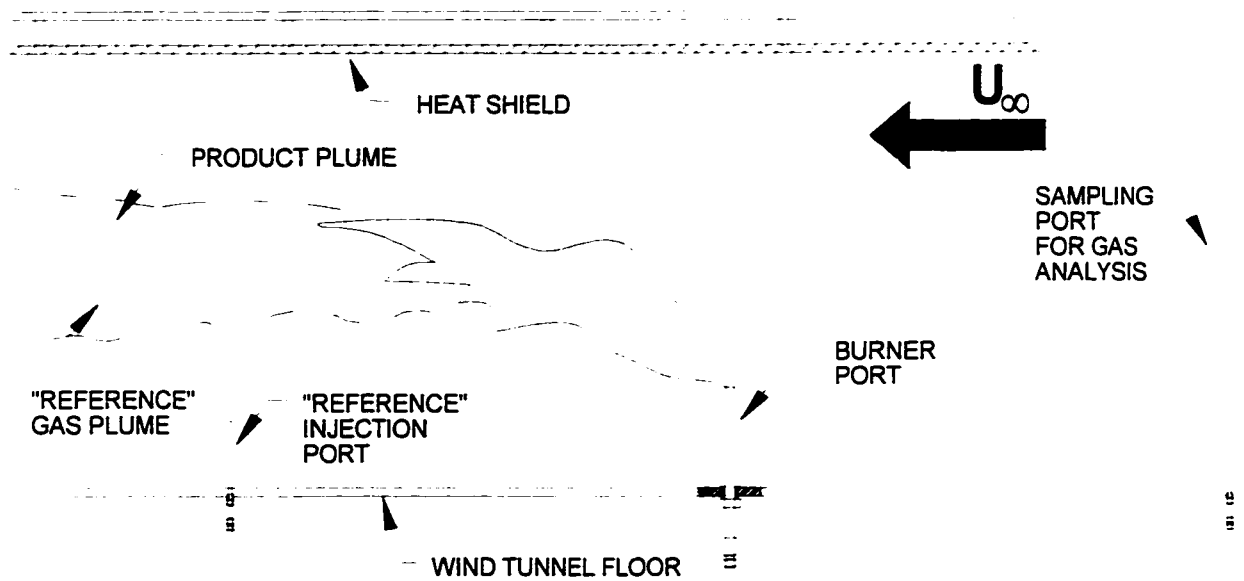


Figure 2.2 - Schematic of Experimental Set-Up. The burner is located 9.5 m from the leading edge of the high-speed test section of the wind tunnel, extending 300 mm into the test section. A heat shield is suspended from the tunnel roof to reduce heating from flame radiation and direct impingement of the flame. An injection port is located 1 m downstream of the burner to permit the introduction of a reference stream of hydrocarbons to the flame plume. The closed-loop configuration of the wind tunnel results in the constant recirculation of air, so a sampling port is located 3 m upstream of the burner to maximize the opportunity for flame products to mix with the tunnel air.

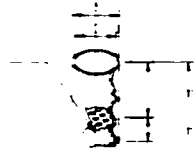


Figure 2.3 - Burner Configuration. The burner used in the experiments is a simple pipe with an outer diameter of 25.4 mm and an inner diameter of 22.1 mm. A turbulence generator is installed in the burner to create a turbulent pipe flow profile with 10% turbulence intensity for all flow rates, including Reynolds numbers where the flow would normally be laminar.

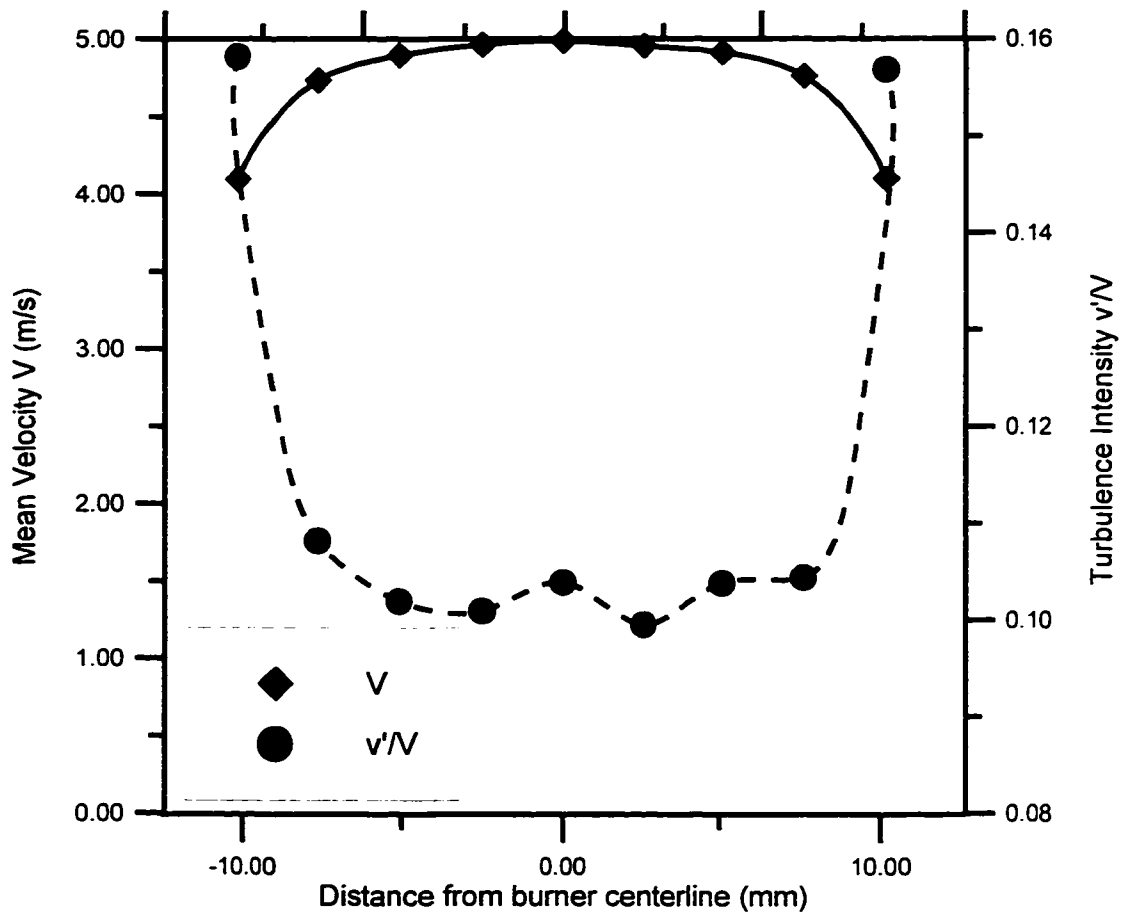


Figure 2.4 - Flow profile and turbulence intensity of 25.4 mm burner with turbulence generator. This plot was generated by a cold flow laser-doppler velocimeter traverse of the burner. The mean flow velocity of 4.8 m/s would normally produce a transitional pipe flow profile at the tip of the burner, but the turbulence plug creates a flat profile with ~10% turbulence intensity across a wide range of burner Reynolds number.

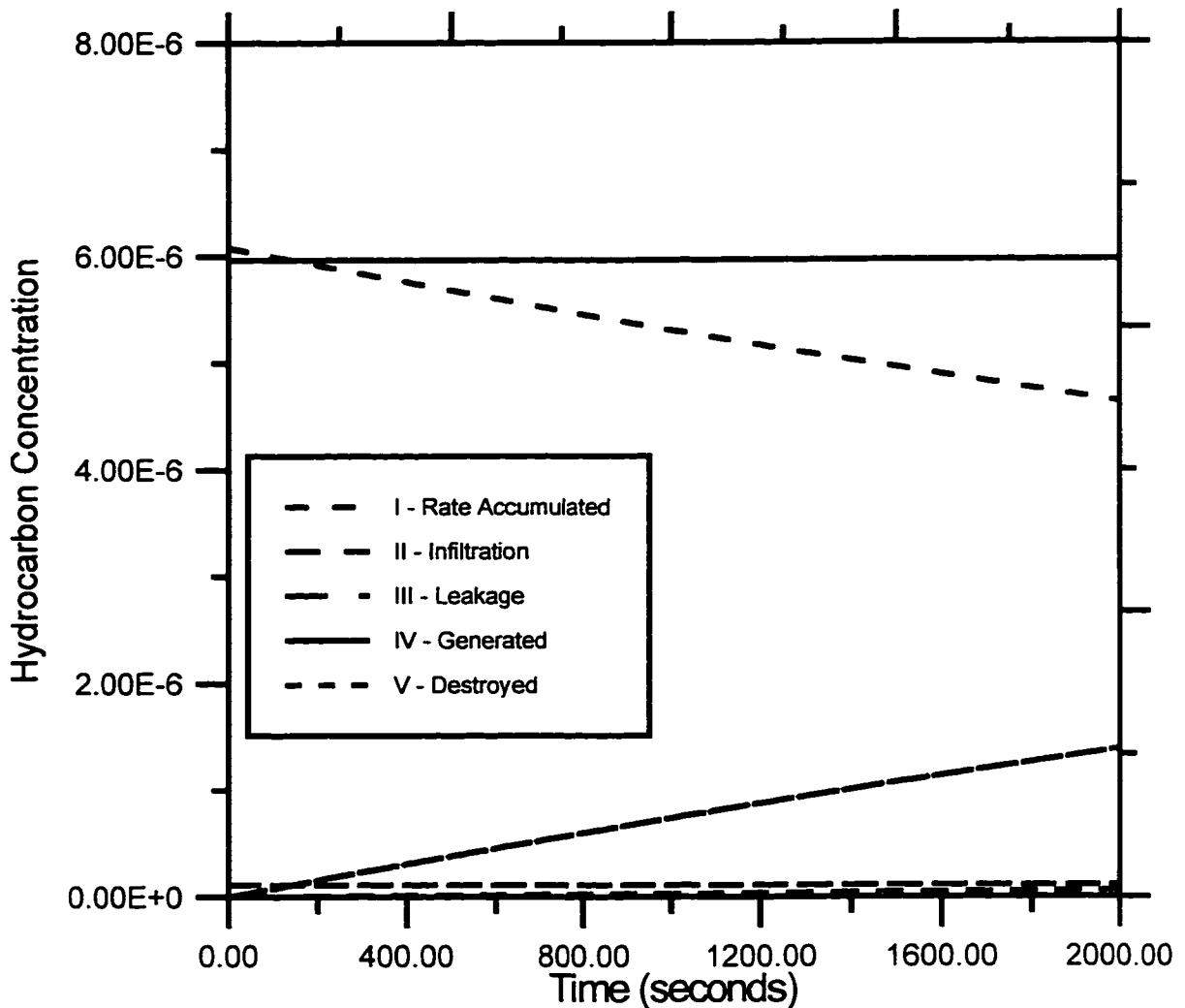


Figure 2.5 - Comparison of terms in wind tunnel mass balance equation. This graph is a model based upon a flame destruction inefficiency of 0.025, a fuel supply rate of 20 slpm methane, and a tunnel air infiltration rate of 0.65 air changes per hour with an ambient hydrocarbon concentration of 2.5 ppm. This model shows that the effects of infiltration, leakage and destruction in the wind tunnel mass balance equation are initially small.

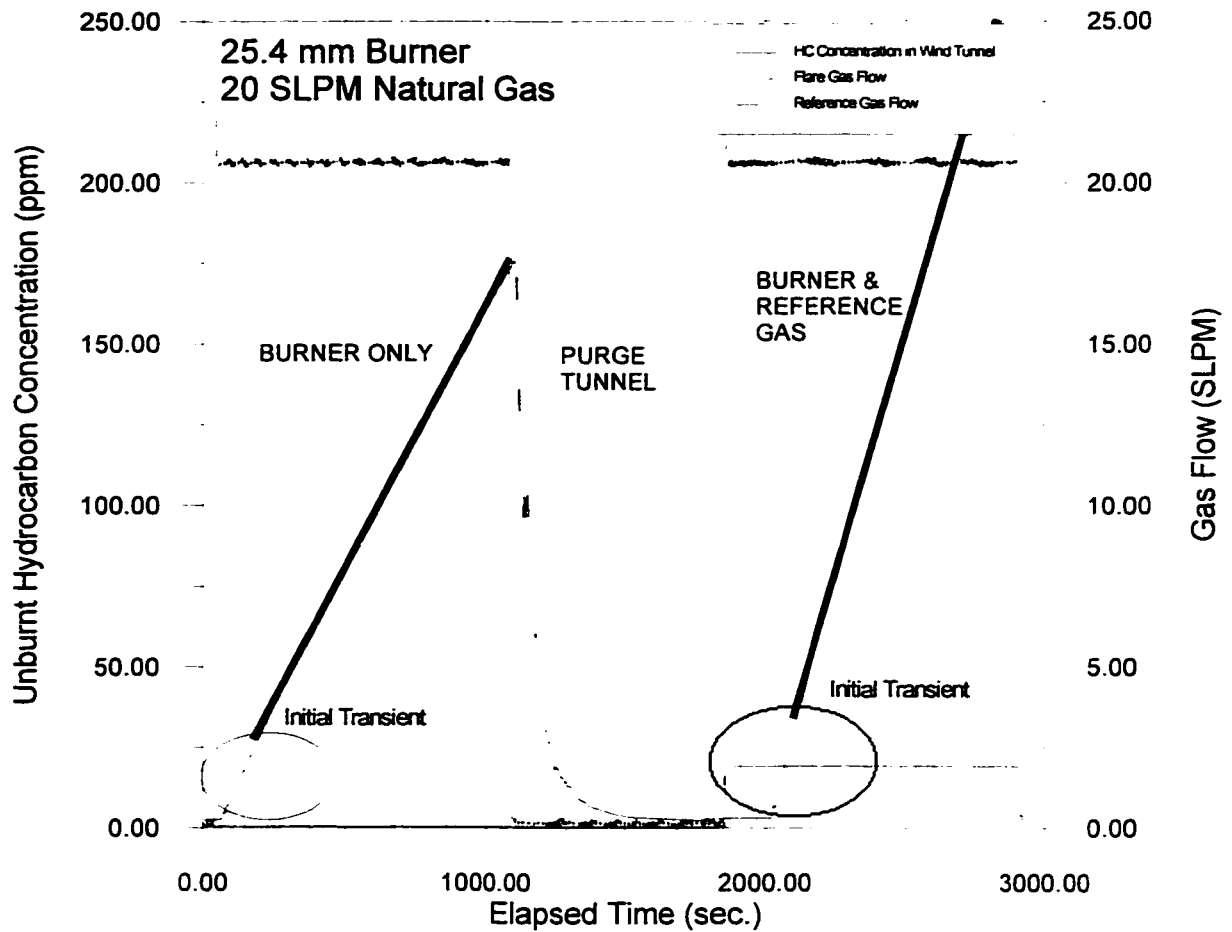


Figure 2.6 - Hydrocarbon concentration and gas flow rates for a typical test. This is plot of the hydrocarbon concentration measured during an efficiency test of a 20 slpm natural gas jet diffusion flame. This plot shows the three segments required for each flame efficiency measurement: burning the flame, purging the tunnel of products, and repeating the first segment with the addition of a stream of reference hydrocarbons. Each burn segment is accompanied by an initial transient resulting from the time lag required for mixing of the flame products with the wind tunnel air.

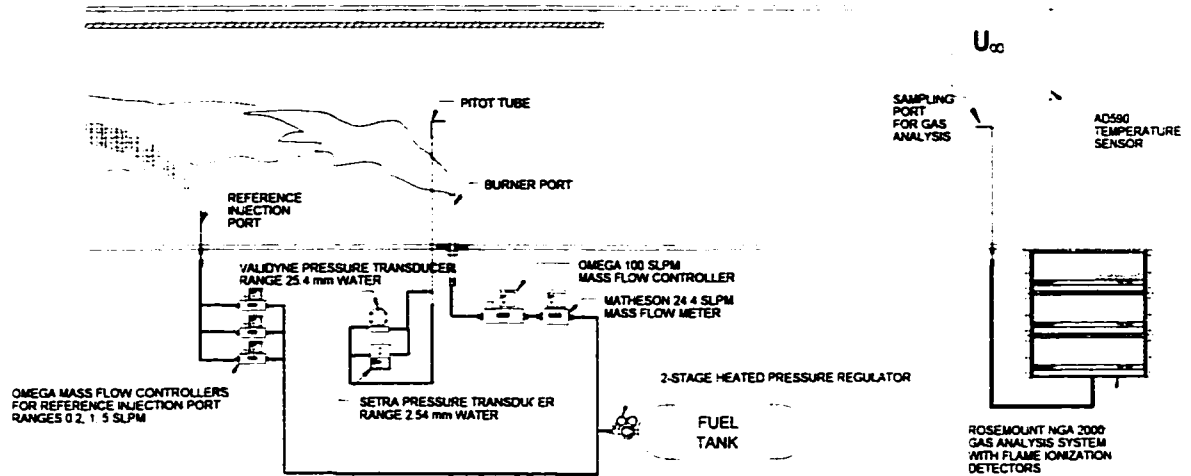


Figure 2.7 - Schematic of experimental diagnostics installation. The flame inefficiency measurement requires the measurement of fuel and reference gas flow rates, hydrocarbon concentration in the wind tunnel, and the air speed and temperature inside of the wind tunnel. Fuel and reference gas flow rates are measured using mass flow controllers. Hydrocarbon concentration is measured using flame ionization detectors sampling from a port 3 m upstream of the flame. Air speed in the wind tunnel is measured with a pitot tube adjacent to the burner. Air temperature is measured with a constant-current temperature transducer located 3 m from the leading edge of the test section.

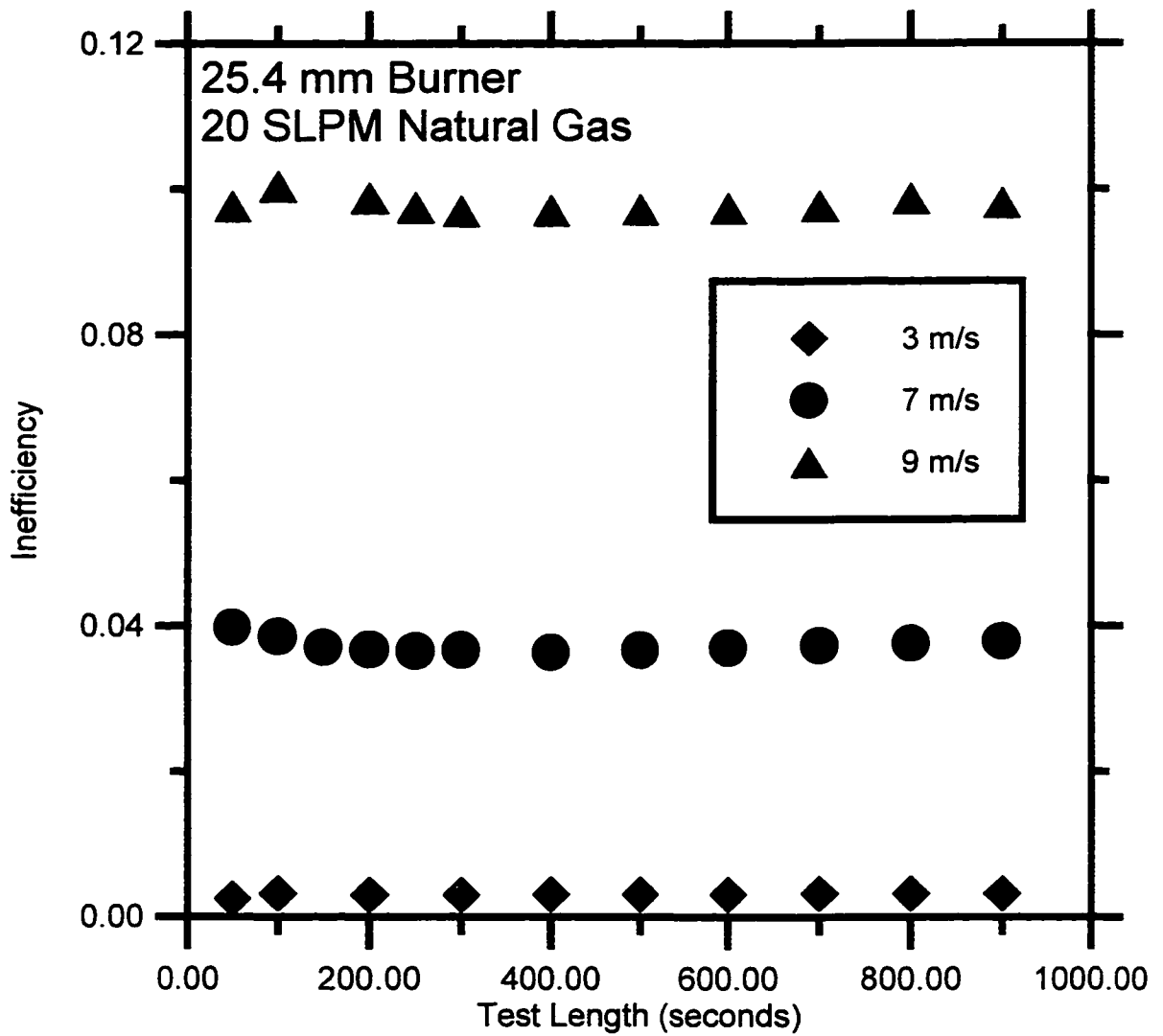


Figure 2.8 - Effect of test length on measured inefficiency. A sensitivity analysis was performed on data sets from a 20 slpm natural gas jet diffusion flame to determine the effect of test length on calculated flame inefficiency. The data sets used were from inefficiency measurements at cross-flows of 3, 7 and 9 m/s. The plot above shows the variation in the flame efficiency computed with progressively longer data sets. After test length reaches 400 s, the value obtained for flame inefficiency becomes relatively constant.

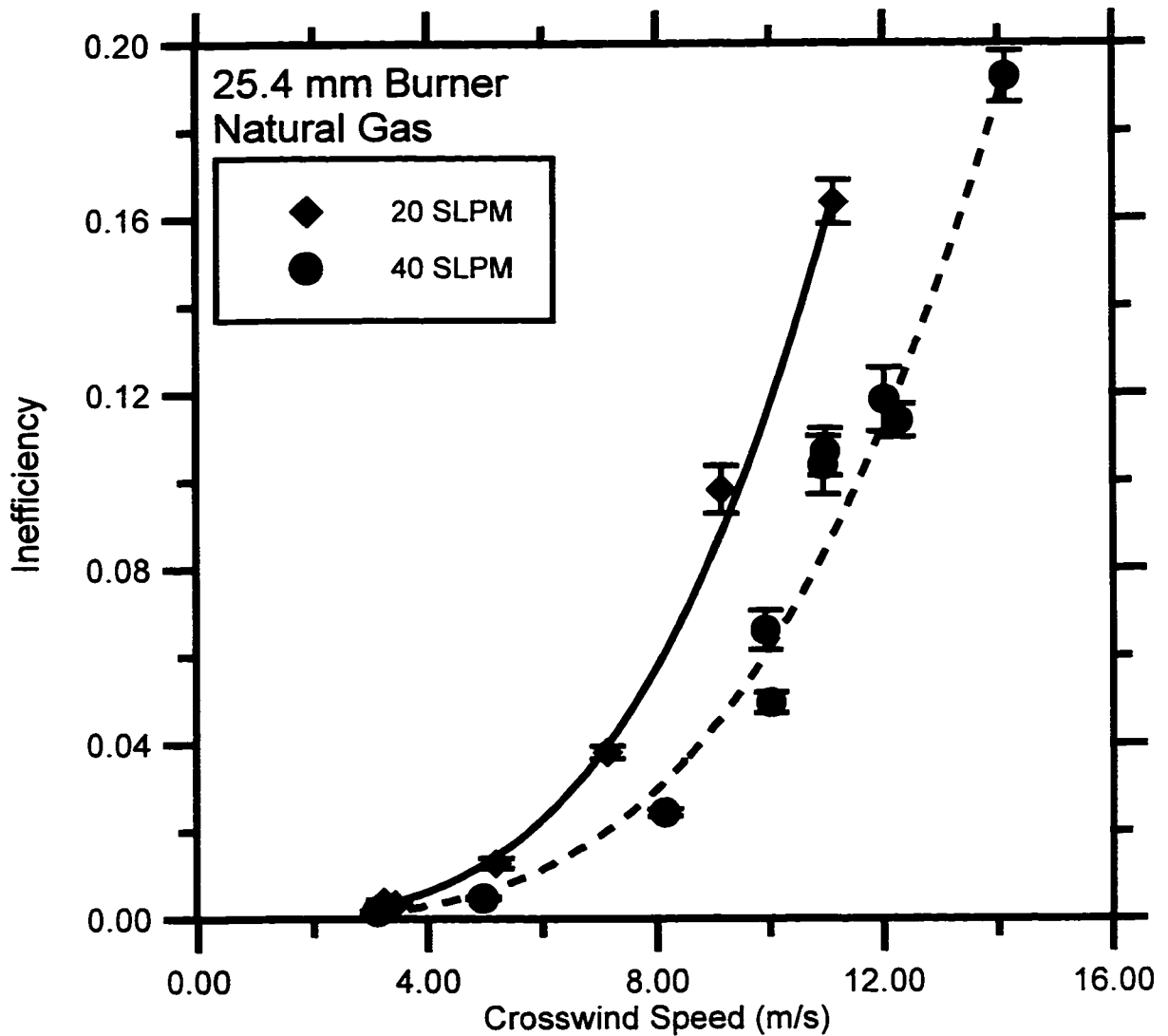


Figure 2.9 - Inefficiency of flame as a function of cross-flow speed for two fuel flow rates. This plot shows the increase in flame inefficiency with increasing cross-flow speed. Inefficiency is very low until a critical cross-flow speed is attained, after which inefficiency increases sharply. Comparing the curves for the two flow rates indicates that a higher fuel flow rate delays the onset of the rapid increase in inefficiency.

Chapter 3 - Efficiency of Natural Gas Flares In Cross-Winds

Introduction

Flaring is widely used in the energy and petrochemical industries to destroy combustible waste gases. As many of these waste gases pose environmental or explosion hazards, they must be destroyed reliably. Research conducted prior to 1996 has concluded that flares burn fuel at efficiencies greater than 98% except near blow-off [Pohl et. al., 1986]. However, these tests were conducted in quiescent environments and considered only gaseous fuels. More recent research has indicated that flares could have efficiencies as low as 64% [Stroscher, 1996]. Unfortunately, these investigations were conducted under field conditions, and test parameters like wind speed, gas composition, gas flow rate and inclusion of liquid hydrocarbons were poorly controlled or unknown. As a result the quantitative question of the effects of wind on flare efficiency relative to other sources of inefficiency was left unanswered.

The behavior of flares has been studied for more than a half century. Initial research focused on characterizing the shape, flame modes, radiation field and stability limits of the flames in order to develop procedures for the design of industrial flares [Gollahalli et. al., 1975; Brzustowski, 1975; Brzustowski, 1976; Kalghati, 1983]. With the advent of stricter environmental regulations in the 1970s' and 1980s', studies shifted to the

effectiveness of a flare at destroying waste gases from industrial and petrochemical operations.

Major studies of flare efficiencies have been conducted in the United States of America by the Chemical Manufacturers' Association (CMA) [Keller et. al., 1983; Romano, 1983] and the Environmental Protection Agency (EPA) [Pohl, 1986]; in Europe by Shell Research and British Gas [Kuipers et. al., 1996], and in Canada by the Alberta Research Council (ARC) [Stroscher, 1996].

Several definitions of flare efficiency have been used, including destruction efficiency or combustion efficiency. Destruction efficiency (η_d) accounts for the fraction of a species or group of species that exists in the reactant stream that are destroyed by the flare.

$$\eta_d = \frac{\text{mass flow rate of species } i \text{ in products}}{\text{mass flow rate of species } i \text{ in reactants}} \quad 3.1$$

For example, a methane destruction efficiency would be defined as the amount of methane contained in the flare products divided by the amount of methane delivered to the flare as fuel. Combustion efficiency (η_c) based on carbon measures the fraction of carbon atoms that are not fully oxidized in the reactant stream (e.g. hydrocarbons, CO) that become fully oxidized (CO₂) by the flare.

$$\eta_c = \frac{\text{Mass flow rate of fully oxidized carbon produced by the flare}}{\text{Total mass flow rate of carbon in reactants not as CO}_2} \quad 3.2$$

The destruction efficiency is often an adequate measure of flare performance if the flare is being used to destroy a hazardous substance [Pohl, 1986]. Carbon-based combustion efficiency is a more conservative assessment of flare efficiency. Species considered

destroyed under the definition of destruction efficiency may have been converted to either toxic products such as carbon monoxide or polynuclear aromatic hydrocarbons (e.g. benzal pyrene, ethynyl benzene or cyclohexane). The definition of combustion efficiency does not consider the flare to be efficient unless all of the carbon-based components have also been destroyed by complete oxidization to carbon dioxide. However, destruction efficiency and combustion efficiency have been found to be closely related; a high destruction efficiency generally implies a high combustion efficiency [Pohl, 1986].

Research into the efficiency of flares has been conducted under both laboratory and field conditions. The laboratory conditions typically allow for good control of fuel flow rate and ambient conditions, but result in lack of wind effects and limit the size of flare that can be investigated. Field conditions permit testing of large flares under operational conditions, but typically suffer from poor control of test conditions such as wind speed and from the difficulty of instrumenting a large flame 10-30 meters above ground level.

The size of the large flares encountered in field tests means that flare efficiency measurements are typically based on sampling of flare products at a single point from the flare plume. The smaller flares employed in laboratory tests permit more sophisticated methods of sampling such as hood sampling that provide a more homogeneous sample from the flare plume.

Most flare efficiency tests have been conducted under field conditions both because the size of industrial flares complicates laboratory tests and because the use of an existing flare eliminates the expense of constructing a test item. A major study was conducted by the CMA in 1983 at a large industrial flare located at a refinery [Romano, 1983; Keller, 1983]. Other field studies have been conducted since in Nigeria [Obioh et. al., 1993], by the ARC [Stroscher, 1996], and by Shell Research and British Gas [Kuipers et. al., 1996]. In all studies except the ARC the efficiency was reported to be >95%. The ARC study found efficiencies as low as 64% [Stroscher, 1996].

Laboratory conditions allow good control of test parameters, however only a limited number of tests have been performed under laboratory conditions.. The ARC conducted some small-scale laboratory whose primary purpose was to develop an experimental technique that could be used in pilot scale and field parts of the study. These laboratory tests were restricted in the size of flames which could be tested (0.1-3.0 mm) and lacked a suitable method for creating a cross-flow [Stroscher, 1996]. The EPA studied full-sized flares (37-300 mm diameter) outdoors but under what were essentially laboratory conditions in the early 1980s' at its large scale test facility, but did not investigate wind effects [Pohl, 1986]. Both of these studies resulted in efficiencies >95% as long as they were conducted in quiescent conditions.

Previous studies into flare efficiency have not focused on wind effects. Several of the studies purposely avoided wind effects [Pohl, 1986]. Studies conducted on flare

geometry recognized that a cross-flow altered flame shape, but efficiency studies have assumed implicitly that a change in flame shape has no impact on efficiency. Some of the field studies were conducted with mild winds, but none of the studies performed a systematic investigation into wind effects [Stroscher, 1996; Kuipers et. al., 1996].

Another key question is how results obtained from small laboratory scale tests scale up to much larger industrial flares. With the exception of the EPA studies, laboratory-based flare experimentation has been limited to flares less than 25.4 mm in diameter. In contrast, industrial flares range in size from 100 mm to 3 m in diameter [Pohl, 1986]. Laboratory tests are well-suited to parametric studies of flare behavior, but are of little use if they cannot be correlated to the large flares used by the energy and petrochemical industries.

In the current study a laboratory-based method was developed for measuring the hydrocarbon destruction efficiency of a well-controlled scaled-down flare in a cross-wind. The method had the combustion occur in a large closed-circuit wind tunnel and measured the build-up of combustion products in the wind tunnel. The rate of accumulation of unburned fuel in the wind tunnel was used to determine the efficiency of the flare at a given wind speed. Destruction efficiency was measured for two different size pipe flares at varying fuel flows and wind speeds. Modeling a flare as a buoyant plume allowed efficiency to be correlated with a power law that related the flare exit velocity and the wind speed.

Experimental Methodology

A scaled-down model of a pipe flare was operated in a closed-loop wind tunnel under the influence of a steady cross-wind with low turbulence intensity. A schematic view of the experimental set-up is depicted in Figure 3.1. The destruction efficiency (I_d) of the flare was determined by conducting a hydrocarbon mass balance on the wind tunnel. The mass balance considered several influences

- ◆ The rate at which hydrocarbons escaped combustion in an inefficient flare
- ◆ Dilution of the hydrocarbon mass fraction in the wind tunnel by infiltration of external air and leakage of products from the wind tunnel
- ◆ Destruction of hydrocarbons that initially escaped combustion but were consumed when recirculated past the flare

As the scale flare burned, the accumulation of unburned fuel in the wind tunnel was measured with two Rosemount NGA 2000 flame ionization detectors. After measuring the accumulation for 15 minutes, the tunnel was purged of the combustion products and the flare re-lit while a known mass flow rate of flare gases was added to the wind tunnel as a “reference” from a separate injection port. By comparing the accumulation rates of the flare and the flare plus reference gas, the hydrocarbon destruction inefficiency of the flare was determined using the equation

$$I_d = 1 - \eta_d = \frac{Q_{ref}}{Q_f} \left(\frac{\frac{d}{dt} \left(\frac{y_{HC}}{T(t)} \right)_{ref} \Big|_{t \rightarrow 0}}{\frac{d}{dt} \left(\frac{y_{HC}}{T(t)} \right) \Big|_{t \rightarrow 0}} - 1 \right)^{-1} \quad 3.3$$

where

η_d = destruction efficiency of flare

y_{HC} = volume fraction of hydrocarbons in wind tunnel (ppm)

T = temperature inside wind tunnel (K)

Q_f = fuel flow rate (slpm)

Q_{ref} = reference gas flow rate (slpm)

$t \rightarrow 0$ refers to a time early in the experiment after an initial mixing transient but before the accumulated volume fraction of hydrocarbons becomes large enough to significantly influence the rate of accumulation of hydrocarbons in the wind tunnel.

A description of the experimental facility and this measurement technique is found in Chapter 2.

Flares Tested

The flares investigated in this study had a simple open-pipe geometry with no tip modifications. Two sizes of flares were investigated: a pipe with an outside diameter of

25.4 mm and an inside diameter of 22.1 mm, and a pipe with an outside diameter of 12.7 mm and an inside diameter of 11.0 mm. Both pipe flares terminate 300 mm above the floor of the wind tunnel.

The focus of work was the 25.4 mm flare fitted with a turbulence generator. The generator is a perforated plug installed in the pipe that creates a turbulent pipe flow profile with 10% RMS turbulence, similar to the fully turbulent pipe profile in an industrial flare [Bourguignon, 1997]. Details of the turbulence generator are given in Chapter 2.

A secondary set of experiments was conducted using the 12.7 mm flare. An appropriate turbulence generator was not available for the 12.7 mm flare at the time of testing. For the Reynolds numbers encountered during testing ($Re_d=700-11000$), the 12.7 mm flow profile varied from a laminar profile to a turbulent pipe profile. Not having a turbulence generator for the 12.7 mm flare prevents an unambiguous comparison between the two scales of flares. However, having the flow vary from laminar to turbulent allows questions to be addressed regarding the importance of the flow profile of flare gases.

Experimental Results

The flares burned sales-grade natural gas (>96 % methane) [Johnson, 1995] at flow rates of 5, 10, 20, 40 and 80 slpm. Efficiencies were measured for each flow rate at wind

speeds ranging from 3 m/s to a sufficiently high wind speed for the flare to burn inefficiently, $1-\eta_d > 16\%$.

Figure 3.2 is a plot of the inefficiency of the 25.4 mm flare at varying fuel flow rates plotted against wind speed. Examination of the plot reveals that the curves of constant flow rate have similar shapes, with very low inefficiency at low wind speed and inefficiency increasing monotonically with wind speed. The inefficiency remains less than 1% until some critical wind speed where the inefficiency begins to increase dramatically. This critical wind speed increases with increasing fuel flow rate, demonstrating that an increased flow rate decreases a flare's susceptibility to wind. At least one data point was repeated for each fuel flow rate to verify the repeatability of the measurements. The repeated points showed good agreement with previous results.

When plotted on a log-log scale, Figure 3.2 becomes a series of straight lines in Figure 3.3, indicating that flare inefficiency has a power-law dependency on wind speed. The power law exponent for each flow rate is shown in Table 3-1. The first two flow rates exhibit a fit to the power of 2 while the three higher flow rates are fitted with a power law of 3. Exponential behavior was also considered as a possible correlating function but was not an appropriate form.

Table 3-1 - Power law exponents for plots of 25.4 mm flare inefficiency as a function of wind speed

Fuel Flow Rate (slpm)	Mean Air Velocity (m/s)	Power Law Exponent on U
5	4.28	1.776
10	5.04	2.172
20	5.88	3.201
40	8.90	3.299
80	7.46	3.167

Many of the trends observed with the 25.4 mm flare are repeated with the 12.7 mm flare. Figure 3.4 plots the inefficiency of the 12.7 mm flare against wind speed. Again, the curves for varying fuel flow rates have similar shapes and exhibit a rapid increase in inefficiency after some critical wind speed is surpassed. The similarity between the behavior of the 12.7 mm and 25.4 mm flares suggest that these effects exist over a range of scales. The efficiency of the small flare is much more susceptible to wind than the larger flare. Plotting Figure 3.4 on a log-log scale in Figure 3.5 again produces a set of straight lines, reinforcing the idea of a power-law dependency. The power law exponent for each flow rate is shown in Table 3-2. The 12.7 mm flare does not exhibit the sharp difference between flow rates for power law exponents as seen in Table 3-1 for the 25.4 mm flare. Instead, the power law exponent varies about an exponent of 2.5.

Table 3-2 - Power law exponents for plots of 12.7 mm flare inefficiency as a function of wind speed

Fuel Flow Rate (slpm)	Mean Air Velocity (m/s)	Power Law Exponent on U
5	5.67	2.634
10	6.30	2.681
20	7.10	2.125
40	6.53	2.739
80	6.11	2.093

Interpretation of Results

To interpret the results of these investigations into flare inefficiency, a functional relation is required to define the interaction between flare exit velocity, crosswind speed and the scale(s) of the experiment. A jet diffusion flame such as a flare is a turbulent, buoyant, reacting plume whose structure is dominated by entrainment and mixing. Non-reacting buoyant plume research [Briggs, 1975] has comprehensively studied the interaction between the jet flow and cross-flow. These studies have identified two major regimes of interaction to aid interpretation of plume behavior (e.g. trajectory, spread, dispersion, etc.). One regime is set by the relative momentum flux of the jet flow and the free stream. The other region is set by the momentum of the free stream and the buoyancy of the plume.

Momentum-Based Correlation

Previous research has attempted to correlate flare behavior to ratios of flare gas and wind momentum [Brzustowski, 1975; Kalaghati, 1983]. The use of momentum as a basis for correlations was not particularly successful. A momentum-based model for flame length by Brzustowski usually was in error by a factor of 2 [Brzustowski, 1976]. Momentum is expressed in terms of the ratio of air momentum to fuel momentum,

$$M = \frac{\rho_{\infty}^{\frac{1}{2}} U_{\infty}}{\rho_f^{\frac{1}{2}} V_f} \quad 3.4$$

where

M = ratio of wind momentum to fuel momentum at flare tip

ρ_{∞} = air density (kg/m³)

U_{∞} = wind speed (m/s)

ρ_f = flare fuel density (kg/m³)

V_f = average fuel velocity at flare tip (m/s)

The flare efficiency data is plotted against M in Figure 3.6 for the 25.4 mm diameter flare. The spread of the data has not been improved by the momentum correlation and means that a ratio of flare exit velocity and crosswind speed raised to the same power is not an appropriate scaling factor.

Buoyancy-Based Correlation

Other recent research indicates that buoyancy has a major influence on the behavior of jet diffusion flames such as flares. Full-sized flares have Richardson numbers on the order

of 10^3 to 10^4 [Pohl et. al., 1986], and recent microgravity experiments have confirmed that buoyancy dominates jet diffusion flame behavior [Bahadori et. al., 1993]. Therefore, it seems reasonable to attempt to correlate the behavior of a flare under the influence of wind to the behavior of a buoyant plume in a cross-flow.

The rise of a buoyant plume from a point source is given by Briggs (1975),

$$\Delta h_b = B_1 \frac{F_b^{\frac{1}{3}} x_b^{\frac{2}{3}}}{U_\infty} \quad 3.5$$

where

Δh_b = vertical distance between plume tip and plume centerline (m)

x_b = distance downstream of flare stack (m)

F_b = buoyancy flux (m^4/s^3)

U_∞ = cross wind speed (m/s)

B_1 = constant

Figure 3.7 is a schematic of a buoyant plume that defines Δh_b at x_b .

The buoyant flux can be expressed as a relation of the chemical energy release by the flame:

$$F_b = \left(\frac{g \bar{R}_\infty}{\pi C_{p_x} P_\infty} \right) H_s \quad 3.6$$

where

$H_s = \rho_f Q_f q_r =$ flare chemical energy release rate (J/s)

$\rho_f =$ density of fuel at ambient conditions (kg/m³)

$Q_f =$ flow rate of fuel (m³/s)

$q_r =$ enthalpy of reaction of fuel & air (J/kg)

$g = 9.81$ m/s²

$R_\infty =$ ideal gas constant for air (kJ/(kmol*K))

$C_{p,\infty} =$ heat capacity of air (J/kg)

$P_\infty =$ atmospheric pressure (kPa)

Treating the fuel flow from the flare stack as having a top-hat velocity profile, Q_{fuel} can be expressed as a function of average exit velocity of the fuel and the flare diameter, essentially modeling turbulent pipe flow. By making this substitution and non-dimensionalizing the length scales with d , Equation 3.4 becomes

$$\frac{\Delta h_b}{d} = B_2 \left(\rho_f q_r \frac{\pi}{4} \right)^{\frac{1}{3}} \left(\frac{V_f^{\frac{1}{3}} d^{\frac{1}{3}}}{U_\infty} \right) \left(\frac{x_b}{d} \right)^{\frac{2}{3}} \quad 3.7$$

where

$B_2 =$ combined constant

$d =$ flare tip flow diameter (m)

$V_f =$ average fuel velocity at flare tip (m/s)

Equation 3.7 introduces the physical scaling in the analysis. In order to maintain the same flame shape for the full-scale flare and the scale model when the same fuel is used,

$$\frac{V_f^{1/3} d^{1/3}}{U_\infty} = \text{constant}$$

This maintains the same normalized flame height $\Delta h_f/d$ at a given normalized position x/d .

To test the relation given in Equation 3.8, the inefficiency data for the 25.4 mm and 12.7 mm flares from Figures 3.2 to 3.5 is replotted against Equation 3.8 in Figures 3.8 and 3.9, respectively. The data for the 25.4 mm flare plotted in Figure 3.8 shows a strong convergence about a single line. This convergence is evidence that flare inefficiency is strongly linked to flame shape. By correcting for the different flame shapes using Equation 3.8, the 25.4 mm flare data for different fuel flow rates has converged on a single line.

The data for the 12.7 mm flare in Figure 3.9 does not converge as well. This difference may be associated with the lack of a turbulence generator for the 12.7 mm flare. Without a turbulence generator, calculations show that the gas flow velocity profile at the tip of the 12.7 mm flare can be expected to vary from laminar to turbulent as gas flow rate increases. This change in velocity profile could possibly affect the mixing of fuel and air at the flare tip, as the momentum flux is higher for a laminar profile than a turbulent or transitional profile at the same average velocity.

Plotting the inefficiencies of the 12.7 mm and 25.4 mm flares against wind speed in Figure 3.10, the data points are spread in several curves across the plot. By replotting the

inefficiency data against Equation 3.8, the data points collapse onto a single line in Figure 3.11. This seems to confirm that a flare and a buoyant plume exhibit similar behavior over the range of conditions tested.

Using Equation 3.8 to create a predictive scaling rule for buoyancy dominated flares for the same cross wind speed between full and model scales gives:

$$V_{f,model} = \left(\frac{d_{full\ scale}}{d_{model}} \right) V_{f,full\ scale} \quad 3.9$$

Extending this further, Equation 3.7 could be used to translate the behavior of a scale flare to a full-sized flare. From Equation 3.7, the 25.4 mm flare burning 80 SLPM exhibits the same inefficiency behavior as a 100 mm flare burning 454 m³ of gas per day, a common flare used at oil wells in Alberta.

Conclusions

Most studies conducted previously have concluded that flare efficiency is greater than 98% in all conditions. This study has shown that flare efficiency is dependent on wind speed. Flare efficiency is very high until some critical wind speed is attained after which efficiency drops off as a function of wind speed to the third power.

By treating the flare as a combustion process governed by air entrainment of a buoyant plume, a relationship has been derived between flare efficiency, wind speed, flare

diameter and fuel exit velocity. The relationship produces good agreement with experimental results, and could be used to translate the results obtained with small laboratory scale flare models to large industrial flares.

References

Bahadori, M.Y.; Stocker, D.P.; Vaughan, D.F.; Zhou, L.; Edelman, R.B.; "Effects of Buoyancy on Laminar, Transitional, and Turbulent Gas Jet Diffusion Flames", Second International Microgravity Combustion Workshop, NASA, 1993.

Bourguignon, E., Flow & Turbulence Profiles of 25.4 mm Burner with Turbulence Generator, Private Communication, October 1997.

Briggs, G.A.; "Plume Rise Predictions", in *Lectures on Air Pollution and Environmental Impact Analyses*, Workshop Proceedings, American Meteorological Society, pp. 59-111, , Sept. 29 - Oct. 3 1975.

Brzustowski, T.A., "Flaring in the Energy Industry", *Prog. Energy Combust. Sci.*, 2, pp.129-141, 1976.

Brzustowski, T.A., "The Turbulent Diffusion Flame in a Cross-Wind", *Proceedings of the Fifth Canadian Congress of Applied Mechanics*, University of New Brunswick, Fredericton, 1975.

Gollahalli, S.R.; Brzustowski, T.A.; Sullivan, H.F.; "Characteristics of a Turbulent Propane Diffusion Flame in a Cross-Wind", *Transactions of the CSME*, 3, No. 4, pp.205-214, 1975.

Johnson, M.R.; Development of a Low Emissions, Lean Premixed, Natural Gas Burner,
M.Sc. Thesis, University of Alberta, 1995.

Kalghati, G.T.; "The Visible Shape and Size of a Turbulent Hydrocarbon Jet Diffusion
Flame in a Cross-Wind", *Combustion and Flame*, 52, pp.91-106, 1983.

Keller, Mike; Noble, Roger; "RACT for VOC - A Burning Issue", *Pollution Engineering*,
July 1983, pp.20-23.

Kuipers, E.W.; Jarvis, B.; Bullman, S.J.; Cook, D.K.; McHugh, D.R.; Combustion
Efficiency of Natural Gas Flares; Effects of Wind Speed, Flow Rate and Pilots, Shell
Research and Technology Center Thornton & British Gas Research Center, 1996.

Obioh, I.B.; Oluwole, A.F.; Akeredolu, F.A.; "Non-CO₂ Gaseous Emissions From
Upstream Oil and Gas Operations in Nigeria", *Environmental Monitoring and
Assessment*, 31, pp. 67-72, 1994.

Pohl, J.H.; Lee, J.; Payne, R.; Tichenor, B.A.; "Combustion Efficiency of Flares",
Combustion Science and Technology, 50, pp.217-231, 1986.

Romano, R.R.; "Control Emissions with Flare Efficiency", *Hydrocarbon Processing*,
October 1983, pp.78-80.

Strosher, M.; Investigations of Flare Gas Emissions in Alberta, Environmental Technologies, Alberta Research Council, 1996.

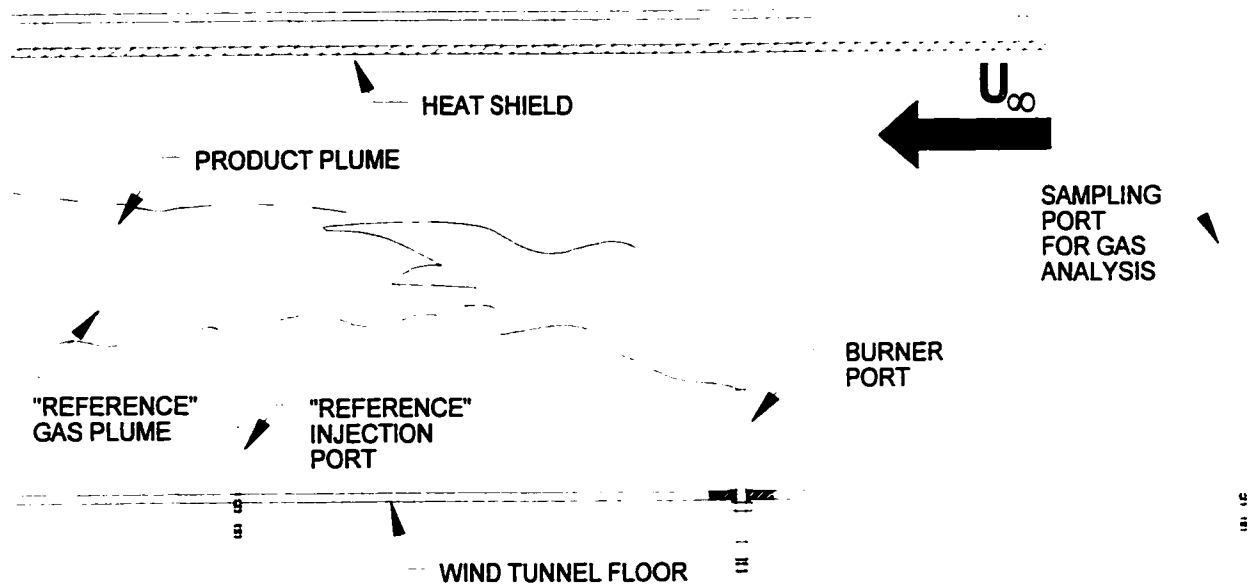


Figure 3.1 - Schematic of experimental set-up used to measure flare efficiency. The experiment was conducted in the high-speed test section of a closed-loop wind tunnel. The closed-loop configuration allows for the capture of all of the products of the diffusion flame, permitting determination of absolute quantities of products created by the flame.

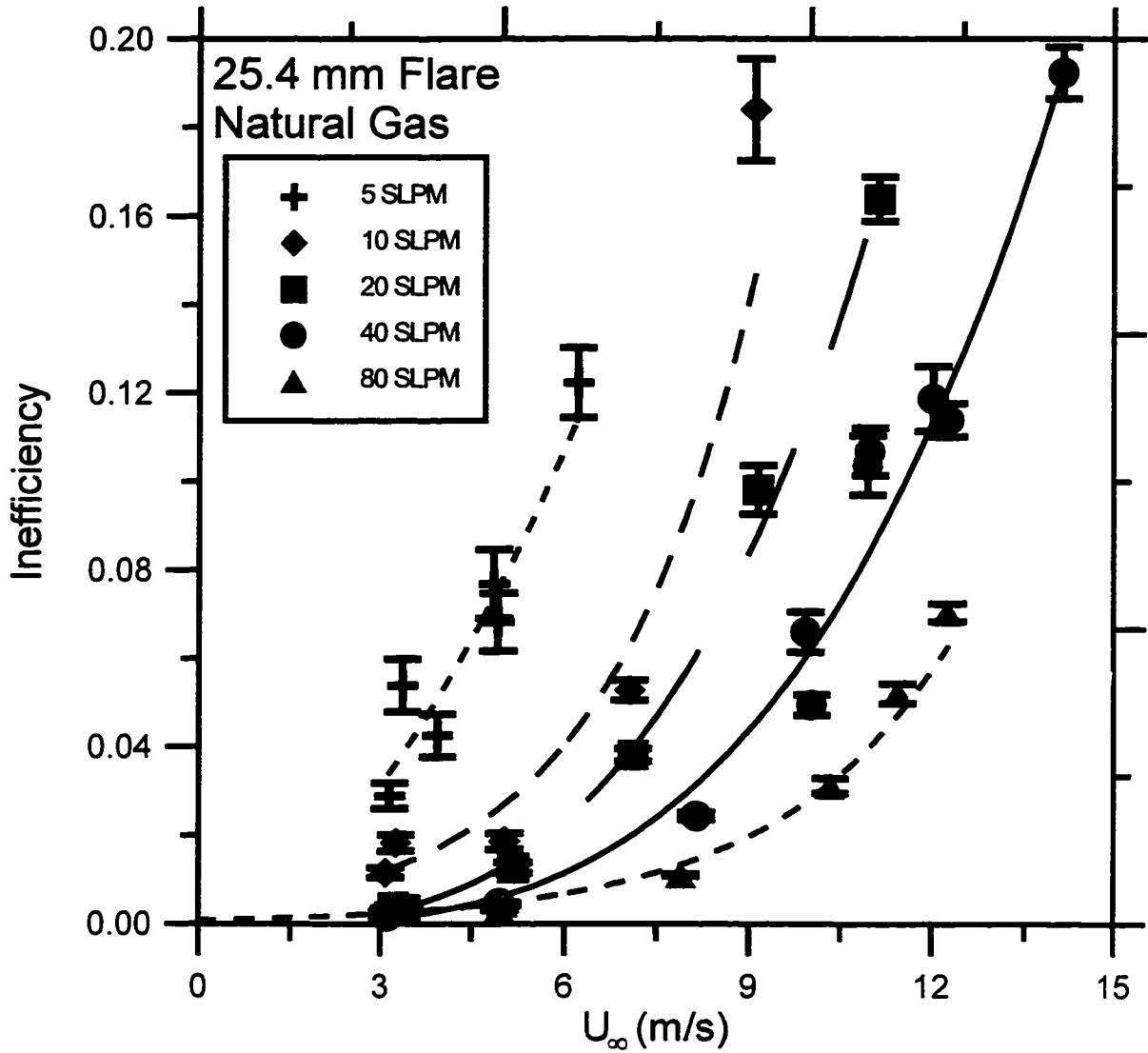


Figure 3.2 - Hydrocarbon destruction efficiency of 25.4 mm scale flare at varying fuel flow rates and wind speeds. The curves of constant flow rate show similar behavior. Inefficiency is low until some critical wind speed where the inefficiency increases dramatically. As fuel flow rate is increased, the onset of inefficiency is delayed.

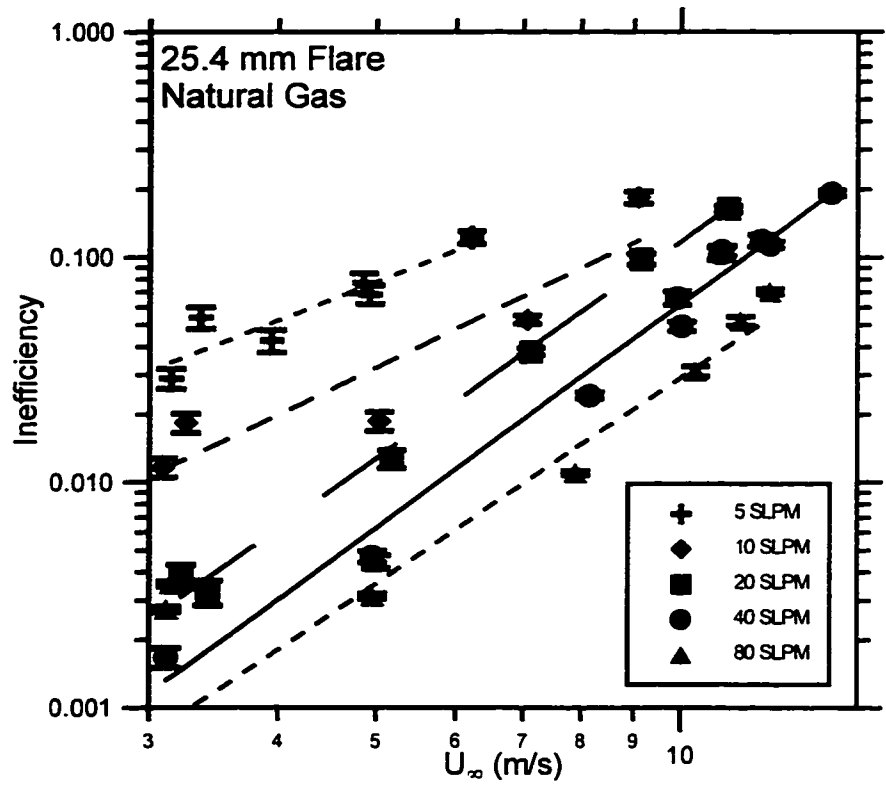


Figure 3.3 - Power Law behavior of 25.4 mm flare destruction efficiency for varying wind speed. Re-plotting Figure 3.2 on logarithmic scales changes the curves of constant fuel flow rate into straight lines, suggesting that flare inefficiency has a power-law behavior.

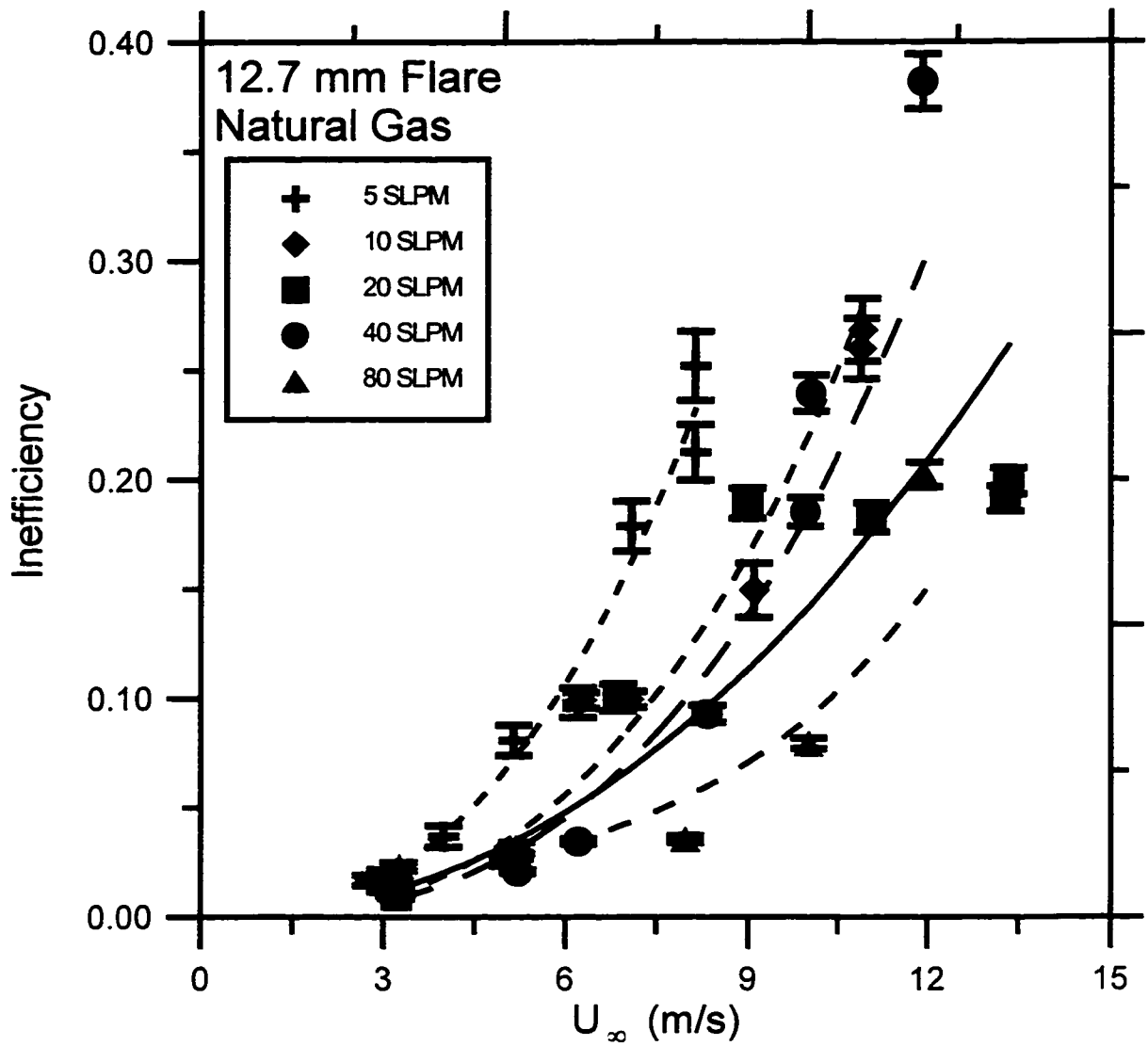


Figure 3.4 - Hydrocarbon destruction efficiency of 12.7 mm scale flare for varying fuel flow rate and wind speed. The 12.7 mm flare exhibits similar behavior to the 25.4 mm flare. Inefficiency is again low until some critical wind speed where inefficiency increases rapidly. The similarity of the behavior of the two flares suggests that this inefficiency behavior exists over a range of scales.

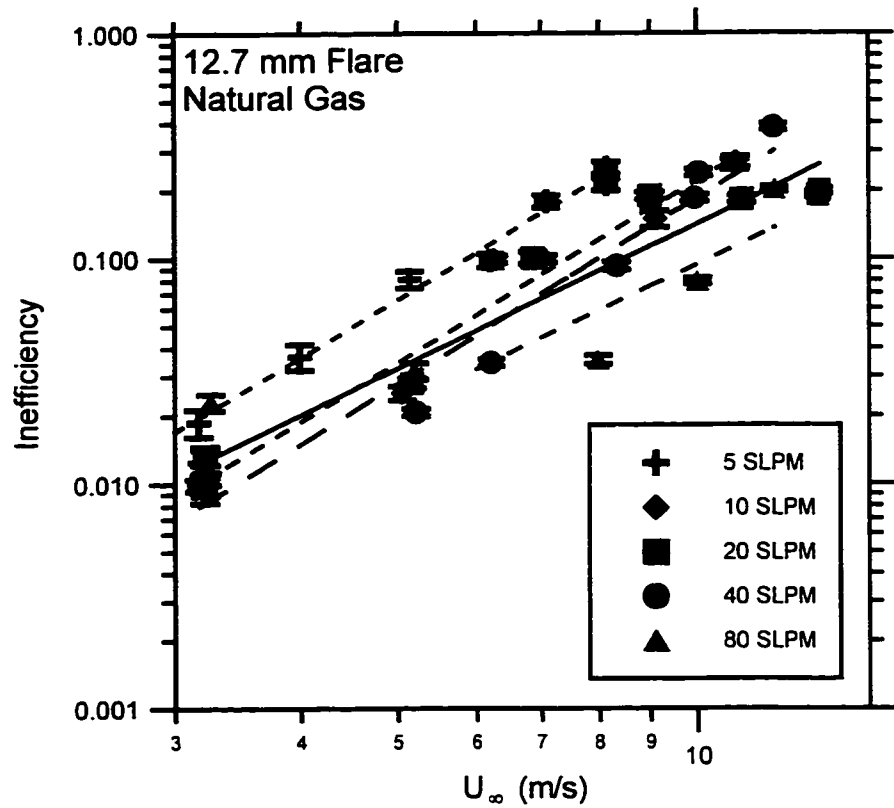


Figure 3.5 - Power law behavior of 12.7 mm flare inefficiency for varying wind speed.

Again, when plotted on logarithmic scales, the curves of constant fuel flow rate become straight lines, adding confidence to the notion of power law behavior for flare inefficiency.

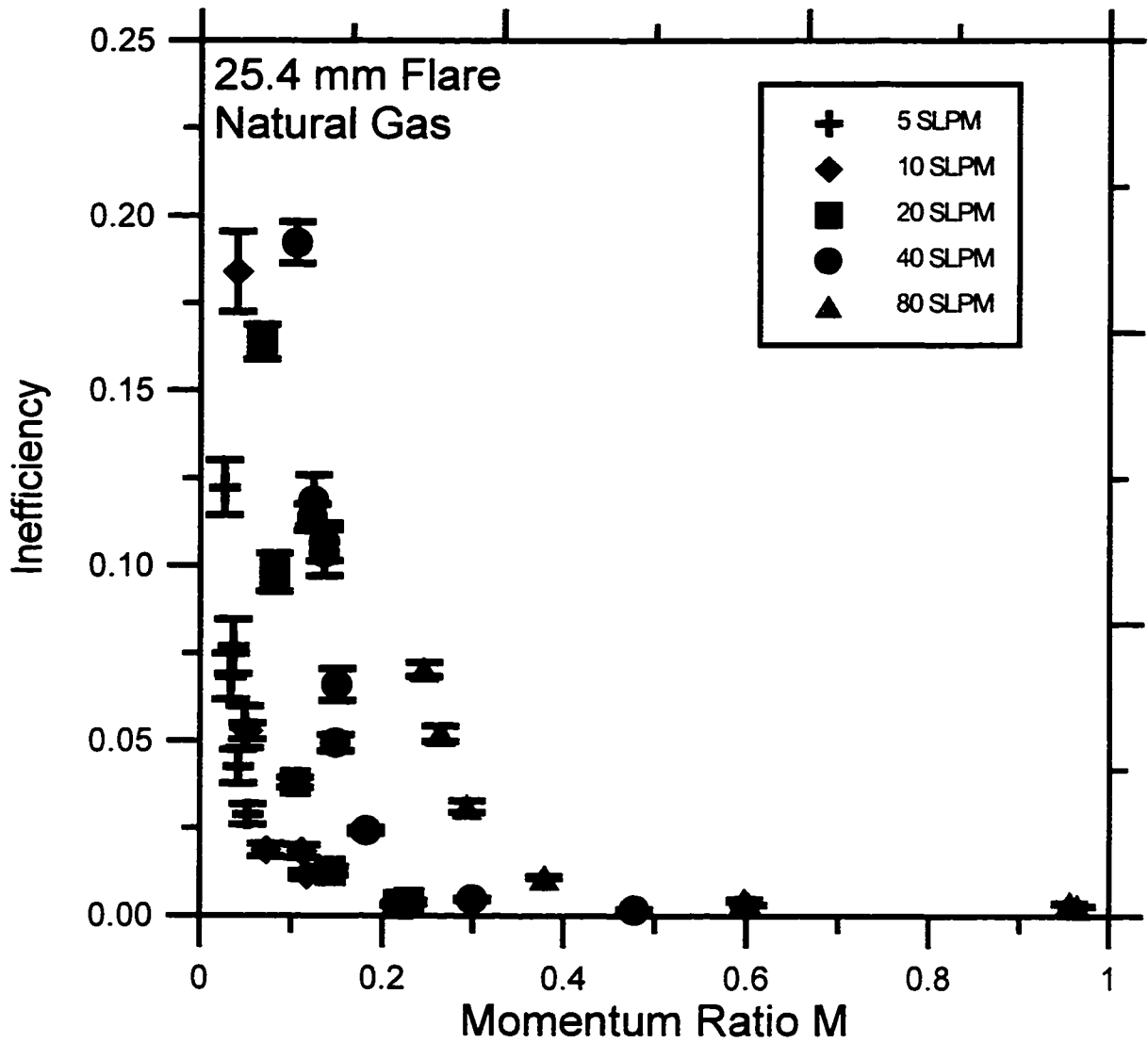


Figure 3.6 - 25.4 mm flare inefficiency plotted as a function of the ratio of air momentum to fuel momentum. Attempting to correlate flare behavior to the ratio of air and fuel momentum does not create any significant change in the spread of the data.

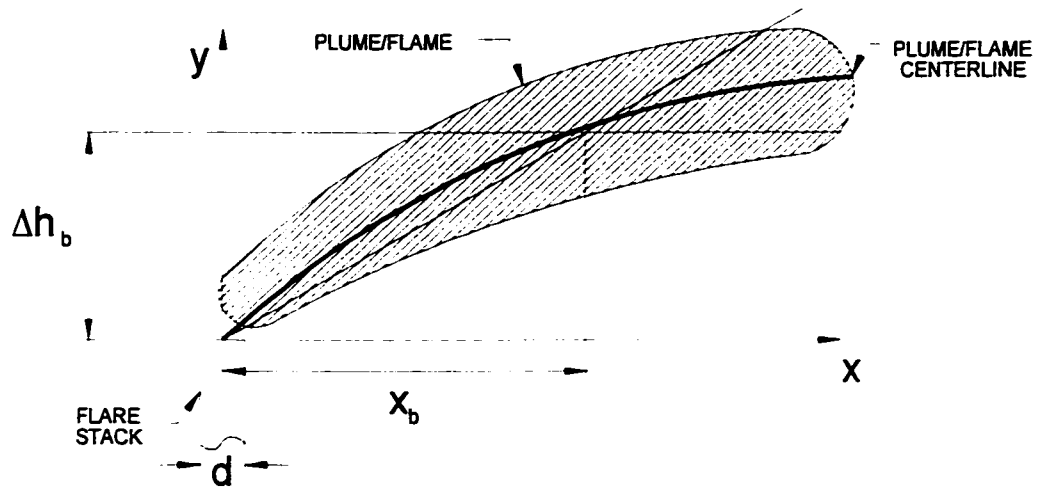


Figure 3.7 - Diagram illustrating plume nomenclature. The flare flame is a buoyant reacting plume, with the combustion process governed by the entrainment of air into the plume to be mixed and burned with fuel.

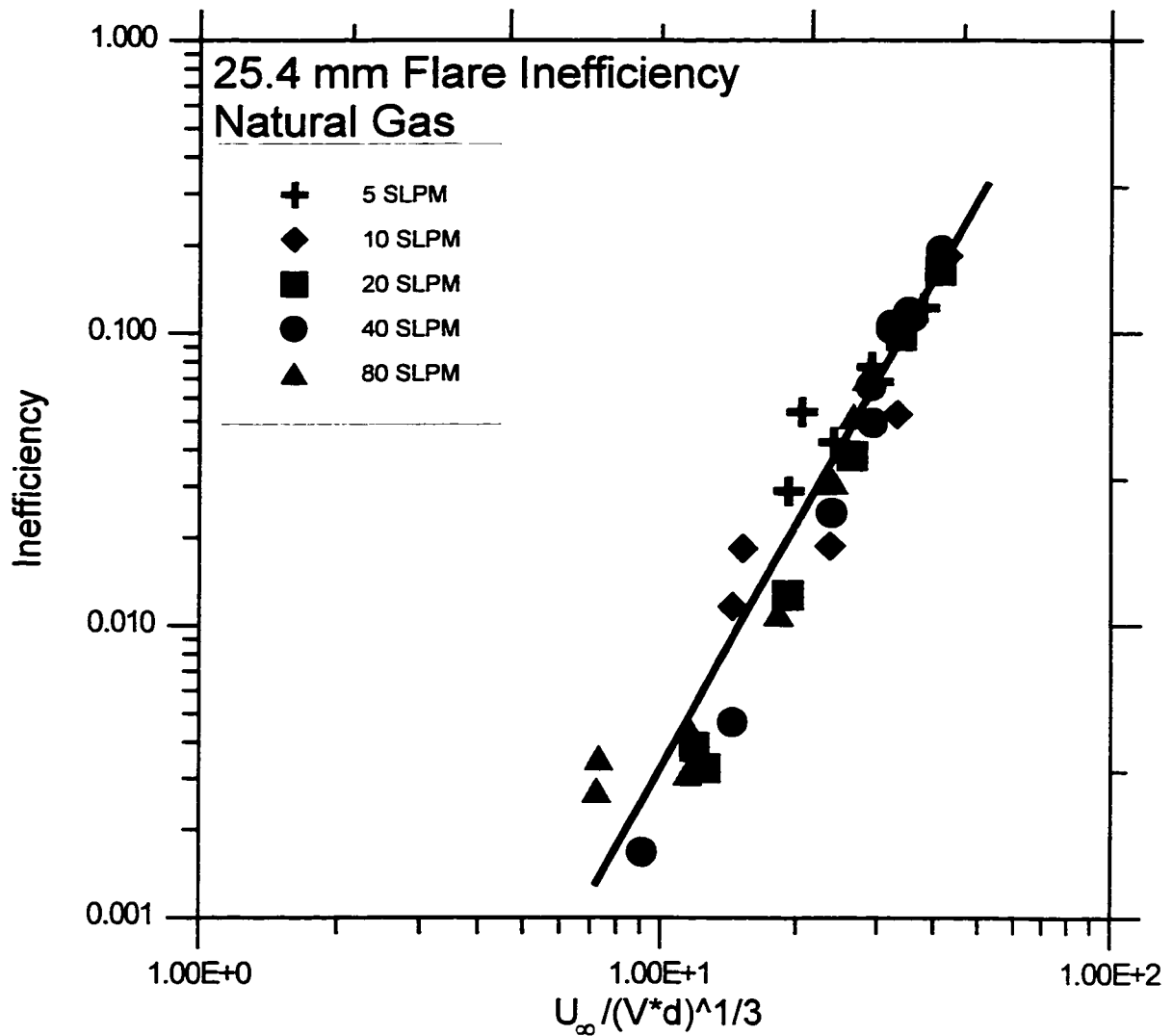


Figure 3.8 - 25.4 mm flare inefficiency data plotted as a function of $\frac{U_\infty}{V_r^{1/3} d^{1/3}}$ (Equation

3.6). The relation from Equation 3.6 collapses the inefficiency data onto a single line, appearing to confirm that maintaining a similar flame shape is the key to achieving similar flare behavior.

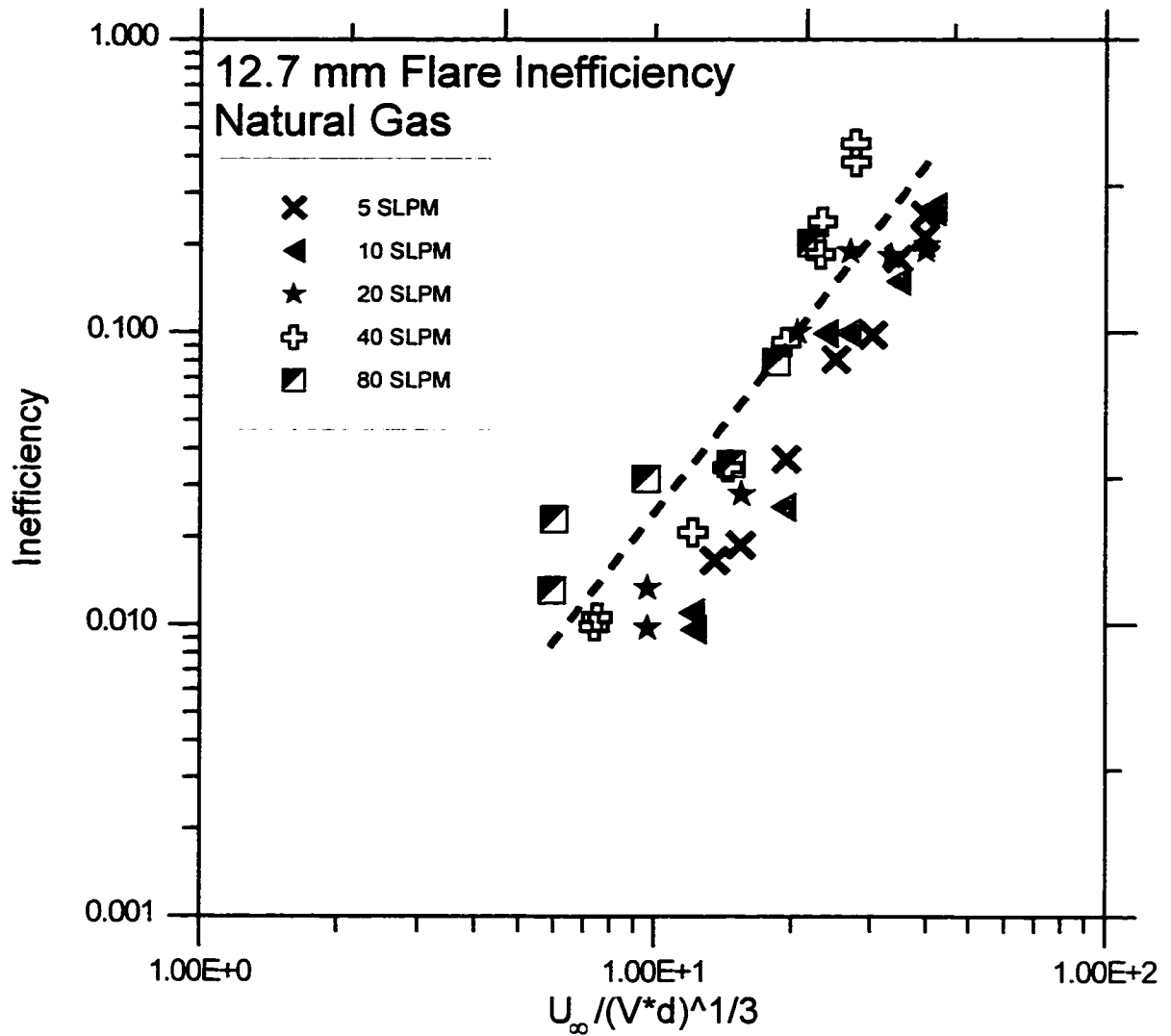


Figure 3.9 - 12.7 mm flare inefficiency plotted as a function of $\frac{U_{\infty}}{V_f^{1/3} d^{1/3}}$. The 12.7 mm

flare data does not converge as well as the 25.4 mm flare data. This may be due to the presence of a turbulence generator in the 25.4 mm flare that created a uniform gas flow profile across the range of flows tested and the lack of such a generator in the 12.7 mm flare, whose flow profile varied from laminar to turbulent as flow rate was increased.

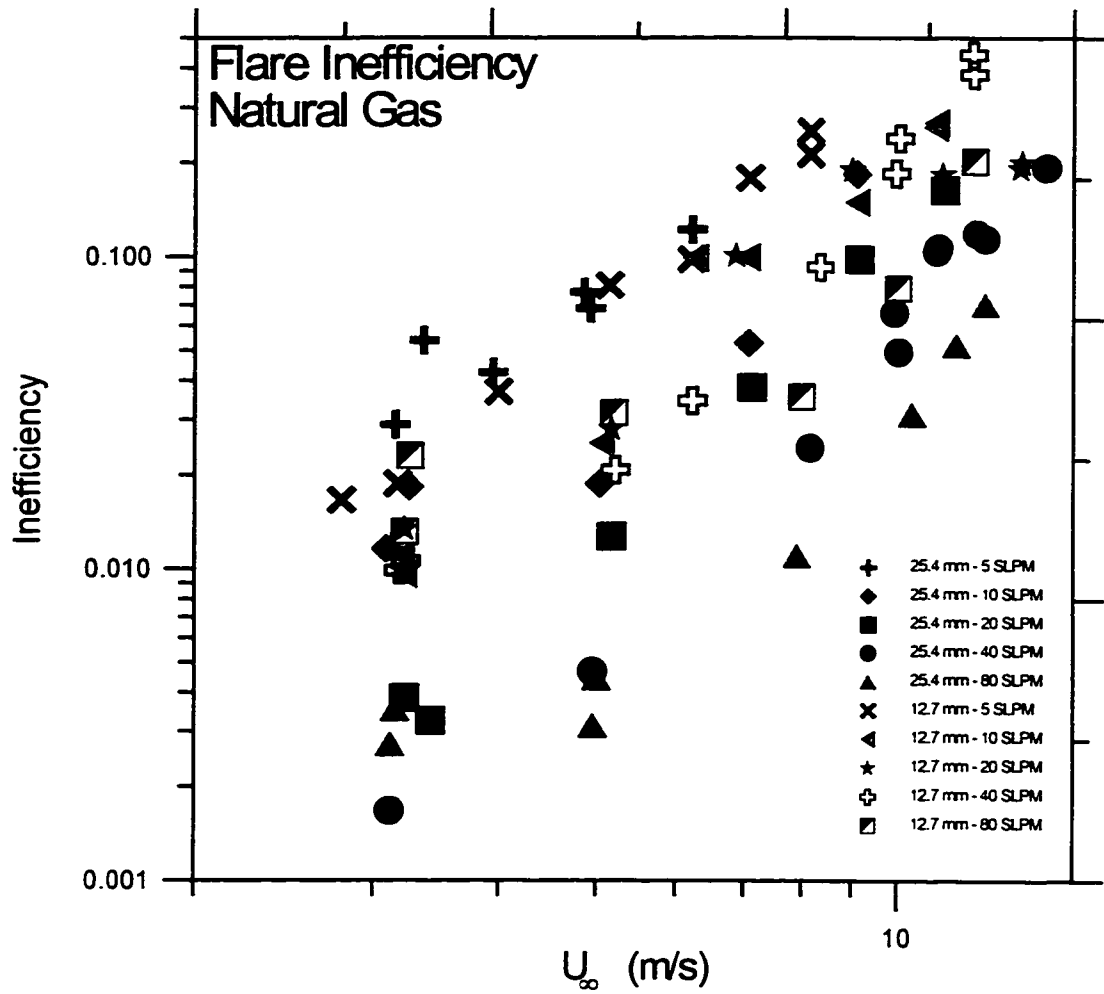


Figure 3.10 - Destruction inefficiencies of 12.7 mm and 25.4 mm flares plotted as a function of wind speed for varying fuel flow rates. Simply plotted against wind speed, no significant correlation is apparent for the inefficiency data from the two flares.

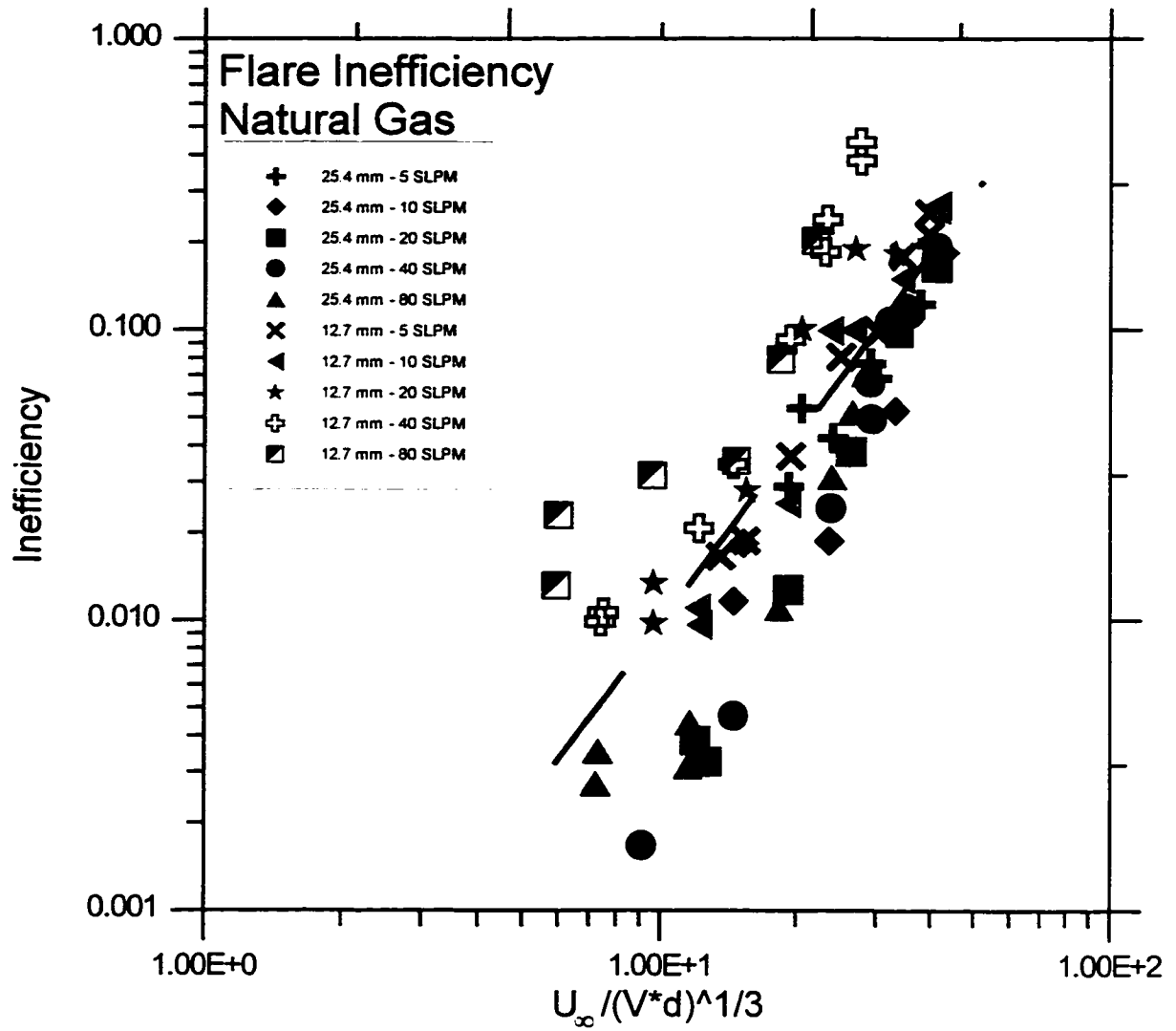


Figure 3.11 - Flare inefficiency data collapses onto a single line when plotted as a function of $\frac{U_{\infty}}{V_r^{1/3} d^{1/3}}$ (Equation 3.6). Despite some scatter in the data from the 12.7 mm flare, the inefficiency data shows a strong correlation when plotted against the relation derived from modeling the flare behavior as a buoyant plume.

Chapter 4 - Conclusions

This dissertation has quantified the substantial effects of wind on the efficiency of flares. The effect of wind on flare efficiency has been measured by developing a wind tunnel-based method of testing flare efficiency under well-controlled conditions. A predictive scaling relation has been developed that defines the interaction of flare efficiency, wind speed and flaring rate. The scaling relation can be used to extrapolate results obtained with small laboratory-scale flares to large industrial flares.

Measuring Efficiencies of Flares in Cross-Winds

Chapter 2 described an accurate, reliable method for measuring the efficiency of a flare or jet diffusion flame in a cross-wind. Flame efficiency measurement was based on a global balance of combustion products to avoid the uncertainties related to the plume sampling techniques used in many previous measurements of flare efficiency. Typical uncertainties in measured destruction inefficiency (I_d) was 5% (i.e. $I_d = 0.10 \pm 0.005$).

The measurements were conducted in a large enclosed facility that allowed well-controlled test conditions. Parameters which could be varied included fuel flow rate and composition, cross-flow speed, turbulence levels both in the cross-flow and the fuel flow, and burner geometry.

Although currently implemented in a large wind tunnel, this test method could conceivably be applied to any closed-loop structure for testing of flares. Development of this test method opens the possibility of a standardized test of efficiency that could be used by flare manufacturers for product evaluation.

Efficiency of Flares in Cross-Winds

Most studies conducted previously have assumed or concluded that flare efficiency is greater than 98% in all regimes. The test results presented in Chapter 3 showed that flare efficiency depends on wind speed. Flare efficiency was very high until some critical wind speed is attained after which efficiency drops off rapidly with roughly the cube of wind speed.

Relationship Between Efficiency, Wind Speed and Flaring Rate

By treating the flare as a combustion process governed by air entrainment of a buoyant plume, a relation was derived in Chapter 3 between flare efficiency, wind speed (U_∞), flare diameter (d) and fuel exit velocity (V_f). The functional form of these parameters has

$\left(\frac{U_\infty}{V_f^{1/3} d^{1/3}} \right)$ and allowed all of the destruction efficiency data collected to be correlated. It

can be used to translate the results obtained with small laboratory scale flare models to large industrial flares.

Future Directions

The testing presented in this dissertation covered only two sizes of small scale model flares with a simplified geometry burning a high quality fuel. While sufficient to add insight into the effect of wind on flare efficiency, the limited data collected may not effectively represent the wide variety of flare geometries and fuel compositions encountered in the real world. Initial follow-on work would include testing a wider range of sizes of scale flares to strengthen the validity of modeling a flare as a buoyant reacting plume.

The fidelity of the flare modeling could be improved by modifying several test parameters. The model geometries should be modified to more effectively represent the complex shapes of industrial flares. The various pilots and wind shields added to actual flares produce more complex fluid interactions near the flare tip than are present at the tip of a simple pipe flare. Fuel composition should be modified to establish what effect the lower quality fuels flared by industry will have on efficiency in a cross-wind. The fuel burned in this study was high-quality natural gas which could be expected to burn well. Flare gas is composed of a mixture of methane, carbon dioxide, hydrogen sulphide and droplets of heavier hydrocarbons, lowering the quality of the fuel supplied to the flame. Finally, the uniform, low turbulence flow profile in the wind tunnel test section should be modified to represent a turbulent atmospheric boundary layer. Observation has indicated that the turbulence generated by a bluff body upstream of the model flare in the wind

tunnel dramatically increases flare intermittency. This increase in intermittency may interfere with the flare combustion process and decrease flare efficiency.

Appendix A - Low Speed Wind Tunnel

The Low-Speed wind tunnel facility is located on the main floor of the Mechanical Engineering Building. It was built in the early 1970s' as a multi-purpose facility for environmental and aerodynamic research.

The wind tunnel facility was modified for use by the Flare Research Project which requires burning scale flares inside the tunnel. Modifications include installation of a heat shield, a combustible gas monitoring system, purge fans and extensive sealing.

Wind Tunnel Layout

The wind tunnel is a two-story structure located in the south-east corner of the Mechanical Engineering building (Room 1-31). The tunnel has two test sections: a 2.5 m x 2.5 m low speed test section and a 1.2 m x 2.4 m high speed test section. A diagram of the wind tunnel is shown in Figure C-1. Wind tunnel volume is approximately 350 m³.

The fan and motor are located on the second floor of the wind tunnel facility, blowing into the low-speed test section. The flow is directed through fiberglass matting at the end of the low-speed test section acting as a filter into a large plenum. The outlet of the plenum leads towards the lower section of the facility. The flow is turned into and out of the plenum by sets of vanes. At the bottom of the plenum, the flow passes through several sets of fine nylon screens and a contraction section to reduce turbulence intensity and produce a uniform flow into the high-speed test section. The high-speed test section

is 12 m long. Calculations and measurements show that it develops a 0.15 m boundary layer by its end [Wilson, 1979]. The flares are located 9.5 m from the leading edge of the high speed test section. After passing through the high-speed test section, the flow is turned with another set of vanes and gradually expands back to the fan.

Two pneumatically-controlled dampers are installed in the wind tunnel. A 1x4 m exhaust damper is located at the top of the large expansion on the east wall of the Mechanical Engineering Building. A 1x2 m intake damper is located on the side of the wind tunnel just before the fan intake. The intake damper opens to the south wall of the building. The dampers can be opened while the tunnel is running to permit operation in a pseudo-open circuit mode. Damper locations are shown in Figure A.1.

Modifications for Combustion Experiments

The wind tunnel is mainly constructed of plywood and plexiglass supported by a metal frame for structure. Due to the flammable nature of the construction, modifications were required for the safe combustion within the test sections and storage of combustible gases within the wind tunnel facility.

An aluminum heat shield was installed just below the ceiling of the high speed test section. The heat shield is suspended 3 cm below the ceiling of the section, and is intended to reduce the heating of the plywood ceiling by flare radiation or direct flame or plume impingement. A plenum and blower were installed at the end of the test section to suck air through the gap between the heat shield and ceiling to increase cooling.

Installation of a series of thermocouples on the tunnel roof has since revealed that the ceiling temperature does not exceed 40° C when a flare is burning even without the blower. Consequently, the blower has not been used to avoid complicating the flow profile within the test section.

Two purge fans were installed in the wind tunnel to assist in evacuating the tunnel of combustion products following a flare test or in the event of a build up of combustible gas. The combined flow rate of the two fans are 7 m³/s and returns the contents of the wind tunnel to essentially ambient air conditions in 10 minutes. The fans have been mounted to the wind tunnel intake damper.

A 4-head General Instruments Model 610 Combustible Gas Monitor was installed in the wind tunnel. The monitoring system reports combustible gas concentration as a percentage of the lower explosive limit of methane (5% concentration by volume) [General Monitors, 1995]. When the concentration of combustible gas reaches 30% of the lower explosive limit, a warning alarm is sounded. If the concentration reaches 60% of the lower explosive limit, the monitoring system sounds another alarm and activates the purge fans to evacuate the wind tunnel facility. Sensor heads are located in the ceiling above the wind tunnel facility, in the low-speed test section, above the high-speed test section, and on the floor below the high-speed test section. The upper sensors are for lighter gases (e.g. methane) that may collect at ceiling level. The lower sensors are for heavy gases (e.g. propane) that tend to collect at the floor.

Wind Tunnel Performance

The wind tunnel is powered by a 200 HP DC electric motor with a 6-bladed fan. The DC motor allows precise speed control and can maintain steady flow rates in the wind tunnel even at very low speeds. Wind speeds as high as 25 m/s can be reached in the high-speed test section. The excellent speed control of the tunnel motor allows for steady speeds as low as 0.20 m/s in the high-speed test section, ideal for environmental studies [Wilson, 1979].

The high speed test section has extremely low levels of turbulence and an extremely uniform flat flow profile. Free stream turbulence intensity in the high-speed test section is 0.1% and mean flow velocity varies $\pm 1\%$ [Wilson, 1979].

The low-speed test section is not used for flare testing. Due to its close proximity to the fan and the lack of flow straightening devices upstream, the flow in the low-speed test section is too turbulent to be of much use.

Tunnel Leak Rate

Wind tunnel leak rate is an important parameter in flare efficiency testing. The efficiency tests require a well-sealed volume so that the corrections applied for leaking gas are small. Initially the wind tunnel leak rate was measured using a tracer-decay technique and found to be unacceptably high. Subsequently, a large effort was made to improve the tightness of the wind tunnel. In the end the leak rate was reduced by 90% of its initial state.

Tracer-Decay Technique for Air Infiltration Measurements

The tracer-decay technique to measure the leak rate involves placing an amount of tracer gas into a closed volume and monitoring the decay in tracer concentration with time. The decay rate can be used to determine the air infiltration/leakage rate of the closed volume. When the ambient air contains no tracer gas, the concentration of the tracer gas in the wind tunnel can be written as

$$C(t) = C_o e^{-kt} \quad \text{A.1}$$

where

C = concentration of tracer

C_o = initial concentration of tracer

t = time

k = air changes per unit time

Sulfur hexafluoride (SF₆) was used as a tracer gas because its unique infrared adsorption spectrum enables detection of very low concentrations and it is not found naturally in the atmosphere [Costello et. al., 1982].

SF₆ concentration was measured with a Foxboro Miran 103 infrared gas analyzer equipped with a filter designed for SF₆ measurement. The analyzer was calibrated using a closed-loop calibration pump connected to the Miran. A known concentration of SF₆ was produced in the Miran by injecting SF₆ into the known volume of the calibration pump/analyzer system with a micro-syringe.

Air infiltration tests were conducted by setting the wind tunnel at a fixed speed, emptying a container of tracer gas in the wind tunnel, and tracking the decay in tracer concentration over a period of at least an hour. An exponential curve of the form given by Equation A.1 was fitted to the concentration data to determine the air infiltration rate. A sample trace of gas concentration during an air infiltration measurement is shown in Figure A.2.

Pressure upstream and downstream of the fan varies with wind speed, changing the air infiltration rate. Air infiltration rates were measured at a variety of speeds spanning the expected range of tunnel operating speeds. The air infiltration rate measured after improving tunnel sealing is plotted against high-speed test section wind speed in Figure A.3.

Tunnel Mixing Characteristics

The flare efficiency measurements operate under the assumption that the volume of the wind tunnel is well-mixed, with any gases added in any part of the wind tunnel quickly mixing with the rest of the volume. The actual assumption needed for the experimental methodology is that the sampling location shows the same rate of increase of temperature and concentration as the average wind tunnel condition.

Two types of mixing behavior are important: longitudinal mixing, or mixing of a substance along the length of the closed-circuit; and transverse mixing, or mixing of a substance through a cross-section of the tunnel. In both cases, the tunnel has good

mixing characteristics. Longitudinal mixing of an isolated pocket of gas is accomplished within 3-6 passes through the wind tunnel, and transverse mixing is complete within 1 pass. After these times no measurement inhomogeneities could be detected. The longitudinal mixing process is illustrated in Figure A.4.

The mixing characteristics were tested using SF₆ as a tracer gas and monitoring the mixing from several points within the tunnel. No significant concentration gradients were found to exist in the tunnel in any of these tests. Figure A.5 shows the concentration measured in four locations in the low-speed test section. The sampling position was changed every two minutes. Sampling positions were at the top, middle, bottom, and a corner of the test section.

Despite the positive conclusions of tunnel mixing tests, it was decided to attempt to further enhance mixing by installing 4 small fans in the low-speed test section. The fans are pointed in directions opposite to the swirl of the flow from the tunnel fan to increase turbulence levels in the low-speed test section and enhance mixing.

Tunnel Volume

Initial concepts for measuring flare efficiency required the volume of the wind tunnel to be known. Unfortunately, it has proven impossible to precisely determine the wind tunnel volume. The result of the volume measurements is that the wind tunnel volume may be quoted as $350 \pm 20 \text{ m}^3$.

The first attempts to measure tunnel volume were direct measurements of tunnel dimensions. Two separate attempts produced figures of 383 m³ and 342 m³. It became obvious that even small variations in measured dimensions can produce drastic changes in calculated volume for such a large structure.

Subsequent measurement attempts centered on adding a known amount of tracer gas to the wind tunnel and measuring the resulting concentration. This too encountered difficulty, this time due to the inability to accurately measure a volume of tracer gas and uncertainties in the gas analyzer calibration. These tests also raised the possibility that the participating volume of the wind tunnel may not be the same as the physical volume, and that indeed the participating volume may vary with wind speed inside the wind tunnel.

References

Costello, T.A.; Meador, N.F.; Shanklin, M.D.; "CO₂ Compared to SF₆ as an Air Infiltration Tracer", Paper No. 82-4014, American Society of Agricultural Engineers, 1982.

General Monitors, Model 610 Four Channel Combustible Gas Monitor Instruction Manual 09/89, Lake Forest, California, 1995.

Wilson, D.J.; Wind Tunnel Simulation of Plume Dispersion at Syncrude Mildred Lake Site, Environmental Research Monograph 1979-1, Syncrude Canada Ltd., 1979.

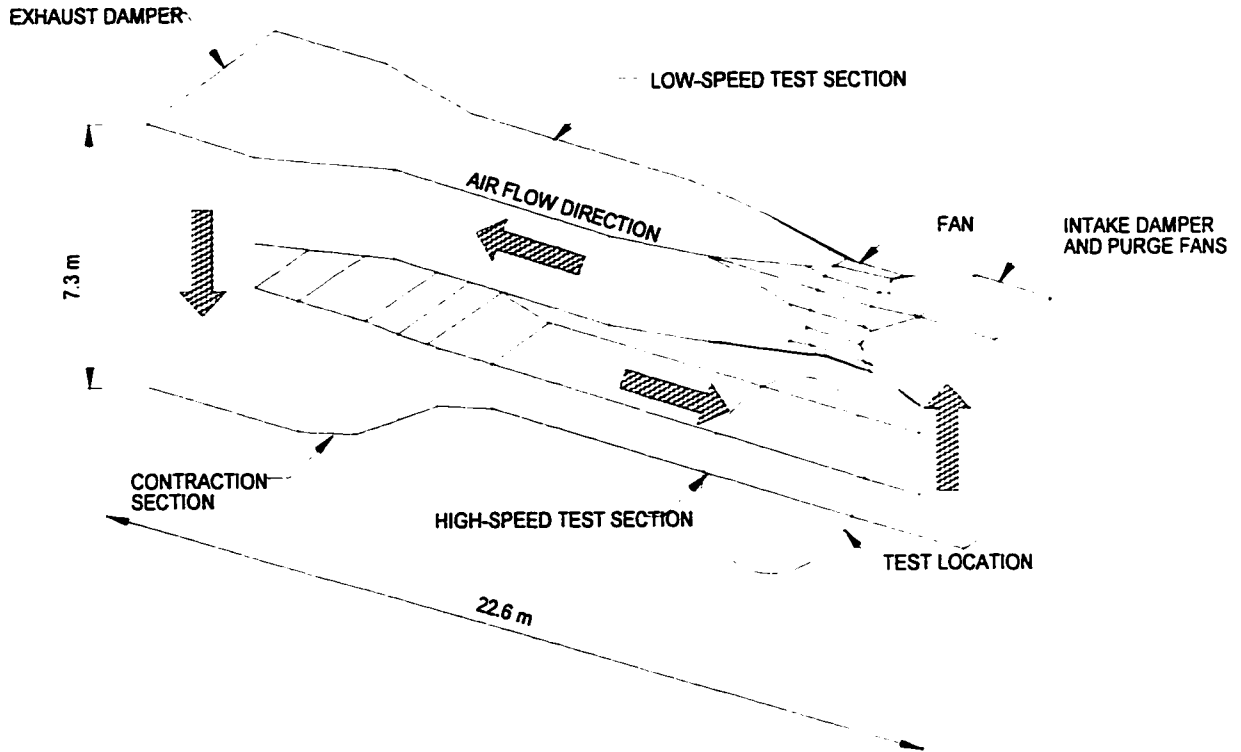


Figure A.1 - Diagram of Wind Tunnel Facility. The closed-loop wind tunnel facility is two stories high and is powered by a 200 HP DC electric motor. The facility has high speed and low speed test sections. Flare testing was conducted in the high speed test section, located in the lower half of the wind tunnel.

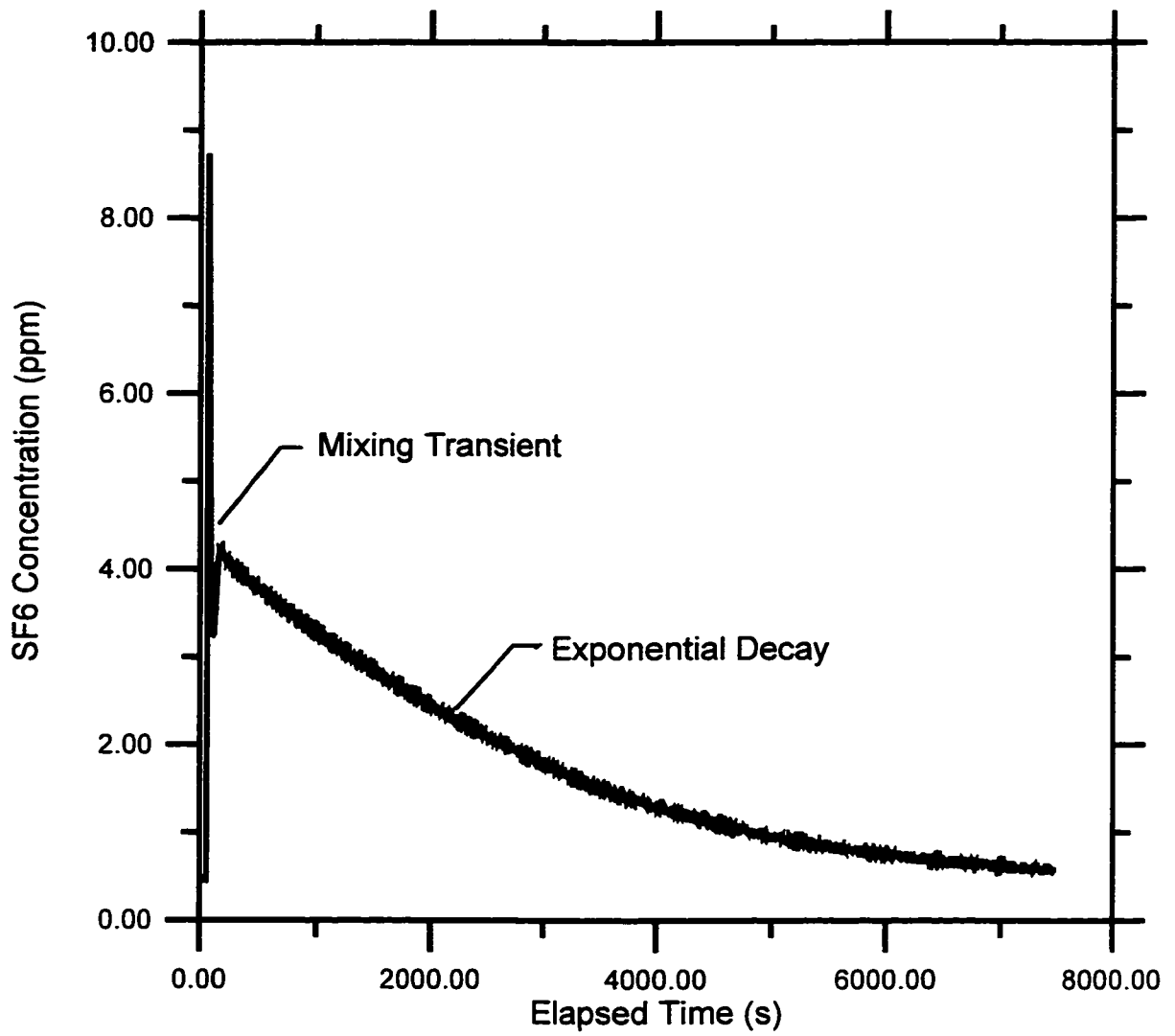


Figure A.2 - Typical decay of SF₆ tracer gas concentration measured in the high speed test section during an air infiltration test. The rate of exponential decay is used to determine air infiltration rate. Air speed is 5 m/s in the high-speed test section.

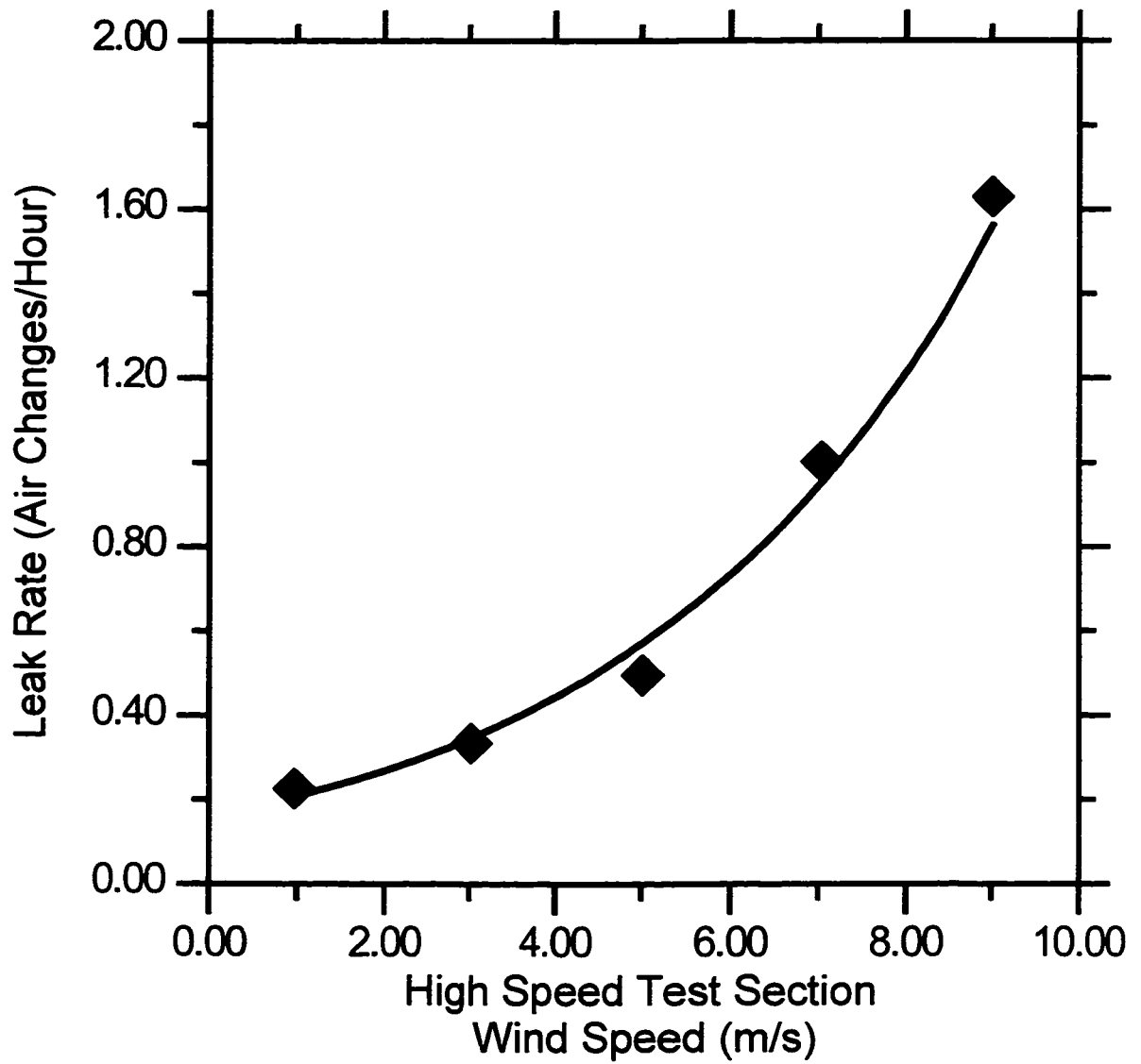


Figure A.3 - Wind Tunnel Leak Rate as a function of High Speed Test Section Wind Speed. Leak rate increases with tunnel speed due to the increased pressure differential between the test sections and ambient conditions.

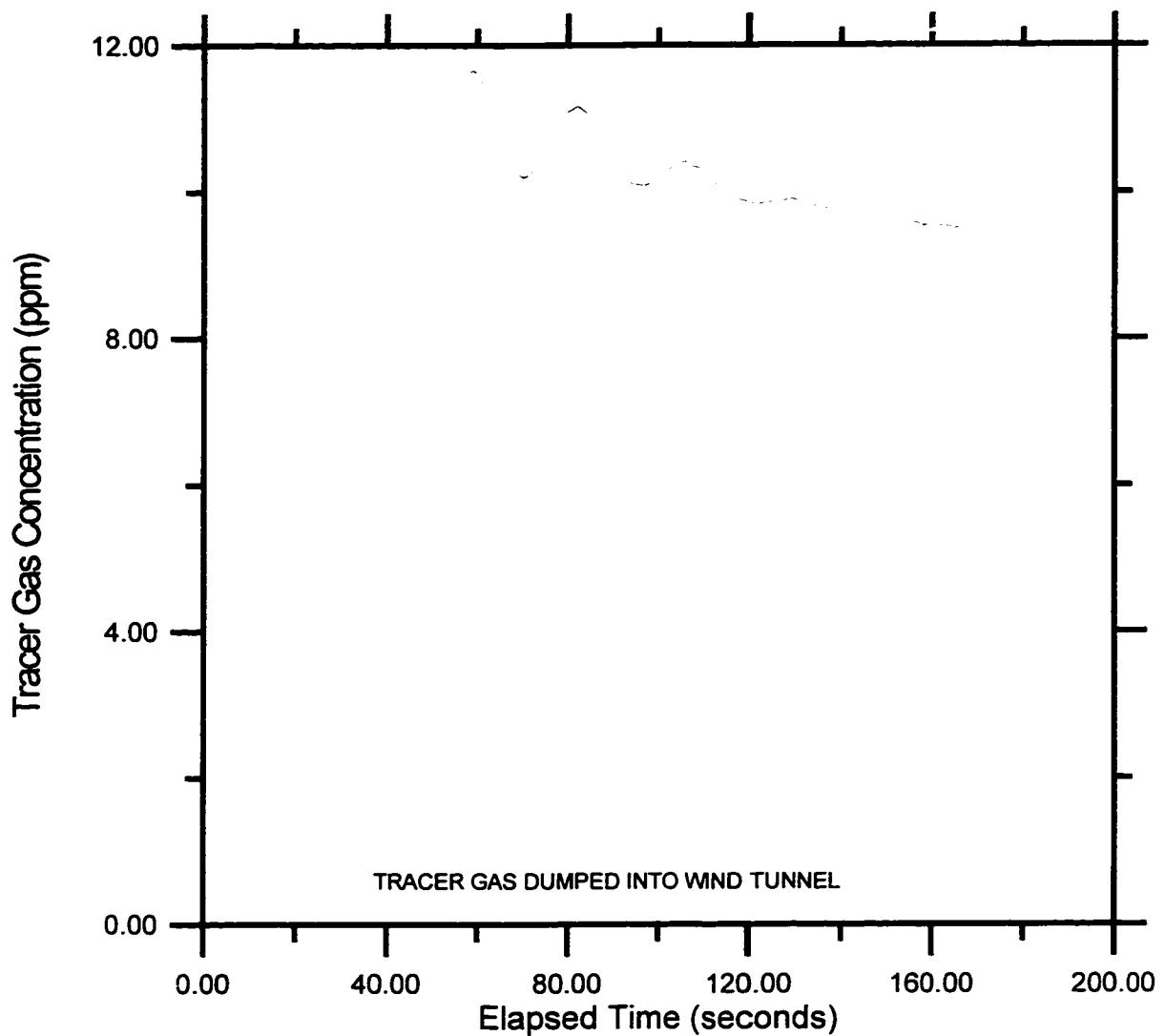


Figure A.4 - Longitudinal mixing behavior of the Low Speed Wind Tunnel.

Longitudinal mixing of the wind tunnel was examined by dumping a quantity of tracer gas (SF_6) at a point within the wind tunnel and watching the concentration of the gas at point in the wind tunnel as it was running. The plot above contains 4 humps. Each hump is caused as the pocket of gas dumped into the wind tunnel is circulated past the sampling point of the gas detector. After each pass, the length of the hump has increased and its height has decreased, indicating longitudinal mixing of the gas pocket. Longitudinal mixing is essentially complete after a gas pocket has made 3-6 circuits of the wind tunnel.

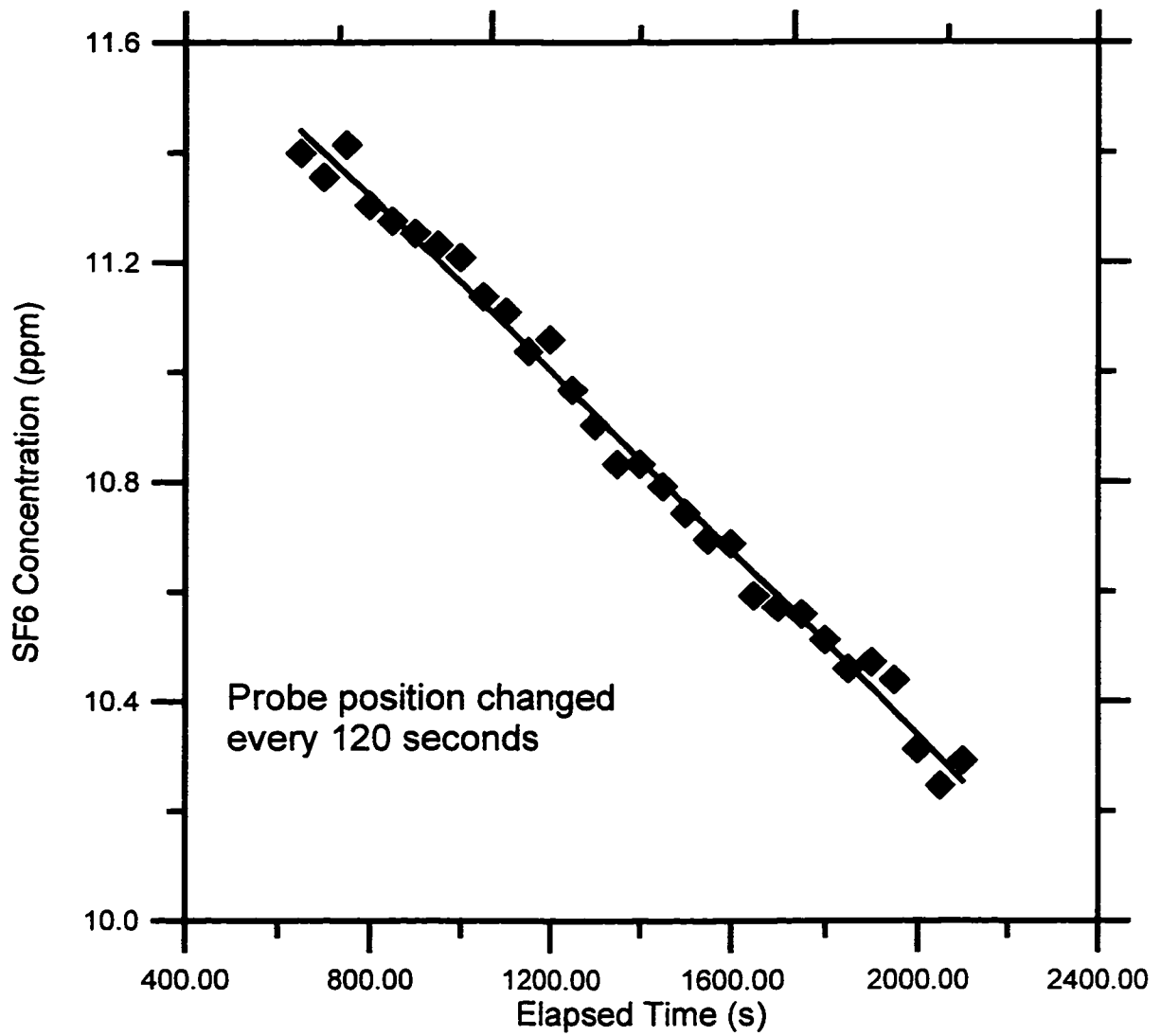


Figure A.5 - Variation in Tracer Gas Concentration Across Low-Speed Test Section. A probe was placed in the low speed test section and its position changed every 120 seconds as tracer gas was injected into the wind tunnel to establish how effective the tunnel mixing was. The absence of any concentration gradients within the resolution of the detector was interpreted as good mixing characteristics.

Appendix B - Gas Analysis System

Overview

A gas analysis unit was built to sample and analyze the combustion products of the flares burned in the wind tunnel. The system measured concentrations of nitrogen oxides (NO_x), carbon dioxide, carbon monoxide, oxygen, and hydrocarbons (HC). The system is self-contained, and output can be read from either a display screen on the unit or from an attached data acquisition system.

Components

The system is composed of 6 individual gas analyzers:

- ◆ NO_x
 - ◆ Horiba chemiluminescent unit
 - ◆ analyzes NO_x in ranges from 0-25 ppm to 0-500 ppm (NO equivalent)
- ◆ CO₂
 - ◆ Rosemount NGA 2000 Non-Dispersive Infrared
 - ◆ analyzes CO₂ in ranges from 0-2% to 0-15%
- ◆ CO
 - ◆ Rosemount NGA 2000 Non-Dispersive Infrared
 - ◆ analyzes CO in ranges from 0-200 ppm to 0-15000 ppm

- ◆ O₂
 - ◆ Rosemount NGA 2000 Paramagnetic Detector
 - ◆ analyzes O₂ in ranges from 0-5% to 0-25%
- ◆ Low Range Hydrocarbons
 - ◆ Rosemount NGA 2000 Flame Ionization Detector
 - ◆ Detects methane in ranges from 0-4 to 0-100 ppm
- ◆ High Range Hydrocarbons
 - ◆ Rosemount NGA 2000 Flame Ionization Detector
 - ◆ Detects methane in ranges from 0-250 to 0-2500 ppm

Principles of Operation

Non-Dispersive Infrared (NDIR)

Non-dispersive infrared detection makes use of the light absorption characteristics of a component of interest to determine the concentration of the component in a gas mixture.

The Rosemount NDIR system uses 2 parallel optical cells. One cell contains a reference gas and the sample gas flows through the other cell. Identical beams of infrared radiation are passed through the cells, interrupted by a chopper. Part of the infrared radiation is absorbed by the component of interest in the sample cell. The amount of absorption is determined by comparing the intensities of the beams emerging from the reference and

sample cells using the Luft principle. The amount of infrared radiation absorbed by the component of interest in the sample cell is proportional to the concentration of the component in the gas mixture.

The non-dispersive infrared system uses a laser as a light source, tuned to a frequency unique to the absorption spectrum of the component of interest. This reduces the possibility of another component interfering with the measurement.

Paramagnetic

Paramagnetic detectors make use of the ability of oxygen to become magnetic in the presence of a magnetic field. A small glass body is placed between 2 poles of a magnet in a stream of sample gas. The magnetic field acts on the oxygen contained in the sample. The oxygen then produces a force on the glass body. The amount of oxygen contained in the sample is measured by the restoring force needed to keep the glass body positioned between the poles of the magnet.

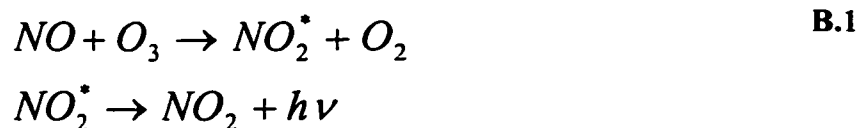
Flame Ionization Detection (FID)

Flame ionization detection is used to determine the concentration of hydrocarbons in a gas mixture. Sample gas is passed through a hydrogen-air flame, breaking the carbon-hydrogen bonds in the hydrocarbons and producing positively-charged carbon ions. The carbon ions are attracted to a negatively-charged electrode, creating an electrical current. The rate of carbon atoms entering the flame is proportional to the current in the detector electrodes. The concentration of carbon atoms can be used to determine hydrocarbon

concentration in the sample. The FIDs used in this study were calibrated to report the methane-equivalent of the hydrocarbon concentration.

Chemiluminescent

Chemiluminescence is a technique used to determine the concentration of nitric oxide in a gas mixture. The detector reacts the NO in a sample with ozone, which produces oxygen and nitrogen dioxide in an excited state. The nitrogen dioxide returns to the ground state by emitting a photon. The reaction process is given by:



[Ferguson, 1986]

By measuring the amount of light emitted by the reaction between the sample and ozone, it is possible to determine the concentration of NO in the mixture.

Gas Analysis System

The gas analyzers are mounted to a cart containing sample delivery equipment. A schematic of the gas analysis system is contained in Figure B.1. The sample is drawn from a single point in the wind tunnel and passed through a filter and a dryer unit. The dryer works by passing co-flowing streams of sample gas and dry air on opposite sides of a neoprene derivative which absorbs water vapor from the sample stream and transfers it to the dry air. A rotameter and valve are used to regulate the sample flow rate. A 3-way

valve is used to switch the gas stream between the sample port and the calibration gas port. The sample is split into 3 separate streams, feeding the hydrocarbon detectors, the NO_x detector, and the CO, CO₂, and O₂ detectors. Each stream is equipped with its own sample pump and rotameters for each analyzer module. The sample pumps are Barnant Model 400-1901 Vacuum Pressure Pumps, lined with teflon to minimize contamination of the sample streams.

The NGA 2000 gas analyzers are connected in a digital network controlled by a separate display unit. The display unit contains a small LCD screen, control keys and 5 analog output boards. The output boards convert the digital output of the analyzer modules into voltages to be read by the data acquisition system. (A digital output board exists that can be used to communicate digitally with an external computer, but was not available at the time of the initial testing.)

Calibration Procedures

Calibration is performed by zeroing and spanning the analyzers with reference gases. Purified nitrogen was used for zeroing the analyzers. The span gas varied from analyzer to analyzer. The span gases used are listed in Table B.1.

Table B-1 - Span Gases used for analyzer calibration

Analyzer	Span Gas
CO ₂ NDIR - Range 0-2%	1.91% CO ₂
CO NDIR - Range 0-200 ppm	178 ppm CO
O ₂ Paramagnetic - Range 0-25%	23.9 % O ₂
Low Range FID - Range 0-100 ppm	102 ppm CH ₄
High Range FID - Range 0-250 ppm	253 ppm CH ₄
NO Chemiluminescent - Range 0-25 ppm	25 ppm NO

The analyzer system was calibrated once a day. The gas analyzers drift before they are fully warmed-up, so the analyzer system was allowed to warm up for at least an hour before calibration.

The analyzers were first zeroed with pre-purified nitrogen. The nitrogen was allowed to flow through the analyzers for 3-5 minutes and the analyzer modules were individually zeroed using the zero controls of the Horiba NO_x analyzer and the Rosemount display unit.

After zeroing, the analyzers were spanned. The appropriate span gas from Table B-1 was passed through the analyzer until a steady reading is produced, then the analyzer is spanned using the span controls of the Horiba NO_x analyzer and the Rosemount display unit.

Analog Output Board Calibration

The analog output boards in the Rosemount display unit can be set for either 0-5 VDC or 0-20 mA and must be calibrated before they deliver the proper output. 0-5 VDC output was used. The output boards only need to be calibrated once, and the correct output levels are stored in an E-PROM chip on each board.

The output was calibrated by adjusting zero and span constants found in the Rosemount Technical Configuration Menu. The analyzers were calibrated prior to calibrating the analog output boards. With zero gas flowing through the analyzer system, the output board zero constants were adjusted so that the data acquisition system read a small (1-5 mV) positive offset voltage from the output boards. With span gas flowing through each analyzer, the span constants were set. The span constant was adjusted to set the full-scale output of each output board to 5 V as read by the data acquisition system. The data acquisition system was used to read the voltage output of the analog output boards to account for any signal degradation over the signal wire and connections.

References

Ferguson, C.R.; Exhaust Gas Analysis, in Internal Combustion Engines, John Wiley & Sons, pp. 198-206, 1986.

Instruction Manual for CLA-510SS General Purpose Gas Analyzer Unit, Horiba Instruments Incorporated, August 1994.

NGA 2000 Flame Ionization Detection Analyzer Module, Software Version 2.2, Instruction Manual 748331 Rev. B, Rosemount Analytical Inc., February 1996.

NGA 2000 I/O Modules, Instruction Manual 748275 Rev. C, Rosemount Analytical Inc., September 1994.

NGA 2000 Non-Dispersive Infrared Analyzer Module, Software Version 2.2, Instruction Manual 748332 Rev. D, Rosemount Analytical Inc., June 1997.

NGA 2000 Paramagnetic Detector Analyzer Module, Software Version 2.2, Instruction Manual 748330 Rev. A, Rosemount Analytical Inc., April 1995.

NGA 2000 Platform Components, Software Version 2.2, Instruction Manual 748329 Rev. A, Rosemount Analytical Inc., April 1995.

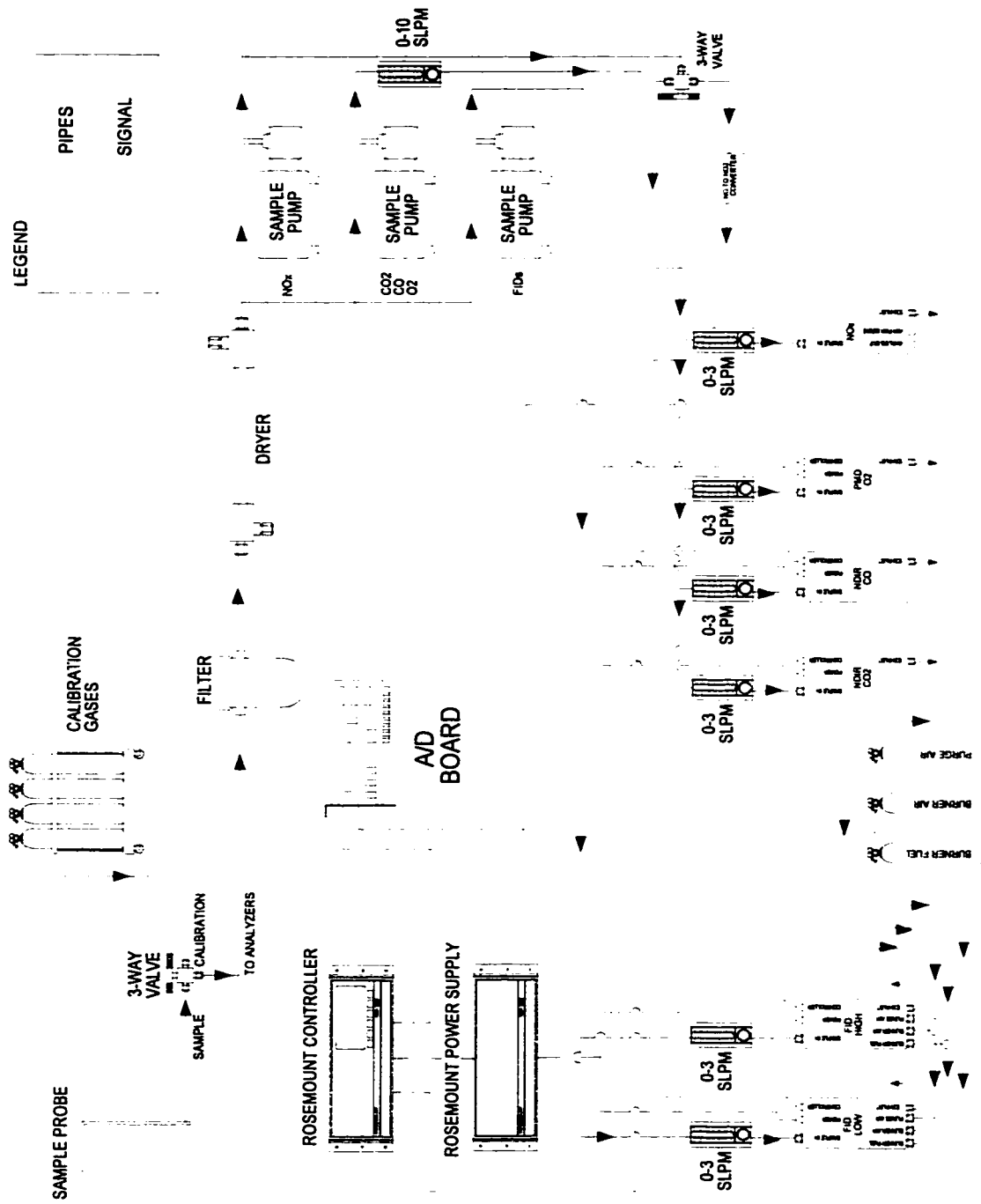


Figure B.1 - Schematic of Gas Analysis System. Solid lines indicate gas piping. Dashed lines indicate electrical and signal connections.

Appendix C - Experimental Diagnostics

The flare testing procedure described in Chapter 2 requires precise measurement of fuel flow, and accurate measurements of wind tunnel air speed and air temperature. Mass flow meters were employed to obtain accurate, precise control and measurement of fuel flows. Wind tunnel air speed was measured using pitot tubes equipped with inductive pressure transducers. Wind tunnel air temperature was measured using a constant-current temperature transducer. A schematic of the diagnostics installation is shown in Figure C.1.

This appendix describes the principles of operation of the flow and temperature transducers used as diagnostics for flare efficiency tests, their installation in the wind tunnel and the procedures used to calibrate them.

Air Speed Transducers

Pitot tubes were used to measure air speed in the wind tunnel. Pitot tubes operate under Bernoulli's principle, measuring the difference between static and stagnation pressure at a point in a flow. The pressure difference can be used to calculate local flow velocity by

$$U_{flow} = \sqrt{\frac{2\Delta p}{\rho_{flow}}} \quad \text{C.1}$$

where

U_{flow} = local flow velocity (m/s)

Δp = stagnation pressure - static pressure (Pa)

ρ_{flow} = density of flow (kg/m³)

The high speed test section of the wind tunnel has an extremely uniform velocity profile ($\pm 1\%$ mean velocity), so a point measurement of flow velocity is a good measure of the average flow velocity [Wilson, 1979]. For example, if the pitot tube measured a local flow velocity of 5 m/s, the velocity at any point within the tunnel cross-section would not be expected to vary more than 0.10 m/s from the velocity measured by the pitot tube.

Two pitot tubes were placed in the wind tunnel. The first pitot tube was placed 2 m from the leading edge of the high-speed test section, extending 0.75 m into the flow. A second pitot tube was placed immediately adjacent to the flare in the high speed test section to account for any change in flow velocity caused by boundary layer growth and the heat shield located above the flare (see Appendix C for details). During testing, the flare pitot tube was used for airspeed measurement because of its closer proximity to the flare.

Each pitot tube was equipped with two pressure transducers. One pressure transducer was calibrated for a low range of pressures for high-resolution low speed readings. The other pressure transducer was calibrated for a higher pressure range to cover a higher range of flow speeds. The ranges and resolutions of each pitot tube are given in Table C-1.

Table C-1 - Pitot Tube Ranges & Resolutions

Pitot Tube	Range (m/s)	Resolution (m/s)
Forward Pitot Tube		
Low Speed Transducer Validyne DP103-10	10.6	0.5
High Speed Transducer Validyne DP15-20	36.6	1.8
Flare Pitot Tube		
Low Speed Transducer Setra Model 264	6.7	0.3
High Speed Transducer Validyne DP45	21.1	1.0

The forward pitot tube was attached to a Validyne DP103-10 pressure transducer calibrated for 0 - 6.5 mm water column and a Validyne DP15-20 pressure transducer calibrated for 0 - 75 mm water column. This gave the forward pitot tube a low speed range of 1 - 10 m/s and a high speed range of 1 - 35 m/s.

The flare pitot tube was attached to a Setra Model 264 pressure transducer calibrated for 0 - 2.54 mm water column and a Validyne DP45 pressure transducer calibrated for 0 - 25.4 mm water column. This gave the flare pitot tube a low speed range of 1 - 6 m/s and a high speed range of 1 - 18 m/s.

The air density used to calculate wind tunnel air speed was calculated using the ideal gas law. Ambient pressure was obtained from a mercury barometer. The pressure reading was taken once a day, with the assumption that any change in pressure throughout the day would be negligible. The tunnel air temperature was continuously measured using a temperature sensor in the wind tunnel.

Pressure Transducer Calibration

All pressure transducers were calibrated using a water column calibrator and micro-manometer. A schematic of the calibration set-up is shown in Figure C.2. The water-column calibrator is used to generate a pressure on the micro-manometer and the pressure transducer being calibrated. The micro-manometer is used to measure the generated pressure. The pressure transducer is calibrated by setting a zero point at atmospheric pressure on both positive and negative ports, and is then spanned by applying the desired maximum pressure to the positive port with the water column calibrator and setting the transducer span to full-scale output. The pressure transducers used all produced a linear output between 0 and 10 V.

Temperature Transducer

An AD590 constant-current temperature transducer was used to measure ambient air temperature in the wind tunnel high-speed test section. The temperature transducer was located 2 m from the leading edge of the test section, extending 0.6 m into the flow. A

radiation shield was placed immediately behind the transducer to prevent the flare radiation from affecting the temperature measurement.

The AD590 transducer produces a voltage output between -5 and 5 V. The transducer was spanned for a range of -50° C to 50° C. Its accuracy was $\pm 0.5^\circ$ C. The data acquisition system read the output with a resolution of 0.25° C.

Temperature Transducer Calibration

The temperature transducer was calibrated against a type T thermocouple in a water bath. The water bath was equipped with a heater, chiller and a stirring device to produce water circulation within the bath. A schematic of the calibration set-up is shown in Figure C.3.

The transducer and the thermocouple were placed in a thin waterproof latex sheath and immersed in the water bath. The transducer zero point was set by chilling the bath to 1° C. The transducer was spanned by heating the bath to 50° C and adjusting the output voltage to its positive full scale. After spanning, the zero was adjusted again to improve accuracy.

Mass Flow Meters & Controllers

Mass flow meters were employed to measure gas flow rates for flare efficiency tests.

Five of the flow meters were equipped with microprocessor-controlled valves that could accurately throttle the flow to a specified rate.

Mass flow meters measure flow rate using the specific heat of the measured fluid. The temperature of the flow at the meter inlet is measured. The flow then passes through a laminar flow device and is heated in a capillary by a small heating element. The temperature of the flow is measured again at the outlet. Knowing the specific heat of the fluid, the rise in temperature for a given heat input allow the flow rate through the flow meter to be determined [Omega, 1997]. The flow measurement is made on a mass basis, and as such is unaffected by changes in flow density or temperature (provided that the specific heat is not strongly dependent on temperature).

The models, ranges, accuracy and resolution of the flow meters used are listed in Table C-2.

Table C-2 - Mass Flow Meters used - Range, Accuracy & Resolution

Model	Range (SLPM)*	Accuracy (\pm SLPM)	Resolution (SLPM)
Matheson 8173-0434	24.4	0.24	0.03
Omega FMA-776-V	500	10	0.61
Omega FMA-774-V	100	2	0.12
Omega FMA-769-V	5	0.1	0.006
Omega FMA-767-V	1	0.2	0.001
Omega FMA-765-V	0.2	0.004	0.0002

**All data stated in terms of methane*

Calibration Procedure

The mass flow meters were calibrated by a mass displacement method using natural gas.

A tank of natural gas was placed on a Pacific Industrial Scale Model 550 electronic scale with a resolution of 5 g. As gas flowed through the mass flow meters, the mass flow rate of fuel was measured by the rate of change of the tank weight. The control valves on the mass flow meters were used to set the flow rate through the meters. Each meter was calibrated using 5 points spread over the meter range. Each point was determined by averaging the voltage output of the flow meter as 750 g of fuel flowed through the meter.

A schematic of the calibration set-up is shown in Figure C.4. A typical plot of tank weight and flow meter output is shown in Figure C.5. A line was fitted to each plot of mass flow rate vs. flow meter output voltage. Figure C.6 through Figure C.8 are plots of the flow meter calibrations.

The Omega 0.2, 1 and 5 slpm mass flow controllers were not calibrated with natural gas. The factory calibrations for methane were used. The low flow rates needed to calibrate these small flow meters made the use of a scale with a 5 g resolution impractical, as the time needed to acquire an accurate measure of the mass flow gravimetrically would have stretched into days or weeks per point. The natural gas used was ~94% methane [Johnson, 1995].

References

FMA760/770 Series & FMA860/870 Series Mass Flow Controllers & Meters User's Guide, Omega Engineering Inc., 1997.

Johnson, M.R.; Development of a Low Emissions, Lean Premixed, Natural Gas Burner, M.Sc. Thesis, University of Alberta, 1995.

Reference Manual for Model 550 Weigh Indicator, Manual T-26216-A, Pacific Industrial Scale Co. Ltd., 1991.

Wilson, D.J.; Wind Tunnel Simulation of Plume Dispersion at Syncrude Mildred Lake Site, Environmental Research Monograph 1979-1, Syncrude Canada Ltd., 1979.

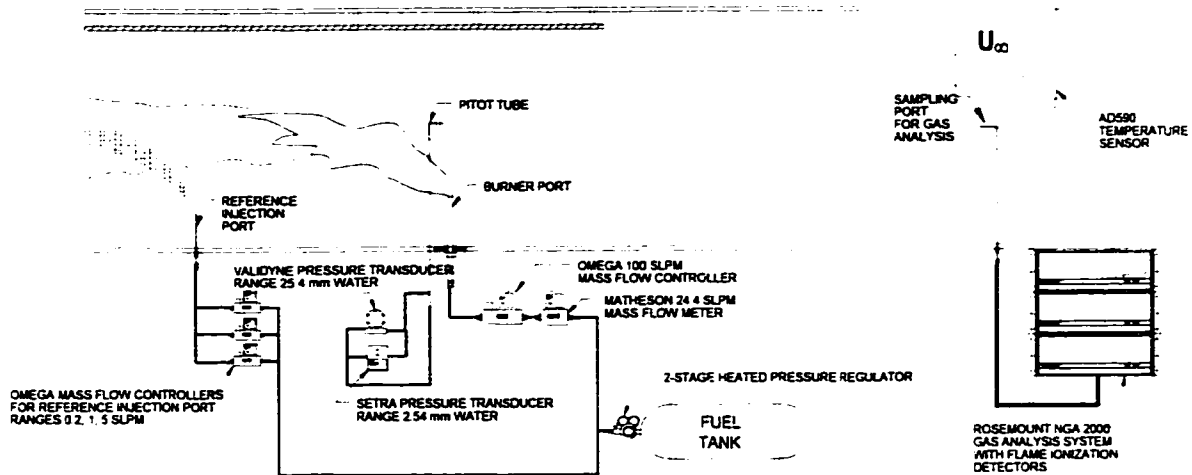


Figure C.1 - Diagram of Diagnostics Installation in Wind Tunnel. The flame inefficiency measurement requires the measurement of fuel and reference gas flow rates, hydrocarbon concentration in the wind tunnel, and the air speed and temperature inside of the wind tunnel. Fuel and reference gas flow rates are measured using mass flow controllers. Hydrocarbon concentration is measured using flame ionization detectors sampling from a port 3 m upstream of the flame. Air speed in the wind tunnel is measured with a pitot tube adjacent to the burner. Air temperature is measured with a constant-current temperature transducer located 3 m from the leading edge of the test section.

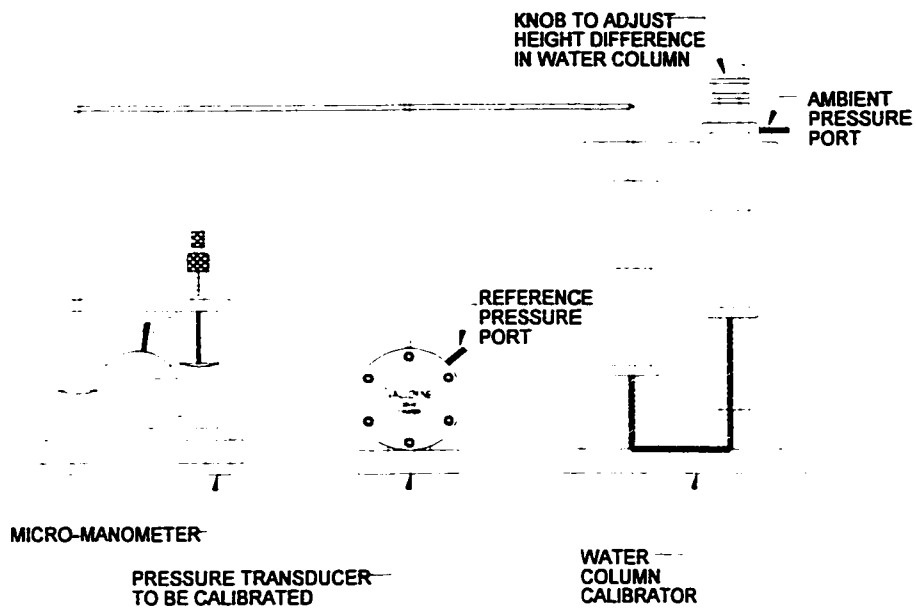


Figure C.2 - Schematic of pressure transducer calibration procedure. Water column calibrator is used to produce pressure. Pressure is measured using micro-manometer. Pressure transducer is connected in parallel with manometer for calibration.

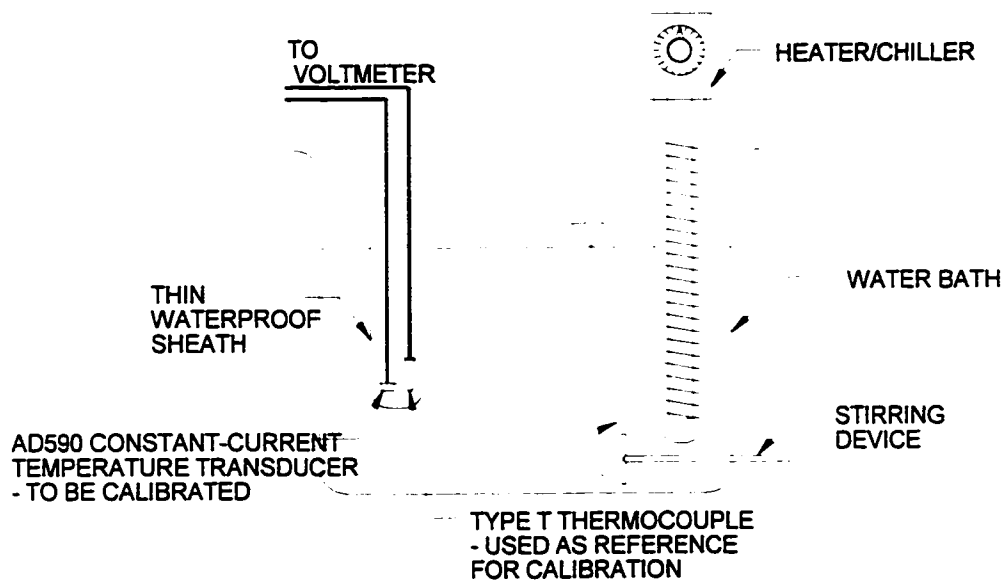


Figure C.3 - Schematic of temperature transducer calibration set-up. The temperature transducer was placed in a thin waterproof latex sheath with a thermocouple as a reference and immersed in a water bath. The temperature of the bath was regulated with a heater and chiller to zero and span the transducer.

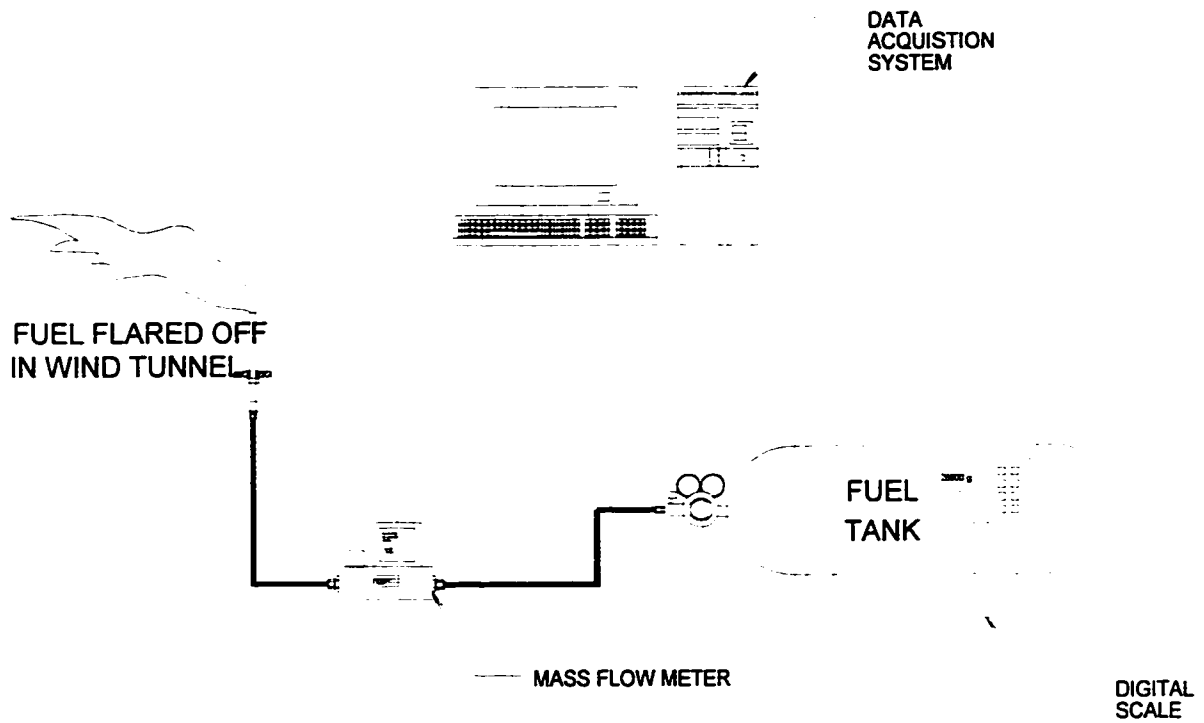


Figure C.4 - Schematic of Mass Flow Meter Calibration Set-Up. Gas was flowed through the meter and meter output was monitored by the data acquisition system. The mass flow rate was determined by reading the change in weight of the gas tank with a digital scale. Each meter calibration consisted of measurements at no less than five flow rates spanning the meter range.

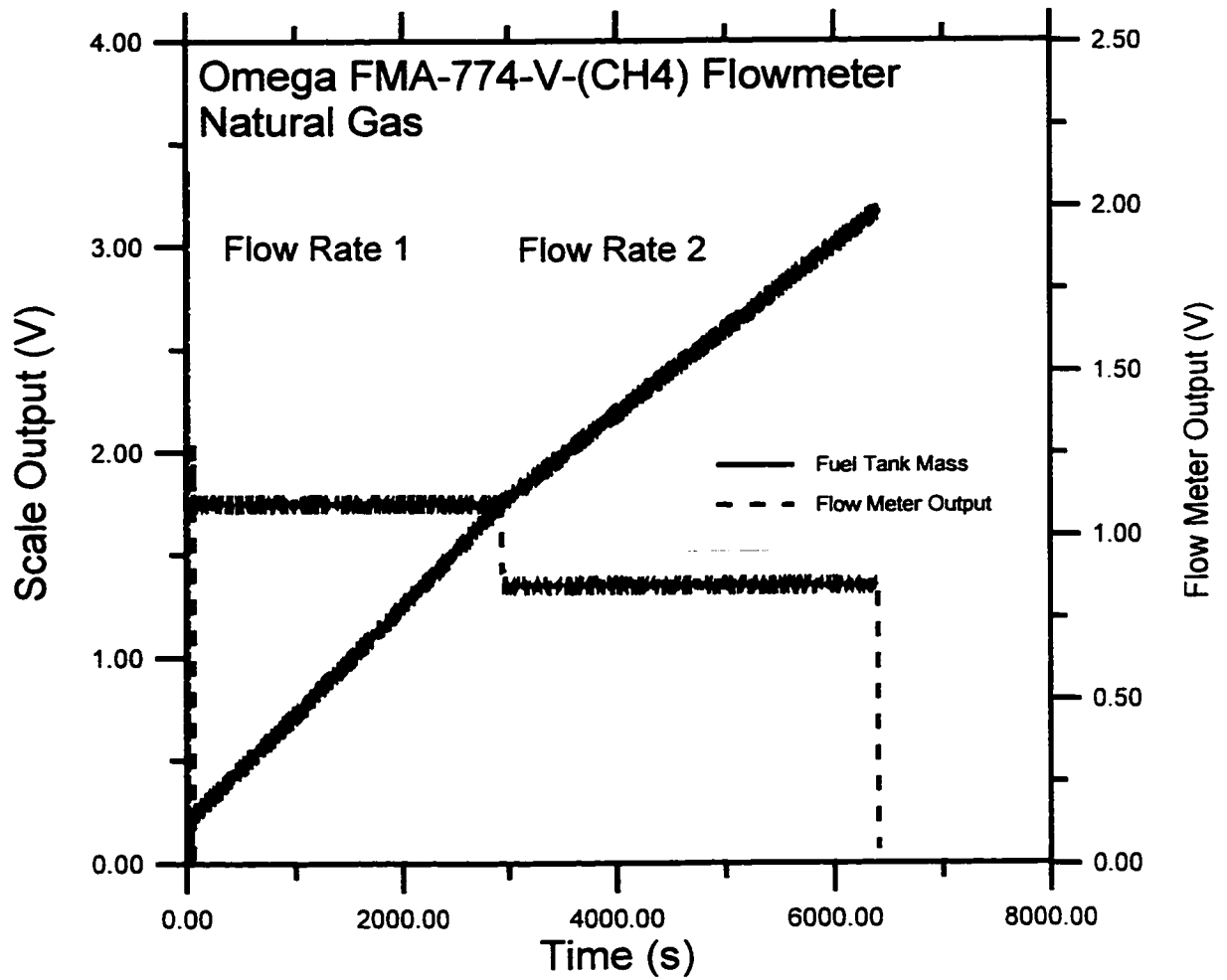


Figure C.5 - Typical plot of output for flow meter calibration. Mass flow rate through the flow meter was determined by measuring the slope of a plot of fuel tank mass versus time. The voltage output at each mass flow rate was taken as an average of the voltage output over the calibration.

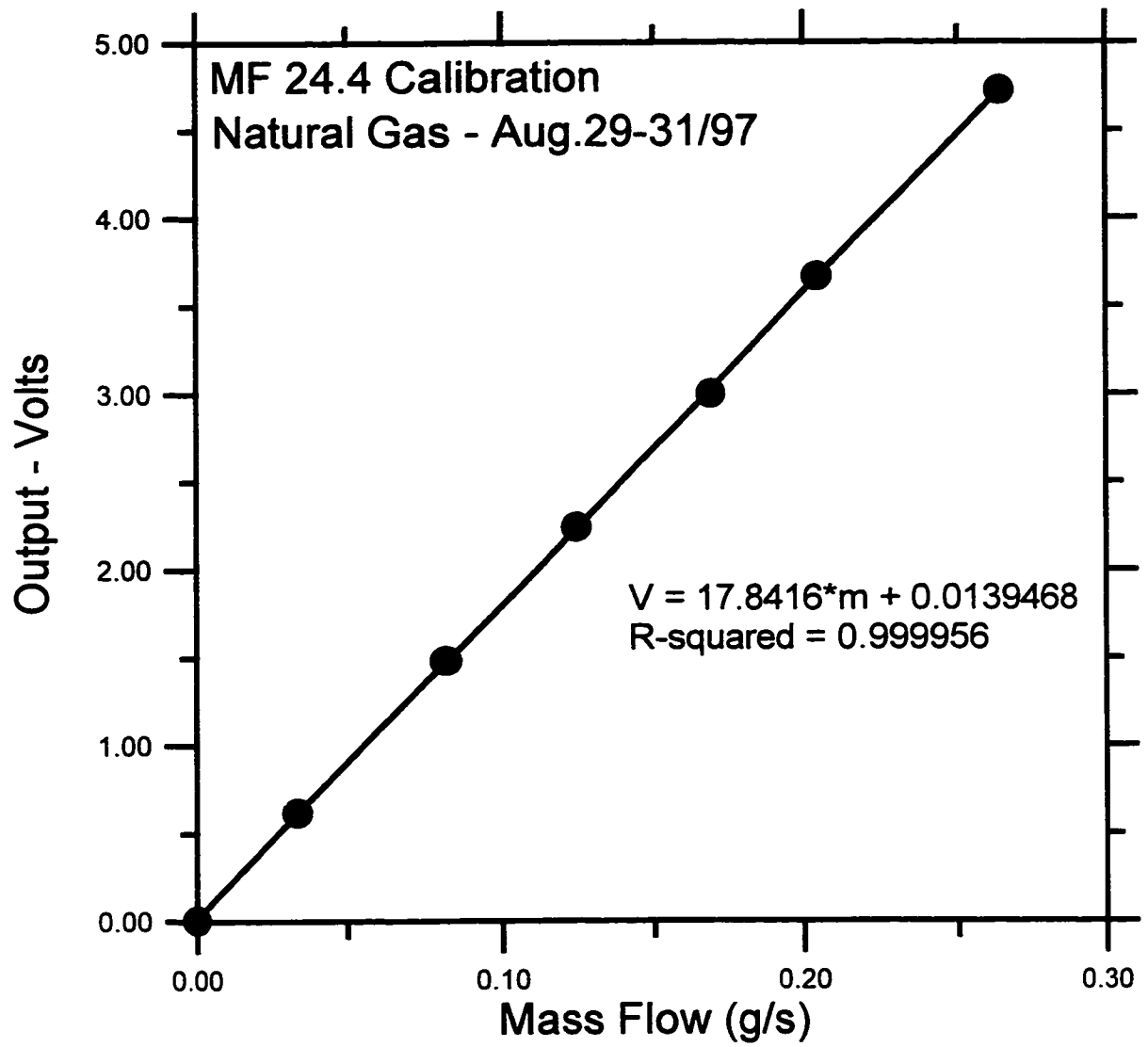


Figure C.6 - Matheson 24.4 SLPM Flowmeter calibrated with natural gas

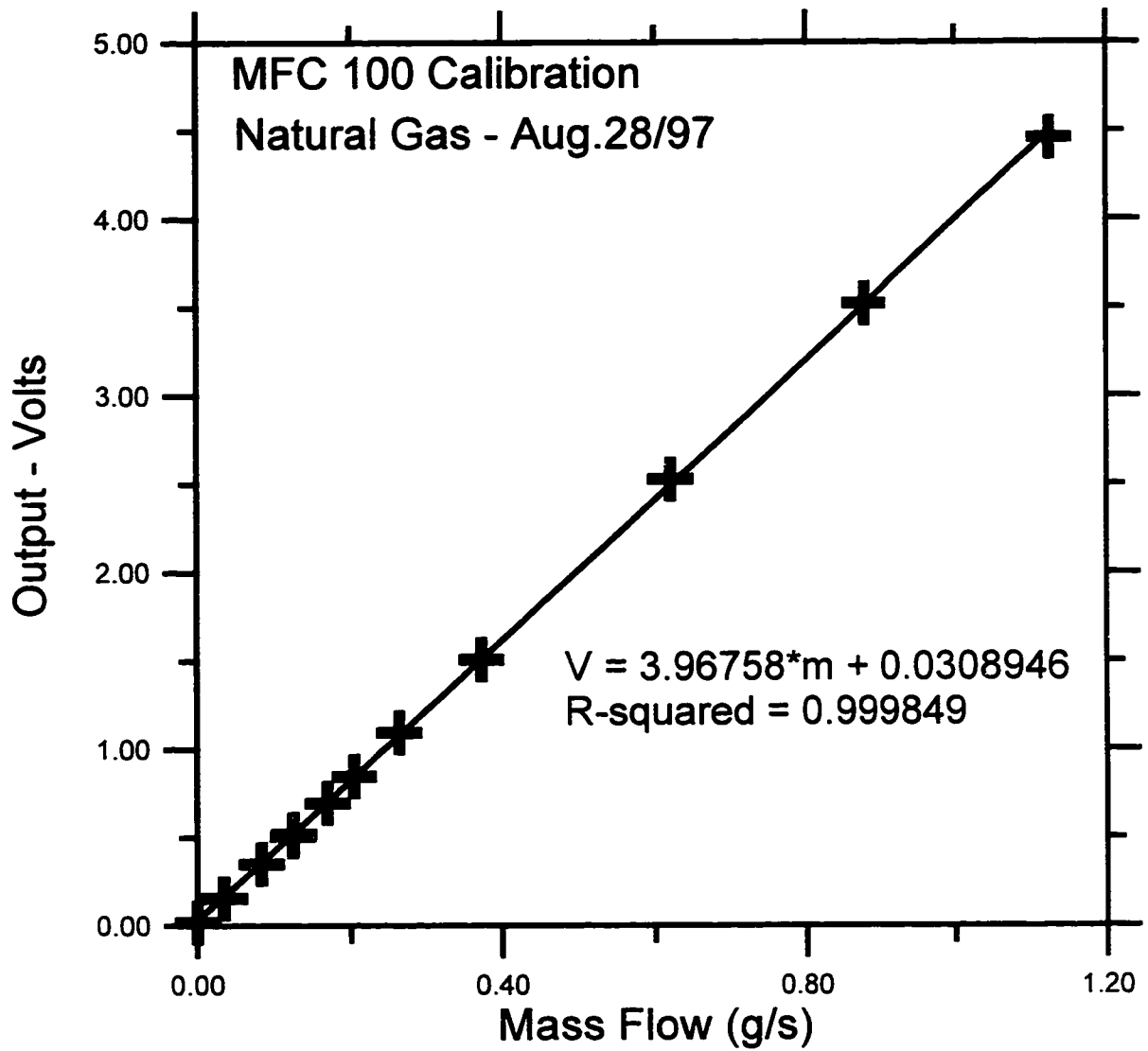


Figure C.7 - Omega 100 SLPM Flow Meter/Controller calibration with natural gas

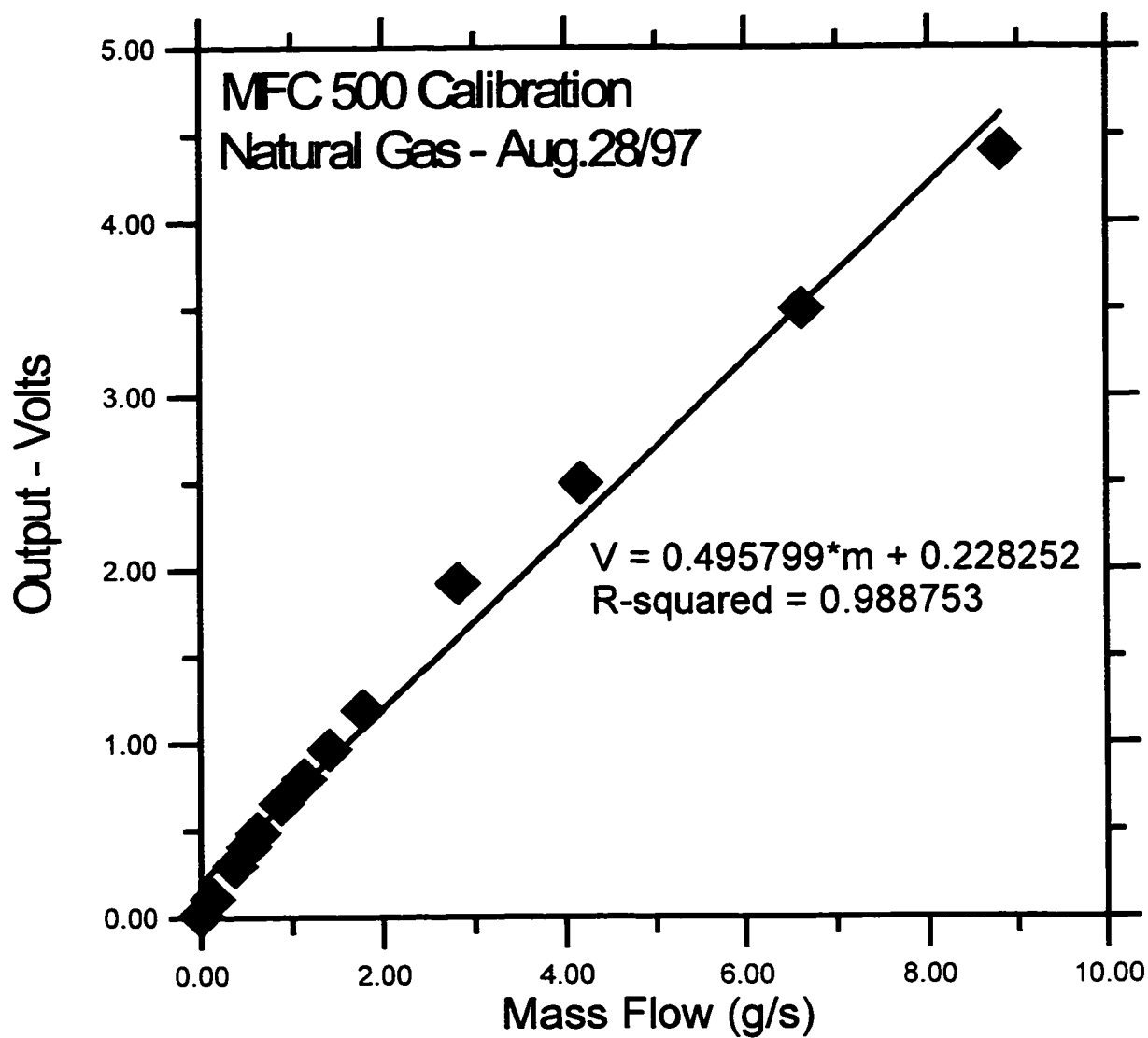


Figure C.8 - Omega 500 SLPM Flowmeter calibrated with natural gas

Appendix D - Uncertainty Analysis of Inefficiency

Measurement

This appendix gives the details of an analysis of the random uncertainty associated with flare inefficiencies calculated using the hydrocarbon reference efficiency measurement procedure described in Chapter 2.

Inefficiency Equation

The equation developed in Chapter 2 to calculate the inefficiency of a jet diffusion flame from test data is

$$I_d = \frac{\rho_{ref} Q_{ref} n_{ref}}{\rho_f Q_f n_f} \left(\frac{B}{A} - 1 \right)^{-1} \quad \text{D.1}$$

where

I_d = destruction inefficiency of the flame

ρ = gas density, (kg/m³)

Q = gas flow rate, (m³/s)

n = number of carbon atoms in gas molecule

y_{HC} = concentration of hydrocarbons in wind tunnel, (ppm)

T = temperature in wind tunnel, (K)

$A = \frac{d}{dt} \left(\frac{y_{HC}}{T} \right)$, (ppm/K · s)

$$B = \frac{d}{dt} \left(\frac{y_{HC}}{T} \right)_{ref}, \text{ (ppm/K} \cdot \text{s)}$$

with subscripts

f = relates to fuel supplied to flame

ref = relates to hydrocarbon injected as reference flow

Expression for Uncertainty

Assuming independence between all variables, uncertainty in inefficiency can be expressed in terms of the individual variables that make up the expression D.1 [Wilson, 1993] as

$$\epsilon_{I_d}^2 = \sum_{j=1}^N \left(\frac{\partial I_d}{\partial x_j} \right)^2 \epsilon_{x_j}^2$$

D.2

where

ϵ = uncertainty in quantity

x = generalized variable in inefficiency equation

j = index

N = total number of variables

For the variables in D.1, D.2 takes the form

$$\begin{aligned}
\varepsilon_{1-\eta}^2 = & \left(\frac{\partial I_d}{\partial \rho_f} \right)^2 \varepsilon_{\rho_f}^2 + \left(\frac{\partial I_d}{\partial Q_f} \right)^2 \varepsilon_{Q_f}^2 + \left(\frac{\partial I_d}{\partial n_f} \right)^2 \varepsilon_{n_f}^2 \\
& + \left(\frac{\partial I_d}{\partial \rho_{ref}} \right)^2 \varepsilon_{\rho_{ref}}^2 + \left(\frac{\partial I_d}{\partial Q_{ref}} \right)^2 \varepsilon_{Q_{ref}}^2 + \left(\frac{\partial I_d}{\partial n_{ref}} \right)^2 \varepsilon_{n_{ref}}^2 \\
& + \left(\frac{\partial I_d}{\partial B} \right)^2 \varepsilon_B^2 + \left(\frac{\partial I_d}{\partial A} \right)^2 \varepsilon_A^2
\end{aligned} \tag{D.3}$$

Computing the partial derivatives and rearranging terms results in

$$\varepsilon_{I_d}^2 = I_d^2 \left(\begin{aligned} & \frac{1}{\rho_f^2} \varepsilon_{\rho_f}^2 + \frac{1}{Q_f^2} \varepsilon_{Q_f}^2 + \frac{1}{n_f^2} \varepsilon_{n_f}^2 \\ & + \frac{1}{\rho_{ref}^2} \varepsilon_{\rho_{ref}}^2 + \frac{1}{Q_{ref}^2} \varepsilon_{Q_{ref}}^2 + \frac{1}{n_{ref}^2} \varepsilon_{n_{ref}}^2 \\ & + \left(\left(\frac{B}{A} - 1 \right) A \right)^{-2} \varepsilon_B^2 \\ & + B^2 \left(\left(\frac{B}{A} - 1 \right) A^2 \right)^{-2} \varepsilon_A^2 \end{aligned} \right) \tag{D.4}$$

Some of the uncertainties can be determined from instrument calibrations (Q_f , Q_{ref}). The uncertainties in gas composition (ρ_f , n_f , ρ_{ref} , n_{ref}) were available and are presented in **Table**

D-1. The uncertainty in the terms A and B (the time rate of change of hydrocarbon

concentration divided by tunnel temperature) are unknown. That uncertainty is a function of the uncertainty in the measurement of hydrocarbon concentration, and temperature, and of the uncertainty in the slope of the linear regression used to calculate its rate of change.

Calculation of Uncertainty in $\frac{d}{dt}\left(\frac{y_{HC}}{T}\right)$

$\frac{d}{dt}\left(\frac{y_{HC}}{T}\right)$ is calculated as the slope of a linear regression of y_{HC}/T with respect to time.

The regression takes the form

$$\frac{y_{HC}}{T} = \beta_0 + \beta_1 t \quad \text{D.5}$$

where β_0 and β_1 are the coefficients solved for in the regression.

The uncertainty in $\frac{d}{dt}\left(\frac{y_{HC}}{T}\right)$ is determined by computing a confidence interval for slope

β_1 using a Student-t test [Mendenhall & Sincich, 1992, p.438].

$$\hat{\beta}_1 \pm t_{\frac{\alpha}{2}} s_{\hat{\beta}_1} \quad \text{D.6}$$

where

$$\hat{s}_{\beta_1} = \frac{s}{\sqrt{SS_{xx}}} \quad \text{D.7}$$

s = standard deviation of y_{HC}/T relative to the regression

$$SS_{tt} = \sum_{i=1}^N t_i^2 - \frac{\left(\sum_{i=1}^N t_i\right)^2}{N} \quad \text{D.8}$$

N = number of points used to compute the regression

$\tau_{\alpha/2}$ = Student-t test for $(N-2)$ degrees of freedom

t_i = time at each point in the regression

The standard deviation of y_{HC}/T is determined from a combination of the uncertainties in y_{HC} and T , as in Equation D.2

$$s_{\frac{y_{HC}}{T}}^2 = \left(\frac{s_{y_{HC}}^2}{T^2} + \frac{y_{HC}^2 s_T^2}{T^4} \right) \quad \text{D.9}$$

After representative values for T and y_{HC} are substituted, the standard deviation of y_{HC}/T becomes an expression for the uncertainty in the slope:

$$\mathcal{E}_{\frac{y_{HC}}{T}}^2 = \left(\frac{\mathcal{E}_{y_{HC}}^2}{T_{avg}^2} + \frac{y_{HC,avg}^2 \mathcal{E}_T^2}{T_{avg}^4} \right) \quad \text{D.10}$$

where

$\epsilon_{Y_{HC}}$ = uncertainty in hydrocarbon concentration measurement

$y_{HC, avg}$ = mid-range of hydrocarbon measurement

ϵ_T = uncertainty in temperature measurement

T_{avg} = average temperature during test (K)

Substituting Equations D.7 and D.8 into D.6, we obtain an expression for uncertainty in

$$\frac{d}{dt} \left(\frac{y_{HC}}{T} \right):$$

$$\epsilon \frac{d}{dt} \left(\frac{y_{HC}}{T} \right) = \frac{\tau_{0.025} \left(\frac{\epsilon_{y_{HC}}^2}{T_{avg}^2} + \frac{y_{HC, avg}^2 \epsilon_T^2}{T_{avg}^4} \right)^{\frac{1}{2}}}{\left(\sum_{i=1}^N t_i^2 - \frac{\left(\sum_{i=1}^N t_i \right)^2}{N} \right)^{\frac{1}{2}}} \quad \text{D.11}$$

where

$\tau_{0.025}$ = t statistic for a 95% confidence interval with (N-2)

degrees of freedom

Examination of Equation D.11 shows that uncertainty increases as hydrocarbon concentration increases and temperature decreases.

Sample Calculation

This is a calculation of the uncertainty for a typical-fueled flare test using the experimental set-up detailed in Chapter 2.

The uncertainty in the Rosemount low-range FID used to detect hydrocarbon concentration is $\pm 1\%$ full-scale. For a range of 102 ppm, the uncertainty in hydrocarbon concentration is $\epsilon_{\text{HC}} = 1.02$ ppm. The uncertainty in the AD590 temperature sensor is $\pm 0.5\%$ full-scale. For a range of 223-323 K, $\epsilon_T = 0.5$ K. The average temperature in the wind tunnel during a test was 290 K.

During a typical 15 minute test segment, 900 data points were collected at 1 s intervals.

The t-test for $(900-2)=898$ degrees of freedom for a 95% confidence interval is $t=1.960$.

Substituting these values into Equation D.11,

$$\epsilon_{\frac{d}{dt}\left(\frac{y_{\text{HC}}}{T}\right)} = \frac{(1.960) \left(\frac{(1.02 \text{ ppm})^2}{(290 \text{ K})^2} + \frac{(51 \text{ ppm})^2 (0.5 \text{ K})^2}{(290 \text{ K})^4} \right)^{\frac{1}{2}}}{\left(\sum_{i=1}^{900} t_i^2 - \frac{\left(\sum_{i=1}^{900} t_i \right)^2}{900} \right)^{\frac{1}{2}}} \quad \text{D.12}$$
$$= \underline{\underline{8.880 \times 10^{-7} \frac{\text{ppm}}{\text{K} \cdot \text{s}}}}$$

Uncertainties of Variables in Equation D.4

Table D-1 contains the uncertainties in the measurements conducted during inefficiency tests.

Table D-1 - Uncertainties in variables used to calculate inefficiency

Quantity	Uncertainty	Source
Fuel Density	$1.943 \times 10^{-3} \text{ kg/m}^3$	M. Johnson, M.Sc. Thesis
Fuel Flow Rate		
■ Matheson 24.4 SLPM Flow Meter	0.244 SLPM	Flow meter calibration
■ Omega 100 SLPM Flow Meter	1.00 SLPM	Flow meter calibration
Number of atoms of carbon in fuel molecule	0.005537	M. Johnson, M.Sc. Thesis
Reference Hydrocarbon Density	$1.943 \times 10^{-3} \text{ kg/m}^3$	M. Johnson, M.Sc. Thesis
Reference Flow Rate		
■ Omega 0.2 SLPM	0.004 SLPM	Flow meter calibration
■ Omega 1 SLPM	0.020 SLPM	Flow meter calibration
■ Omega 5 SLPM	0.100 SLPM	Flow meter calibration

Number of carbon atoms in reference gas molecule	0.005537	M.Johnson, M.Sc. Thesis
$\frac{d}{dt} \left(\frac{y_{HC}}{T} \right)$		
■ Low Range FID	1.491x10 ⁻⁶ ppm/K*s	Calculated from D.11
■ High Range FID	1.869x10 ⁻⁶ ppm/K*s	Calculated from D.11
$\frac{d}{dt} \left(\frac{y_{HC}}{T} \right)_{ref}$		
■ Low Range FID	1.491x10 ⁻⁶ ppm/K*s	Calculated from D.11
■ High Range FID	1.869x10 ⁻⁶ ppm/K*s	Calculated from D.11

Sample Uncertainty Calculation

This is a calculation of the uncertainty in the inefficiency measured by test ENHD1005.

This test involved a methane flame with a 25.4 mm burner, ~10 SLPM fuel flow rate and ~5 m/s cross-wind.

For this test,

$$Q_{\text{REF}} = 0.256 \text{ SLPM}$$

$$\epsilon_{Q_{\text{REF}}} = 0.040 \text{ SLPM}$$

$$Q_{\text{F}} = 10.106 \text{ SLPM}$$

$$\epsilon_{Q_{\text{F}}} = 0.244 \text{ SLPM}$$

$$A = 2.692 \times 10^{-5} \text{ ppm/K*s}$$

$$\epsilon_A = 8.880 \times 10^{-7} \text{ ppm/K*s}$$

$$B = 6.336 \times 10^{-5} \text{ ppm/K*s}$$

$$\epsilon_B = 8.880 \times 10^{-7} \text{ ppm/K*s}$$

Sales-grade natural gas was used for both the fuel and the reference gas, so the density and n terms cancel out when inefficiency is computed. In tests where the reference gas is different from the flare gas these uncertainties remain in the calculation.

Inefficiency for ENHD1005 was calculated as $I_d = 0.0187$.

Substituting the values above into Equation D.4 gives

$$\begin{aligned}
\varepsilon_{i_s}^2 &= (0.0187)^2 + \left(\frac{(0.244\text{SLPM})^2}{(10.106\text{SLPM})^2} (0.244\text{SLPM})^2 + \frac{(0.04\text{SLPM})^2}{(0.256\text{SLPM})^2} (0.020\text{SLPM})^2 \right. \\
&\quad \left. + \left(\frac{6.336 \times 10^{-5} \frac{\text{ppm}}{\text{K} \cdot \text{s}}}{2.692 \times 10^{-5} \frac{\text{ppm}}{\text{K} \cdot \text{s}}} - 1 \right) \left(2.692 \times 10^{-5} \frac{\text{ppm}}{\text{K} \cdot \text{s}} \right)^2 \left(8.880 \times 10^{-7} \frac{\text{ppm}}{\text{K} \cdot \text{s}} \right)^2 \right. \\
&\quad \left. + \left(6.336 \times 10^{-5} \frac{\text{ppm}}{\text{K} \cdot \text{s}} \right)^2 \left(\frac{6.336 \times 10^{-5} \frac{\text{ppm}}{\text{K} \cdot \text{s}}}{2.692 \times 10^{-5} \frac{\text{ppm}}{\text{K} \cdot \text{s}}} - 1 \right) \left(2.692 \times 10^{-5} \frac{\text{ppm}}{\text{K} \cdot \text{s}} \right)^2 \left(8.880 \times 10^{-7} \frac{\text{ppm}}{\text{K} \cdot \text{s}} \right)^2 \right) \\
&= (3.493 \times 10^{-4}) (3.471 \times 10^{-5} + 9.766 \times 10^{-6} + 5.937 \times 10^{-4} + 3.288 \times 10^{-3}) \\
&\quad \uparrow \uparrow \uparrow \uparrow \\
&\quad \text{fuel flow reference flowslope / ref slope / o ref} \\
\varepsilon_{i_s} &= 1.171 \times 10^{-3}
\end{aligned}
\tag{D.13}$$

Therefore the inefficiency in test ENHD1005 expressed as a percentage is $1.87 \pm 0.2\%$ (i.e. $1.85\% < I_d < 1.89\%$).

Examining the terms in Equation D.13, it is apparent that the greatest contributor to uncertainty was the uncertainty in the rates of accumulation of hydrocarbons.

References

Johnson, M.R.; Development of a Low Emissions, Lean Premixed, Natural Gas Burner,

M.Sc. Thesis, University of Alberta, 1995.

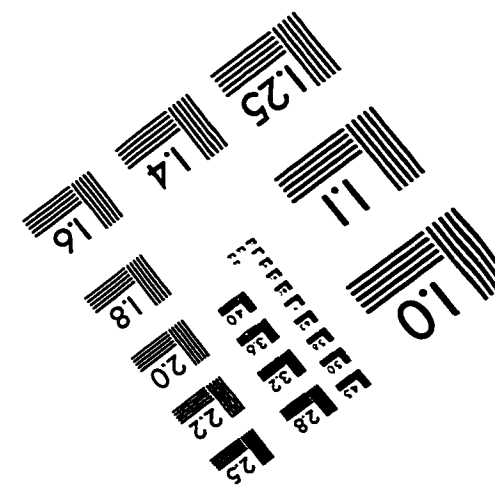
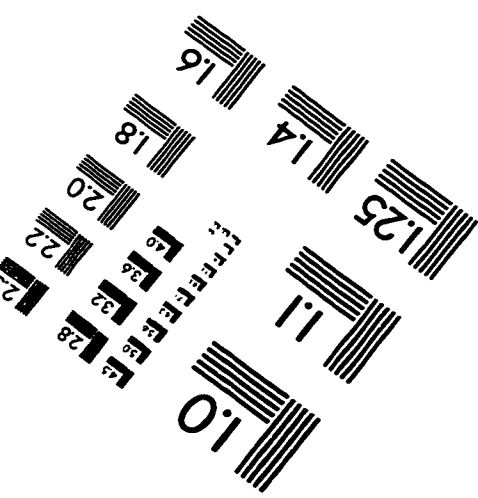
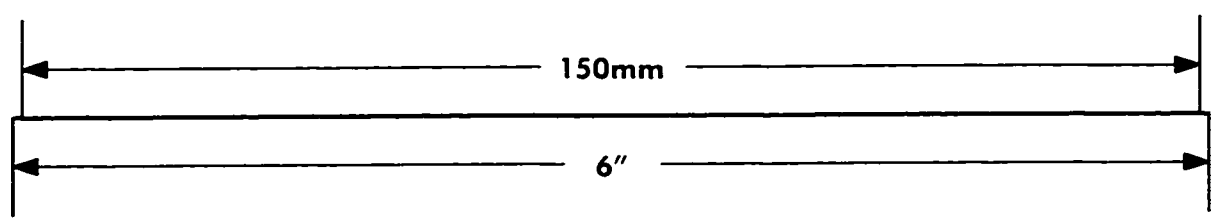
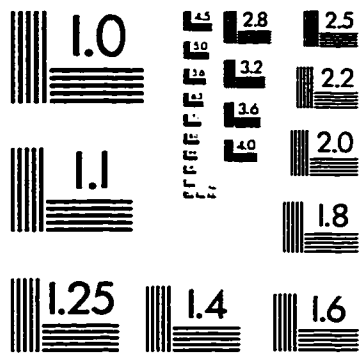
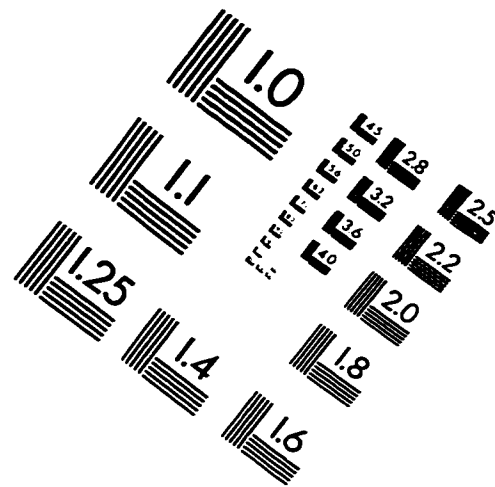
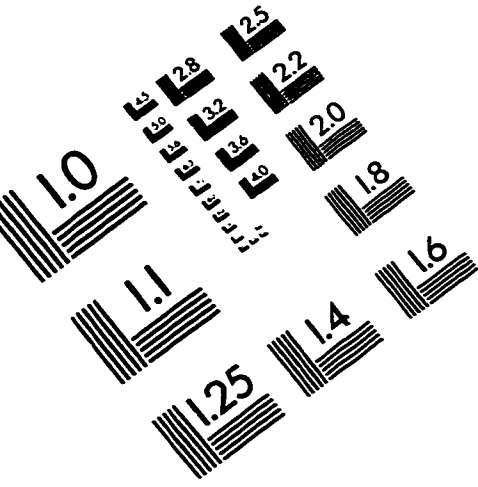
Medenhall, William and Sincich, Terry, Statistics for Engineering and the Sciences,

Dellen Publishing, 3rd Edition, 1992.

Wilson, D.J., Mechanical Measurements - Statistical Analysis of Data, Department of

Mechanical Engineering, University of Alberta, September 1993.

IMAGE EVALUATION TEST TARGET (QA-3)



APPLIED IMAGE, Inc
1653 East Main Street
Rochester, NY 14609 USA
Phone: 716/482-0300
Fax: 716/288-5989

© 1993, Applied Image, Inc., All Rights Reserved